Mitochondrial dynamics and purine metabolism in zebrafish cone photoreceptors

Kaitlyn Michelle Rutter

A dissertation

submitted in partial fulfillment of the

requirements for the degree of

Doctor of Philosophy

University of Washington

2025

Reading Committee:

Susan Brockerhoff, Chair

James Hurley

Suzanne Hoppins

Program Authorized to Offer Degree:

Biochemistry

University of Washington

Abstract

Mitochondrial dynamics and purine metabolism in zebrafish cone photoreceptors

Kaitlyn Michelle Rutter

Chair of the Supervisory Committee:

Susan Brockerhoff

Department of Biochemistry

Photoreceptors, the light-detecting cells in the retina, are vital for vision. Despite being post-mitotic and having high energy demands, photoreceptors survive throughout a human's lifespan. However, many different proteins, including inosine monophosphate dehydrogenase 1 (IMPDH1), can cause vision loss when mutated. In this thesis, I describe a strategy used by zebrafish photoreceptors to remain healthy throughout their lifespan. I also present new hypotheses to explain why cone photoreceptors degenerate when faced with a genetically-induced metabolic insult. Although photoreceptors are mostly glycolytic, they have abundant mitochondria that help with energy demand. We found that cone photoreceptor mitochondria are dynamic depending on the time of day and energy demands. Further, we found that at night, cone mitochondria extrude material out of cones. We expanded our studies to evaluate how larval zebrafish cone mitochondria handle stress. In stressed and unstressed conditions, cone mitochondria migrate away from the ellipsoid region. These unhealthy mitochondria are ejected from the cell, and Müller glia take them up for turnover. We also tested a metabolic stressor by expressing mutant forms of Impdh1a in cone photoreceptors. In humans, these mutations lead

to photoreceptor degeneration. Some Impdh1a mutations are hyperactive *in vitro* so we designed the first Impdh1a mutant animal models to analyze enzyme activity *in vivo.* We found no evidence for Impdh1a hyperactivity in zebrafish cone photoreceptors and instead found other metabolic phenotypes that could contribute to disease. We also found that Impdh1a mutants form large mislocalized filaments that may disrupt important protein-protein interactions. These studies are important for understanding cone health in the context of daily energy demand changes, stress, and disease.

Table of Contents

List of Figures

Figures

Supplementary Figures

Glossary

3D – three-dimensional

ad-RP – autosomal dominant retinitis pigmentosa

ADSS – adenylosuccinate synthetase

CAP – chloramphenicol

CLEM – correlative light and electron microscopy

CNG – cyclic nucleotide gated

COX – cytochrome c oxidase, complex IV

DD – 24-h dark

dpf – days post fertilization

EM – electron microscopy

ER – endoplasmic reticulum

FRET – fluorescence resonance energy transfer

GC/MS – gas chromatography mass spectrometry

IHC – immunohistochemistry

IMP – inosine monophosphate

IMPDH1 – inosine monophosphate dehydrogenase 1

IPM – interphotoreceptor matrix

KO – knockout

KR - KillerRed

LCA – Leber congenital amaurosis

LD – 14-h/10-h light-dark

MCI – mitochondrial complexity index

MCU – mitochondrial calcium uniporter

MG – Müller glia

MTCO1 – cytochrome c oxidase 1

mtDNA – mitochondrial DNA

mtKR – mitochondrial KillerRed

ns – not significant

OLM – outer limiting membrane

ONH – optic nerve head

OS – outer segment

PDE6 – phosphodiesterase 6

PI – propidium iodide

PPP – pentose phosphate pathway

PR – photoreceptor

PRPP – phosphoribosyl pyrophosphate

PTU – 1-phenyl 2-thiourea

RGCs – retinal ganglion cells

ROS – reactive oxygen species

RPE – retinal pigment epithelium

RT – room temperature

SBFSEM – serial block-face scanning electron microscopy

SDH – succinate dehydrogenase, complex II

secA5 – secreted Annexin5+

TCA – tricarboxylic acid

Tg WT – transgenic wild type

UV – ultraviolet

WT – wild type

XMP – xanthine monophosphate

ZT – Zeitgeber Time

Acknowledgements

I have grown as a scientist and person in ways I would not have if it had not been for the incredible people I've interacted with in the scientific community. I want to start by thanking my thesis advisor, Dr. Susan Brockerhoff, for her unwavering support of me throughout my time at the University of Washington. I'm especially grateful for her helping me build my confidence as a scientist. In the Brockerhoff lab, I worked closely with Dr. James Hurley, whom I also owe great thanks to. I appreciate the fun hypotheses he suggests that have helped me think about my work more deeply. I want to thank my committee members, Dr. Suzanne Hoppins, Dr. Yasemin Sancak, and Dr. Hannele Ruohola-Baker, for their insightful comments and support throughout my Ph.D. Additionally, I thank Erin Kirscher for all that she does, including deconvoluting the administrative complexities of going through the whole Ph.D. process.

I would also like to thank the incredible past and present lab members of the Brockerhoff and Hurley labs – Vivian Truong, Matthew Liu, Rachel Hutto, Michelle Giarmarco, Riddhi Atmakuri, Whitney Cleghorn, Chloe Sygitowicz, William Wu, Valentina Alvarez, Kristine Tsantilas, Richard Lowery, Cameron Haydinger, Hunter Frey-Burkart, Kriti Pandey, Brian Robbings, Laura Masserman, Celia Bisbach, Daniel Hass, Tai Le, and Marcos Nazario Jr. You all have helped me grow both as a scientist and as a person. Dr. Jennifer Chao and her lab members, Rayne Lim, Abbi Engel, and Sheldon Niernberger, provide support, laughs, and insights. Dr. Ian Sweet also helped strengthen my approach to thinking about science. Dr. Justin Kollman's lab adopted me on long metabolic flux experiment days, and provided insight into how to think about IMPDH, especially John Calise, Anika Burrell, Gardenia Sanchez, and Audrey O'Neill. A huge thank you to the countless hours Nicole Fan, Stanley Kim, and Jeanot Muster spent keeping the zebrafish facility running smoothly. My biochemistry and BPSD cohort brought a sense of community much needed throughout graduate school – especially Chloe

Adams, Erin Yang, Madison Kennedy, Yuxin Pan, Andrew Muenks, Dane Zambrano, and Meerit Said.

I took my first chemistry course during my undergraduate education, and I thank my professor, Dr. Tim D'Andrea, for convincing me that I was capable of pursuing a degree in chemistry. At Colorado Mesa University, I had many professors who made a lasting impact on my life, most notably Dr. Ed Bonan-Hamada, Dr. Shay West, and Dr. Sam Lohse. Throughout my undergraduate education, I had the pleasure of studying and developing friendships with Robin Marley, Jacob Williams, Nick Curry, Michelle Emig, and Olivia Harwood. During my final years as an undergraduate, I was fortunate to join the lab of Dr. David Weinberg. Thank you, Dave, for being a phenomenal mentor and providing a safe and fun research experience. I traveled to Duquesne University for a summer REU program and did research in Dr. Michael Cascio's group. I want to thank Dr. Cascio, Dr. Kayce Tomcho, and Liz Tidwell for building my biochemistry skillset and helping solidify my decision to pursue a Ph.D. in biochemistry.

My close friends have helped me in more ways than words can describe during my academic journey. Thank you, Elaine Bressler, Erin Myers, and Kayla Nored. You all make my life so much fun. I want to thank my wonderful in-laws for years of support: Noelle, Andrew, Natalie, Beth, Jeff, John, Dawn, and Nick.

I want to thank my parents, Dianne and Gary Gilmore, for teaching me to be strong, inquisitive, and humble. My younger brother, Trent, has kept me on my toes and has been a constant support. My grandpa, Marvin, and aunt, Cindy, have cheered me on and helped me relax in the Nebraska countryside. My husband, Matthew Rutter, is more than I could have ever imagined in a partner. Matt, you've believed in me in the good times and the times I've doubted myself. Not only have you helped shape how I view myself, but also the world. I cannot wait to continue exploring life with you. Finally, I would like to give a huge shout-out to all the wonderful animals in my life. Science and life can get hard, and on those days, time with you always makes it better. Thank you, Annie, Chell, Louie, Skye, Lacey, Felix, and Ozzie.

Dedication

For my nana, Elva Dianne Juedes, who taught me strength, perseverance, and warmth.

Chapter 1 – Introduction

The retina is vital for vision

Between the retinal pigment epithelium (RPE) and vitreous humor in the eye, the retina is critical for detecting and converting light into an electrical signal (Fig. 1.1). This signal is sent down the optic nerve to the brain, where it is processed into the images we see. Without a functioning retina, light detection in the eye would cease, and our vision would be rendered non-existent. The retina is composed of several types of neurons and glia. Photoreceptors line the back of the retina, near the RPE (Fig. 1.1). Photoreceptors initiate vision through phototransduction. Rod photoreceptors are saturated in bright light and thus contribute to our visual image in dim lighting. Cone photoreceptors detect colors, contribute to our visual image in brighter light, and have higher acuity than rods. In humans, rods are more prevalent in the periphery of the retina, and cones are more concentrated near the center in an area known as the fovea. In humans, significant rod death is typically correlated with loss of peripheral vision and/or night blindness, whereas significant cone death is typically associated with loss of central vision.

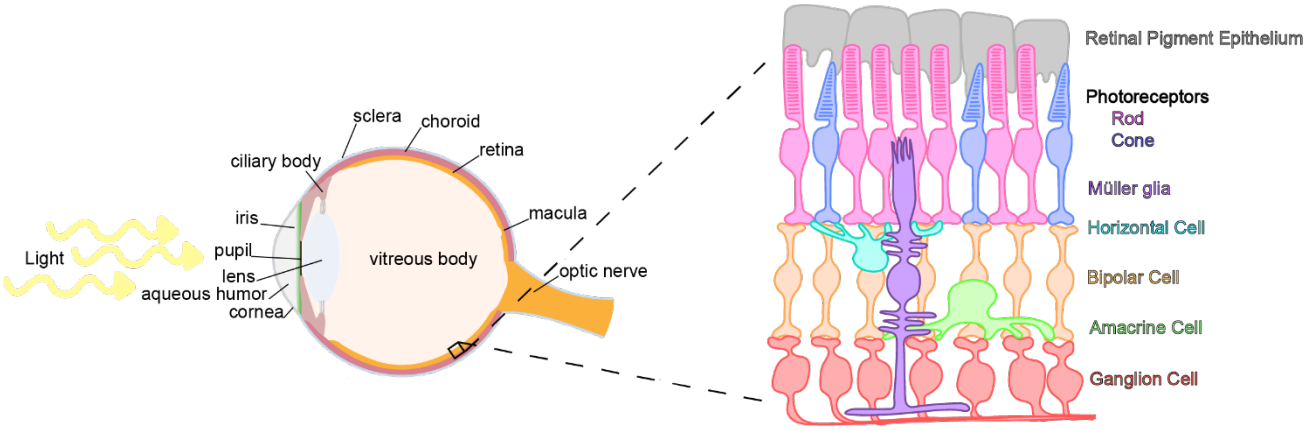

Figure 1.1 Diagram of eye and retinal layer

Photoreceptors are post-mitotic neurons consisting of abundant mitochondrial pools and outer segments (Fig. 1.2). Outer segments are stacks of membrane disks packed with proteins necessary for phototransduction. Phototransduction is a G-protein signaling pathway for

detecting light in photoreceptors. In rods, rhodopsin gets activated upon photon absorption. Activated rhodopsin catalyzes transducin, which then activates phosphodiesterase (PDE). Activated PDE hydrolyzes cGMP to GMP, which leads to the closure of cyclic nucleotide-gated (CNG) channels on the plasma membrane (Fig. 1.3) (Arshavsky et al., 2002). CNG channel closure reduces cation flow into rod outer segments, resulting in membrane hyperpolarization. Hyperpolarization stops glutamate release from rod synapses, and inner retinal neurons further process the signal to the optic nerve. Cone photoreceptors also use phototransduction to detect light but instead use cone opsins that have different spectral sensitivities to produce color vision. Photoreceptors are unique among other neurons in that they have graded hyperpolarization, meaning that the number of photons correlates with the resulting signal sent to downstream neurons until saturation. Several proteins involved in phototransduction have led to photoreceptor degenerative diseases, such as retinitis pigmentosa (RP) or Leber congenital amaurosis (LCA) when mutated.

Photoreceptors require vast amounts of energy for phototransduction, maintaining the dark current, and other cellular processes. In darkness, which is more energy-consuming than light, rods consume 10^8 ATP per second (Okawa et al., 2008). Photoreceptors are highly glycolytic, using ~90% of glucose for glycolysis and lactate production (Ames et al., 1992; Okawa et al., 2008). To supply photoreceptors with fuel, glucose must pass through the RPE left largely unconsumed. A metabolic ecosystem exists between photoreceptors and RPE – photoreceptors use glucose to make lactate that can then be exported, taken up and used by the RPE (Kanow et al., 2017). Photoreceptors also have abundant mitochondria that participate in metabolism (Bisbach et al., 2020a) or uniquely to focus light on the outer segments (Ball et al., 2022). Prior to this work (see Chapter 2), it was unclear if photoreceptor mitochondria shape, number, size, or metabolism changes throughout the day and night as energy demands shift.

Zebrafish as a model system to study cone photoreceptors

The retina has been studied using a variety of model systems, from cell culture to post-mortem human globes. Animal models have been a powerful tool to study the retina in healthy and diseased states. Mice, like humans, have rod-dominant retinas. Zebrafish retinas are more cone-dominant, similar to human macula, thus providing a powerful tool to study cone photoreceptor biology. In addition to the red, green, and blue cones seen in the human retina, zebrafish have UV cones as well. The overall retina architecture between human and zebrafish retina are the same - human and zebrafish retina have an outer nuclear layer containing photoreceptors, inner nuclear layer containing bipolar, horizontal, and amacrine cells, and a ganglion nuclear layer containing ganglion cells (Fig. 1.1). One major difference between human and zebrafish retinas is that zebrafish have regenerative capability post-injury (Wan and Goldman, 2016). This has led to a large effort to identify the regenerative factors in the zebrafish retina.

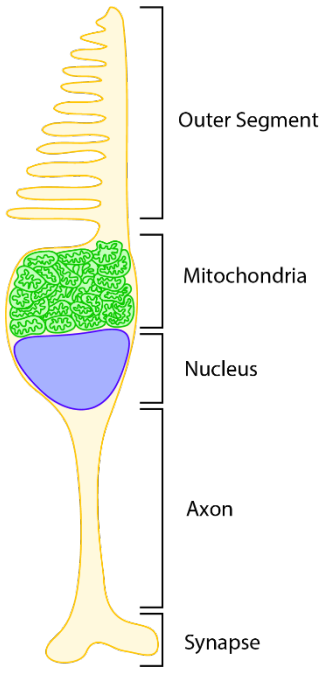

Figure 1.2 Anatomy of zebrafish cone photoreceptor

Zebrafish have been used to study and screen for visual defects for at least 20 years (Brockerhoff et al., 1995; Stearns et al., 2007). Retinal development in zebrafish is rapid – larvae have visual responses by 3 days post-fertilization (dpf) and accurate visual function by 5 dpf (Cleghorn and Brockerhoff, 2020). At 5 dpf, zebrafish larvae must rely on their vision to capture prey for nourishment, and blind zebrafish larvae have lower survival rates (Stearns et al., 2007). Zebrafish larvae can also be transparent post-treatment with phenylthiourea, which allows for live imaging. Transgenic zebrafish expressing fluorescent proteins targeted to various cellular compartments can be visualized live across time with confocal or light-sheet microscopy. We used this advantage to ask questions about cone mitochondrial dynamics in basal and stressed conditions. Zebrafish

cone mitochondria are clustered in the ellipsoid region, between the nucleus and the outer segment (Fig. 1.2). Zebrafish cone mitochondria have been observed outside the ellipsoid region during a cone mitochondrial-specific calcium stress (Hutto et al., 2020). Prior to our work (Chapter 3), it was unclear whether this occurred in unstressed conditions or with other stressors.

Mitochondrial dynamics in healthy and stressed states

Mitochondria are dynamic organelles that divide, fuse, and move. They are not only responsible for oxidative phosphorylation but also play a role in ion homeostasis, apoptosis, light guiding, and reactive oxygen species (ROS) production and consumption (Ball et al., 2022; Brand et al., 2013). Balancing mitochondrial fusion and fission is essential for overall cell health. Not surprisingly, defects in mitochondrial division and fusion machinery lead to disease (Chan, 2020). For example, autosomal dominant mutations in mitochondrial fusion protein, OPA1, can lead to vision loss stemming from optic nerve degeneration (Chan, 2020). To maintain healthy pools of mitochondria and mitochondrial DNA, mitochondria can be turned over by a process called mitophagy. In short, damaged mitochondria are separated from the healthy pool by fission. An autophagosome encircles the unhealthy mitochondrion and later fuses with a lysosome for digestion. Defects in mitophagy can lead to neurological diseases, such as Parkinson's disease, where mutations in Parkin, a protein that is involved with labeling damaged mitochondria, cause neurodegeneration (Fivenson et al., 2017). New mitochondrial material is made by transcribing and translating mtDNA, which can be regulated by PGC-1α activation. Next, proteins encoded by nuclear DNA are imported in. To deal with changing energy demands, we hypothesized that cone mitochondrial pools change throughout the day. Prior to our work, little was known about mitochondrial cluster dynamics, mitophagy, and mitochondrial biogenesis in zebrafish cone photoreceptors.

Photoreceptors are post-mitotic cells. Although a lot of work is going into retina regeneration, we currently do not have the tools to replace degenerated rods or cones. Considering incoming light damage and high metabolic demand, it's surprising that the vast majority of photoreceptors remain intact and functional throughout a person's lifetime (without retinal disease). Photoreceptors may have adapted unique methods to cope with stress. Our lab previously published work evaluating how zebrafish cone photoreceptors handle increased calcium by overexpressing the mitochondrial calcium uniporter (MCU) in cone mitochondria (Hutto et al., 2020). Mitochondrial calcium overload can lead to apoptosis by opening the mitochondrial permeability transition pore. Surprisingly, cones survived for many months before dying in our MCU OE model. Prior to degeneration, several cone mitochondria became swollen and electron-lucent. These mitochondria often migrated away from the mitochondrial cluster towards the synapse (Hutto et al., 2020). We wanted to expand on this work to test if mitochondrial movement was a neuroprotective feature of photoreceptors during different types of stress.

Mutations in metabolic protein, inosine monophosphate dehydrogenase 1 (IMPDH1), cause photoreceptor degenerative diseases

Mutations in several proteins, including IMPDH1, cause RP or LCA. Patients with LCA typically have severe vision loss at birth or shortly thereafter due to photoreceptor death. RP, on the other hand, generally takes longer to manifest but results in loss of peripheral vision and night blindness due to loss of rods. Post-rod death, cones can die, leading to loss of high-acuity central vision. RP affects 1.5 million people worldwide and is considered the most common inherited retinal disorder (Cross et al., 2022). LCA, on the other hand, has been described as one of the earliest and most severe forms of inherited retinal disorders and affects approximately 1/81,000 to 1/30,000 (Huang et al., 2021). There is currently no cure for either RP or LCA. Currently approved treatments have focused more on preserving remaining

photoreceptors (Confalonieri et al., 2024). Gene therapy, small molecule therapeutics, or cell transplantation are current areas of study with varying levels of success (Confalonieri et al., 2024).

Over 150 proteins that, when mutated, lead to either LCA or RP ("RetNet - Retinal Information Network," n.d.). Several of these proteins are involved in phototransduction, but others, like IMPDH1, have a less clear role in photoreceptor maintenance. Mutations in IMPDH1 are also distinct, as some evidence suggests an early cone defect (Bennett et al., 2020; Sakti et al., 2023; Wada et al., 2005; Wendel et al., 2024). This is not necessarily surprising as IMPDH1 is expressed in both rod and cone photoreceptors (Cleghorn et al., 2022; Karlsson et al., 2021; Plana-Bonamaisó et al., 2020). Knocking out IMPDH1 in mice only led to a mild retinopathy and, in zebrafish, led to a significant reduction in guanine levels but no signs of photoreceptor degeneration (Aherne et al., 2004; Cleghorn et al., 2022). This supports the hypothesis that IMPDH1 mutations are gain of function mutations. Prior to our work, there was no known animal model to investigate the mechanism of degeneration. Zebrafish are a powerful way to study cone photoreceptor biology and address how mutations in IMPDH1 impact cone homeostasis (Cleghorn and Brockerhoff, 2020).

IMPDH is a rate-limiting enzyme in the *de novo* purine biosynthesis pathway. There are two isoforms of IMPDH that share 84% sequence identity: IMPDH1 is generally expressed in most tissues, whereas IMPDH2 is upregulated during proliferation (Carr et al., 1993; Jackson et al., 1975; Senda and Natsumeda, 1994). Both IMPDH1 and 2 mutations lead to disease – in the case of IMPDH2, it is associated with neurological diseases, and IMPDH1 is associated with retinal degenerative diseases. It converts IMP to XMP, reducing NAD^+ to NADH. Structurally, IMPDH has a catalytic domain where IMP and NAD^+ can bind and a regulatory domain where ATP and GTP can bind at three distinct sites. IMPDH forms octomers that stack to form filaments. Forming a filament is thought to provide further enzyme regulation (Johnson and Kollman, 2020). The retina has a specific isoform of IMPDH1 that has N and C terminal

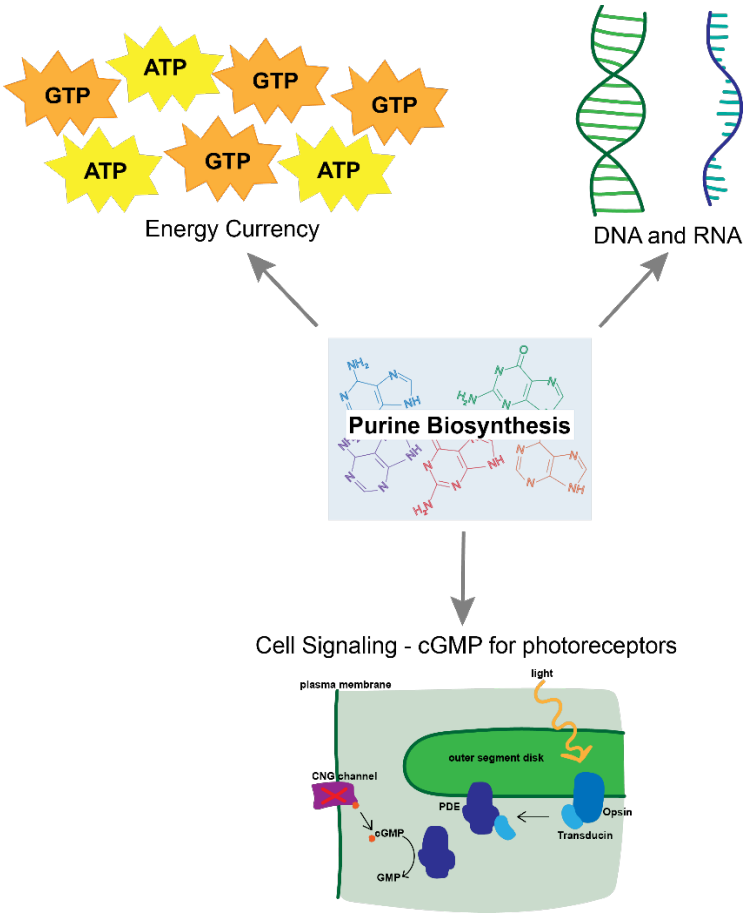

Figure 1.3 Purine biosynthesis can generate nitrogenous bases for ATP, GTP, DNA, RNA, and cGMP.

extensions (Burrell et al., 2022). These extensions help lock the enzyme in a partially open configuration in high GTP environments (Burrell et al., 2022). Retinal IMPDH1 has three phosphorylation sites that control enzyme regulation (Plana-Bonamaisó et al., 2020). Retinal IMPDH1 forms filaments in wild-type zebrafish retina that change in length throughout the day and night (Cleghorn et al., 2022).

Purines bases can be used in cells to make building blocks for DNA and RNA, energy sources (ATP and GTP), and signaling molecules such as cGMP (Fig. 1.3). Mutations in IMPDH could impact these processes and photoreceptors may be especially vulnerable. Although photoreceptors are post-mitotic, they have abundant mitochondria that have mitochondrial DNA. Additionally, approximately 10% of mouse photoreceptor outer segments (which are packed with phototransduction proteins) are turned over daily (Umapathy et al., 2023; Young, 1967). Photoreceptors need to synthesize new proteins for phototransduction, and interruptions in that process may cause issues. Photoreceptors also rely heavily on ATP for energy. During phototransduction, cGMP is used to control CNG channels, and imbalances in cGMP have been associated with retinal degeneration (Farber and Lolley, 1974; Power et al., 2020).

Prior to our work, the leading hypothesis was that some IMPDH1 mutations caused degeneration due to a lack of GTP inhibition (Burrell and Kollman, 2022). Purified mutated IMPDH1 that did not get inhibited with high concentrations of GTP were termed class 1 mutations (Burrell and Kollman, 2022). If IMPDH1 was hyperactive *in vivo*, cGMP levels could be elevated, leading to photoreceptor death. We investigated this possibility with the first IMPDH1 mutant animal models.

Chapter 2 – Daily mitochondrial dynamics in cone photoreceptors

Citation

The work described in this chapter was published in the *Proceedings of the National Academy of Science* (PNAS):

Daily mitochondrial dynamics in cone photoreceptors

M.M. Giarmarco,D.C. Brock,B.M. Robbings,W.M. Cleghorn,K.A. Tsantilas,K.C. Kuch,W. Ge,K.M. Rutter,E.D. Parker,J.B. Hurley,& S.E. Brockerhoff, Daily mitochondrial dynamics in cone photoreceptors, Proc. Natl. Acad. Sci. U.S.A. 117 (46) 28816-28827, https://doi.org/10.1073/pnas.2007827117 (2020).

The PNAS publication and supplementary information are available online:

https://www.pnas.org/doi/abs/10.1073/pnas.2007827117

Introduction

Photoreceptor cells in the retina are highly metabolically active. Their energy demands change throughout the day to support phototransduction (Okawa et al., 2008) and regeneration of outer segment (OS) disks (LaVail, 1976). Photoreceptors consume more energy as ATP in darkness than in light (Okawa et al., 2008) and some additional ATP comes from mitochondrial metabolism (Du et al., 2016).

Energy production can be influenced by mitochondrial fission, fusion, and new growth (mitogenesis). Smaller, fragmented mitochondria typically consume less oxygen (Chen et al., 2005). Mitogenesis is influenced by many factors, including circadian rhythms (Goede et al., 2018). In neurons mitogenesis can occur far away from the cell body (Laar et al., 2018). Mitochondria can form networks (Bleck et al., 2018) and folds of cristae within mitochondria can be remodeled (Cogliati et al., 2016). These dynamic processes contribute to cell health; mitochondrial dysfunction is associated with neurodegenerative diseases (Chen and Chan, 2009; Cieri et al., 2017; Wong et al., 2019), including retinal degeneration (Lefevere et al., 2017; Litts et al., 2015).

Over 90% of glucose taken up by photoreceptors is used for aerobic glycolysis (Ames et al., 1992; Winkler, 1981). Nevertheless, they have a large cluster of mitochondria in the apical portion of the inner segment, the ellipsoid, just below the OS. The density and organization of mitochondrial clusters vary among species, but they are present in photoreceptors of all vertebrates examined, including fish (Tarboush et al., 2014), ground squirrels (Sajdak et al., 2019), mice (Kanow et al., 2017), and humans (Nag and Wadhwa, 2016). In photoreceptors of some species, all mitochondria reside within the cluster, while in mammals with vascularized inner retinas mitochondria are also present at synaptic terminals (Bentmann et al., 2005; Stone et al., 2008). In cultured chicken retinas, mitochondrial dynamics are circadian (J. Y.-A. Chang et al., 2018), but diurnal changes in mitochondrial structure and function in photoreceptors in intact eyes have not been explored. Daily exposure to sometimes intense light and high rates of

energy production suggest that mitochondrial turnover may be important for photoreceptor health. Structural and functional changes to mitochondria could enable photoreceptors to meet increased ATP requirements in darkness.

In this report we describe daily changes that occur in zebrafish cone photoreceptor mitochondria. Zebrafish provide a useful model to dissect mitochondrial dynamics in specific photoreceptor subclasses. Zebrafish undergo typical vertebrate behavioral and biological circadian rhythms (Cahill, 2002; Vatine et al., 2011), and their retinas have four cone subtypes (red, green, blue, and ultraviolet [UV]) organized in a tiered, mosaic pattern. Each cone type can be identified by its unique morphology and position in the outer retina (Raymond et al., 1995), and each maintains a large cluster of mitochondria just below the OS (Tarboush et al., 2014). Our results indicate that mitochondrial clusters in cones undergo diurnal remodeling consistent with enhanced energy production in darkness.

Results

To examine mitochondrial cluster function and dynamics throughout the day, we collected retinas at six timepoints from adult zebrafish under 14-h/10-h light-dark (LD) or 24-h dark (DD) conditions. Retinas were used for imaging and biochemical experiments. Fig. 2.1A illustrates individual cone cell structures with immunohistochemistry (IHC) and electron microscopy (EM). Cone subtypes were differentiated by double cone position, nuclear morphology, and presence of a distinct large mitochondrion at the base of UV cone clusters (Fig. 2.1A, white arrows). At night zebrafish cone ellipsoids and OSs extend distally into the retinal pigment epithelium (RPE); in the morning they retract back toward the nuclear layer. This daily process of retinomotor movements is regulated by light exposure and the circadian clock (Hodel et al., 2006; Menger et al., 2005).

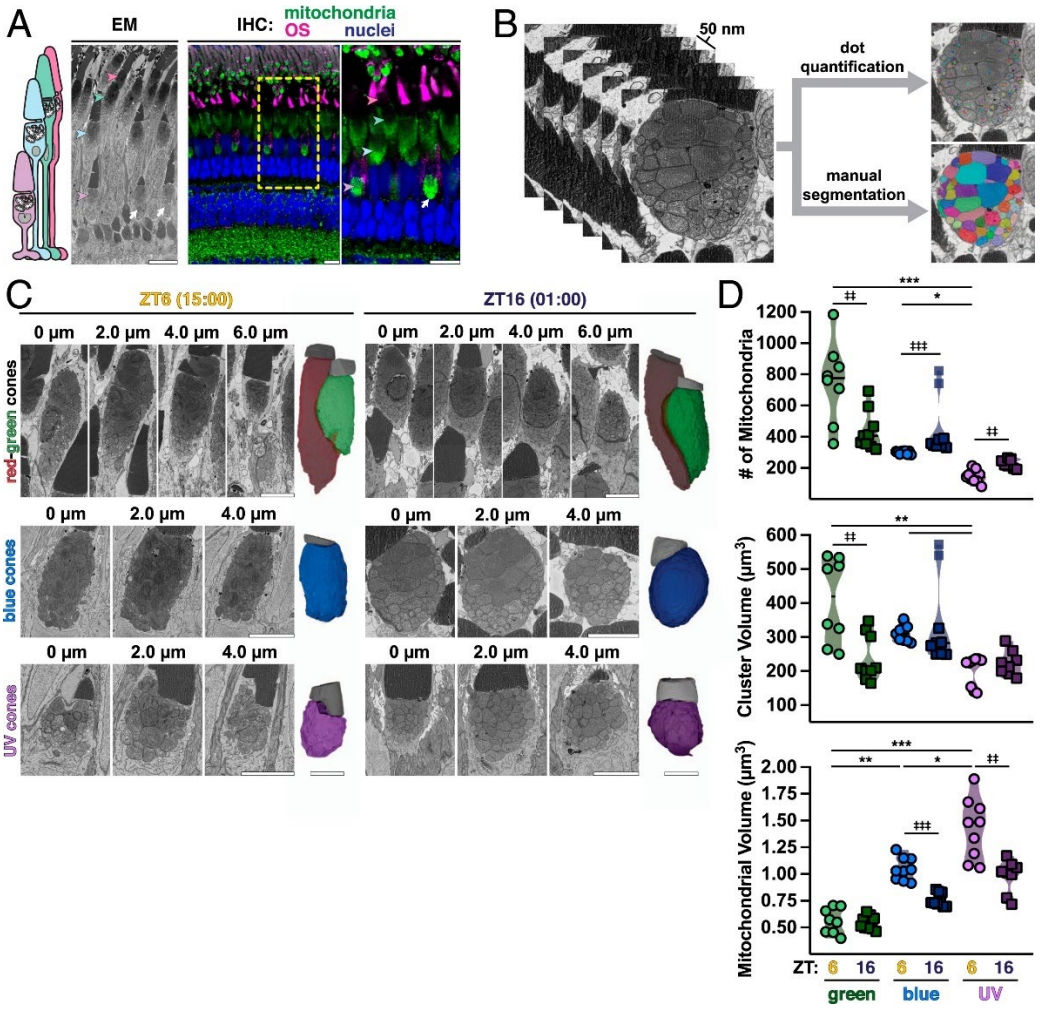

Figure 2.1 At night single cones have more small mitochondria.
A. Schematic of zebrafish cone subtypes (Left), with EM (Middle) and IHC (Right) images of zebrafish outer retina. IHC images are stained for all mitochondria (green), red-green cone OSs (magenta), and nuclei (blue). Arrowheads indicate corresponding UV, blue, green, and red cone mitochondrial clusters; white arrows, megamitochondria at UV cluster bases. Yellow box, zoomed-in area. (Scale bars, 10 µm.)
B. Example 50-nm Z-stack from SBFSEM used for 3D analysis via manual segmentation or rapid dot quantification.
C. Z-stacks from SBFSEM with 3D-rendered mitochondrial clusters (colored) and OSs (gray) from green, blue, and UV cone subtypes in daytime at ZT6 (15:00) and night at ZT16 (01:00). (Scale bars, 5 µm.)
D. Violin plots of mitochondrial number, cluster volume, and mitochondrial volume from dot quantification and manual segmentation; lines represent median. Cone subtypes are represented by respective colors at ZT6 (circles) and ZT16 (squares). *,‡P < 0.05. **, ‡‡P < 0.01. ***,‡‡‡P < 0.001.

Zebrafish Single Cones Have More Small Mitochondria at Night.

We performed detailed three-dimensional (3D) analyses of cone mitochondrial clusters using 50 nm Z-sections collected by serial block-face scanning electron microscopy (SBFSEM) (Fig. 2.1B). Image stacks were analyzed using either a rapid dot quantification method or manual segmentation to compare mitochondrial number, size, shape, and location between day (15:00, Zeitgeber Time 6 [ZT6]) and night (01:00, ZT16). Individual red-green, blue, and UV cone image stacks with corresponding 3D renderings of mitochondrial clusters and OSs at ZT6 and ZT16 are presented in Fig 2.1C.

We found that at night, blue and UV cone mitochondria increase in number by 17 ± 10% and 57 ± 6%, respectively (Fig 2.1D, *Top*). These changes did not coincide with an increase in cluster volume (Fig 2.1D, *Middle*); on average, volumes of individual blue and UV cone mitochondria decreased at night by 29 ± 3% and 31 ± 6%, respectively (Fig 2.1D, *Bottom*). One animal in the study had overall larger cones than all others, and its blue cones were identified as outliers using a robust regression followed by outlier identification test (transparent markers at ZT16 in Fig. 2.1D). For transparency we included these two cones in the analysis, but this did not affect the conclusions. Green cones, which in zebrafish exist in red-green double cones, appeared in two populations at both timepoints. Four animals in our study have very large green cones (>700 mitochondria), while the green cones of four other animals are smaller (300 to 450 mitochondria) (Fig. 2.1D). Despite this bimodal population, mitochondrial volume for green cones is maintained between 0.4 and 0.7 μm^3 at ZT6 and ZT16. This suggests that single and double cone subtypes undergo different cycles of mitochondrial dynamics.

Mitochondrial cluster shape was also examined for each cone subtype using transgenic zebrafish expressing YFP targeted to cone mitochondria (gnat2:mito-cpYFP) (Giarmarco et al., 2017), counterstained with antibodies targeting components of the mitochondrial respiratory chain. Individual cone mitochondrial cluster lengths and circularity ratios were calculated. For all cone types, cluster length increases at night by ~50%, but cluster width, reflected by the

circularity ratio, decreases at this time. Both LD and DD groups exhibited cyclical changes in cluster morphology.

Cone Mitochondria within Clusters Vary in Size and Complexity.

Surface area and volume of each manually segmented mitochondrion was used to calculate mitochondrial complexity index (MCI), a size-insensitive measure of morphological complexity (Vincent et al., 2019). Mitochondria within clusters were heterogeneous in volume and MCI (Fig. 2.2A), and MCI was poorly correlated with volume (Fig. 2.2B). Four individual mitochondria with the same volume but different MCIs are presented in Fig. 2.2C. Compared to mouse cones, zebrafish cone mitochondria are simpler on average but occupy a larger volume.

Mitochondria in Cone Subtypes Are Morphologically Distinct, and More Simple Mitochondria Appear at Night.

Our analyses also revealed morphological distinctions between cone subtypes. Clusters in green cones are longer and have smaller mitochondria (Fig. 1.1D). Fig. 2.2D depict 3D renderings of manually segmented green, blue, and UV cone clusters. At ZT6, green, blue, and UV mitochondria have significantly different distributions of mitochondrial volume, with mitochondrial volumes largest in UV cones and smallest in green cones, but cone subtypes do not have significantly different MCI distributions (Fig. 2.2E).

To compare mitochondrial volume and MCI between day and night, we analyzed manually segmented green, blue, and UV cones at ZT6 and ZT16. At ZT16, mitochondria are significantly smaller in blue and UV cones, but not green cones (Fig. 2.2F). The MCI of all cone subtypes shifts significantly toward having more simple mitochondria at night. These results suggest that green cones can alter their mitochondrial complexity without changing volume.

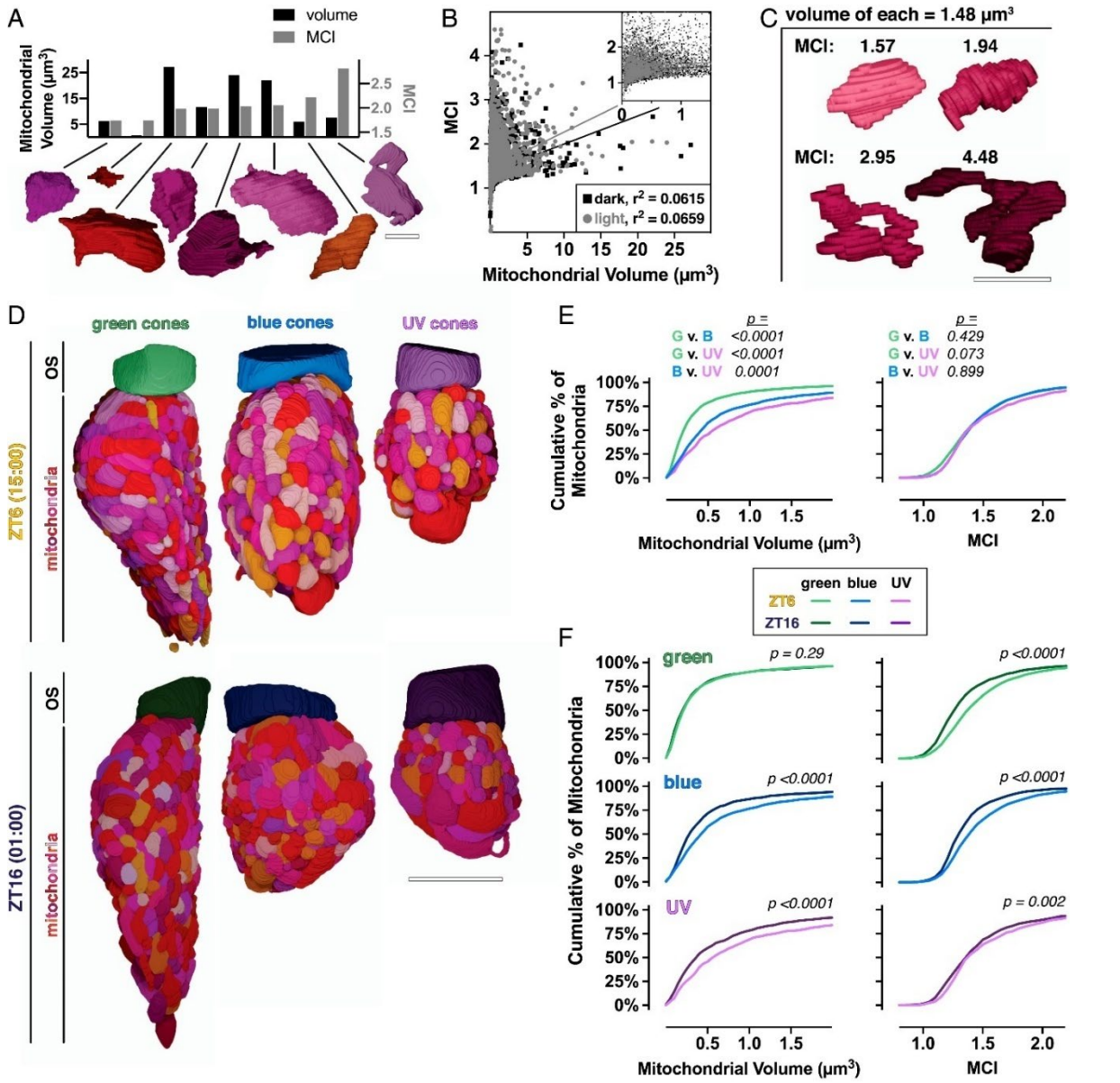

Figure 2.2 At night cones have more simple mitochondria.

A. Three-dimensional renderings of eight manually segmented cone mitochondria with corresponding quantifications of volume (Left axis, black bars) and MCI (Right axis, gray bars). (Scale bar, 2 µm.)

B. Cross-correlation plot of mitochondrial volume and MCI for individual mitochondria at ZT16 (black squares) and ZT6 (gray circles).

C. Three-dimensional renderings of single mitochondria with equal volumes (1.48 μm^3) over a range of MCIs. (Scale bar, 2 µm.)

D. Three-dimensional renderings from manual segmentation of mitochondria and OSs in green, blue, and UV cones at ZT6 and ZT16. (Scale bar, 5 µm.)

E. Cumulative frequency distributions for mitochondrial volume and MCI comparing mitochondria between cone subtypes at ZT6.

F. Cumulative frequency distributions for cone subtypes, comparing mitochondrial volume and MCI at ZT6 (light lines) and ZT16 (dark lines). ZT6 curves are also presented in E.

Megamitochondria Associate in the Cluster Core.

Cones of several species (Knabe et al., 1997; Tyrrell et al., 2019; Utsumi et al., 2020), including zebrafish (Kim et al., 2005), contain large megamitochondria. To examine the distribution of megamitochondria in zebrafish cone clusters, we 3D rendered the three largest mitochondria in manually segmented cones in their respective clusters. In all cone subtypes, megamitochondria localize within the cluster core, often in direct contact (Fig. 3.3A). We did not detect striking differences in megamitochondria between day and night, but note that the volume, location, and complexity of megamitochondria vary between cone subtypes. Megamitochondria in green cones localize to the top of the cluster and are relatively uniform in size and of average complexity. Single cones contain distinct megamitochondria whose volume comprises 12 to 22% of the cluster. We observed several megamitochondria with projections extending toward the cluster periphery, and UV cone megamitochondria are unusually complex.

Mitochondria in the Cluster Core Are Smaller at Night.

To examine the distribution of mitochondrial sizes across the cluster, each mitochondrion from SBFSEM analyses was plotted as a single point in 3D using its center X-Y-Z coordinates (Fig. 2.3B). For manual segmentation, point size was proportional to mitochondrial volume. For dot quantification, point size was proportional to the number of dots needed to track each mitochondrion; larger points represent larger or more branched mitochondria. Points were separated into peripheral and core populations according to distance from the cluster 3D central axis. Similarly, top and bottom populations were defined by proximity to the OS or cluster base. Mitochondrial point sizes were quantified in relation to cluster position (Fig. 2.3C), and ratios of core/periphery and top/bottom were used to assay relative size distribution (Fig. 2.3D).

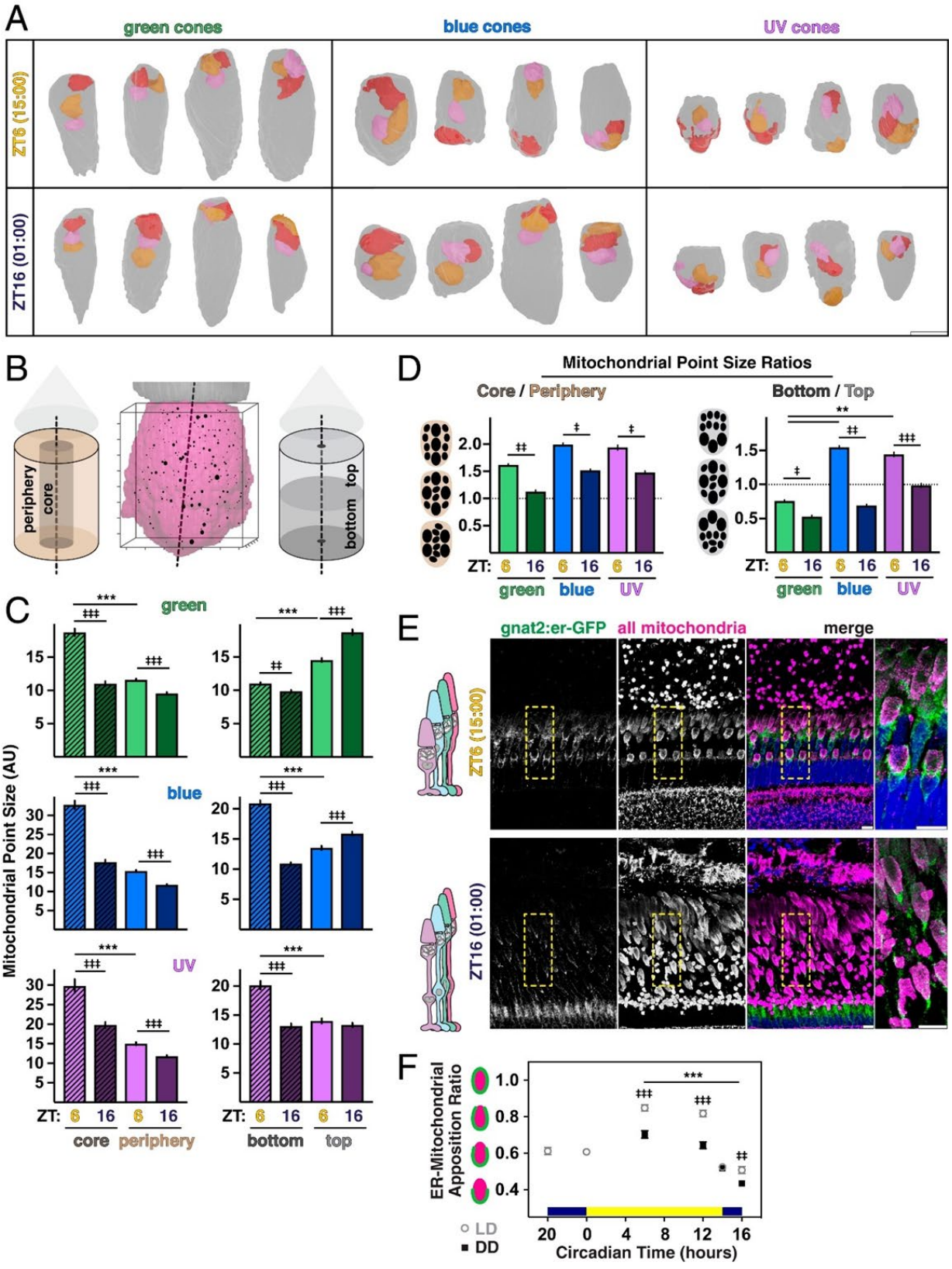
A
green cones
blue cones
UV cones
ZT6 (15:00)
ZT16 (01:00)
B
periphery
core
bottom
top
C
green
blue
UV
Mitochondrial Point Size (AU)
ZT: 6 16 6 16
core periphery
bottom top
D
Mitochondrial Point Size Ratios
Core / Periphery
Bottom / Top
ZT: 6 16 6 16 6 16
green blue UV
E
gnat2:er-GFP
all mitochondria
merge
ZT6 (15:00)
ZT16 (01:00)
F
ER-Mitochondrial Apposition Ratio
LD
DD
Circadian Time (hours)

Figure 2.3 Distribution of mitochondrial size across the cluster changes throughout the day.
A. Three-dimensional renderings of the three largest mitochondria in manually segmented cones at ZT6 and ZT16. OSs are oriented toward the top; ellipsoids, gray. Largest mitochondrion, red; middle, orange and smallest, pink. (Scale bar, 5 μm.)
B. Three-dimensional rendering of cone ellipsoid (magenta) and OS (gray) overlaid with the corresponding point cloud. Individual mitochondria are represented at their X-Y-Z locations; point size corresponds to relative mitochondrial size. Points were separated into core and peripheral or top and bottom populations. Axis ticks, 1 μm.
C. Quantification of mean mitochondrial point size in regions of the cluster for cone subtypes at ZT6 and ZT16.
D. Mitochondrial point size ratios quantifying regional core–periphery and bottom–top distributions of mitochondrial size reported in C for cone subtypes at ZT6 and ZT16. In C and D, ‡P < 0.05; **P < 0.01; ‡‡P < 0.001; ***,‡‡‡P < 0.0001.
E. IHC images of transgenic zebrafish outer retina expressing cone-targeted er-GFP (green) overlaid with mitochondrial and nuclear stains (magenta and blue, respectively) at ZT6 and ZT16. Yellow boxes, zoomed-in areas. (Scale bars, 10 μm.)
F. Quantification of mean ER–mitochondrial apposition in blue and UV cones from IHC for LD or DD groups. ‡‡P < 0.01. ***,‡‡‡P < 0.0001.

At ZT6 cones have significantly more large mitochondria at the cluster core, compared to the periphery (Fig. 2.3C,D *Left*). At ZT16 average mitochondrial point size decreases 30 to 45% in the core and ~30% in the periphery; size also decreases ~35 to 50% at the bottom of the cluster (Fig. 2.3C). Conceptually, this represents a shift toward more small mitochondria at the base of the cluster at night (Fig. 2.3D). Compared to single cones, green cones underwent similar changes to mitochondrial size distribution, but maintain a significantly larger population of small mitochondria at the cluster base (Fig. 2.3D, *Right*). These data suggest that in daytime all cones maintain a population of small mitochondria at the cluster periphery; at night mitochondrial size becomes more uniform across the cluster.

Endoplasmic Reticulum–Mitochondrial Appositions Peak in Daytime.

In other cells the organelle endoplasmic reticulum (ER) initiates mitochondrial fission (Friedman et al., 2011; Korobova et al., 2013), a process that occurs at the end of mitogenesis (Amiri and Hollenbeck, 2008). Zebrafish cone ER primarily contacts mitochondria at the cluster base and periphery (Giarmarco et al., 2017), where mitochondrial size is most dynamic. We

examined the cone ER network surrounding mitochondria at all timepoints. Using sections from LD or DD transgenic zebrafish expressing GFP targeted to cone ER (gnat2:er-GFP) (George et al., 2014), we performed IHC with antibodies against the mitochondrial respiratory chain (Fig. 2.3E). To quantify potential ER contacts for individual blue

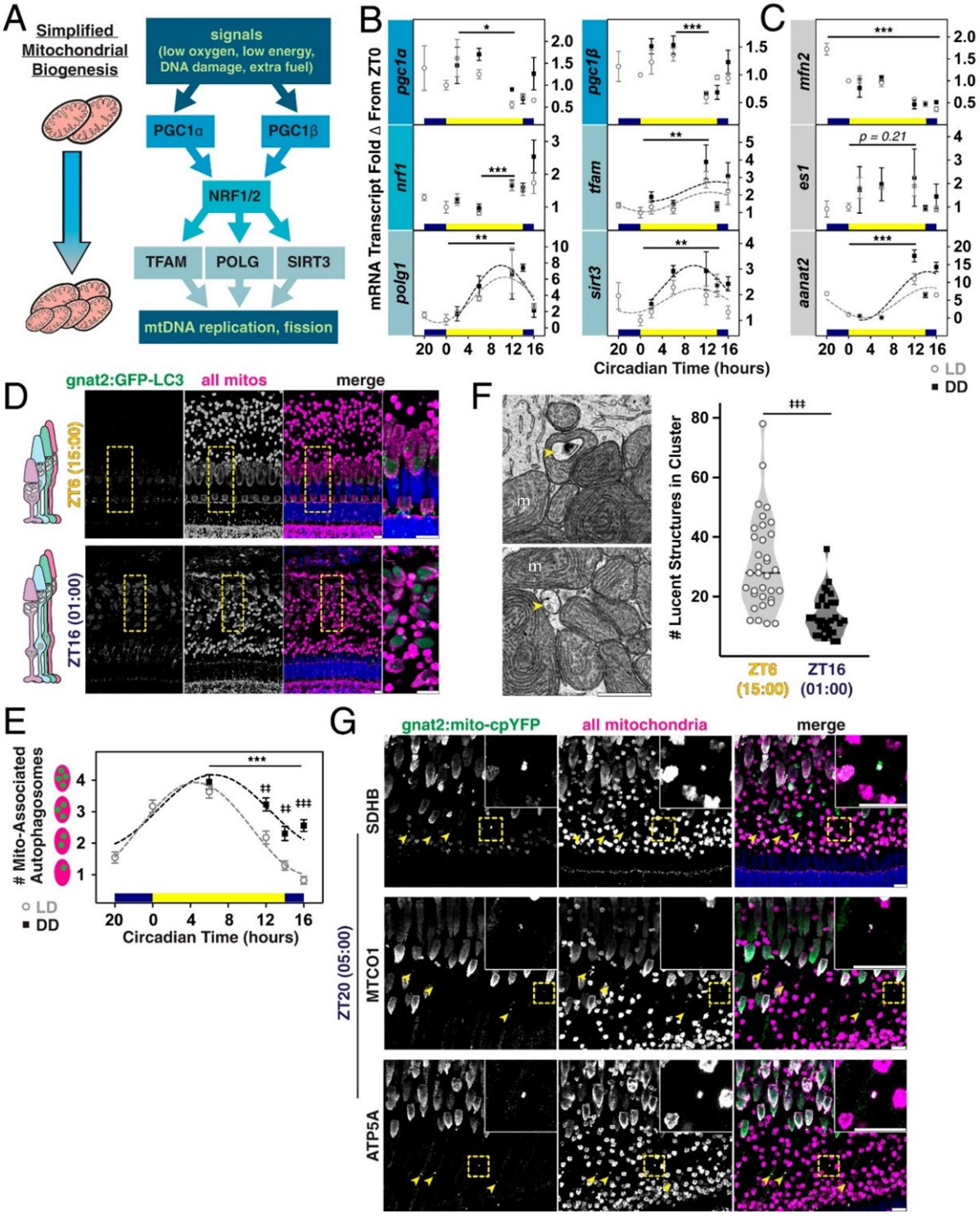

Figure 2.4 Mitogenesis genes peak in the evening, when fewer autophagosomes associate with mitochondrial clusters.
A. Simplified pathway for mitogenesis.
B and C. Quantification of mRNA transcripts from whole retinas measured using qPCR: in B, six mitogenesis genes, and in C, the mitochondrial fusion factor mfn2, the mitochondrial enlargement factor es1, and a control gene aanat2. LD, open circles; DD, black squares. *P < 0.05. **P < 0.01. ***P < 0.0001.
D. IHC images of transgenic zebrafish outer retina expressing cone-targeted GFP-LC3 (green) overlaid with mitochondrial and nuclear stains (magenta and blue, respectively) at ZT6 and ZT16. Yellow boxes, zoomed-in areas. (Scale bars, 10 μm.)
E. Quantification of mitochondrial LC3-positive puncta in blue and UV cones from IHC for LD or DD groups. ‡‡P < 0.001. ***,‡‡‡P < 0.0001.
F, Left. SEM images of lucent autophagosomal structures (yellow arrowheads) inside and between cone mitochondria (m). (Scale bar, 1 μm.)
F, Right. Violin plots quantifying lucent structures in clusters at ZT6 (empty circles) and ZT16 (black squares); lines represent median. ‡‡‡P < 0.0001.
G. IHC images of transgenic cone-targeted mito-cpYFP (green) counterstained for SDHB, MTCO1, or ATP5A (magenta) and nuclei (blue) at 05:00 (ZT20). Yellow arrowheads and Insets indicate mislocalized mitochondria. (Scale bars, 10 μm.)

and UV cone clusters, ER–mitochondrial apposition ratios were calculated by dividing the longest length of ER adjacent to the cluster by the cluster length.

In the daytime, ER tightly associates with the entire cluster surface and is densely packed around its base (Fig. 2.3E, *Top*). At night, apposition ratios decrease as the ER becomes more diffuse and extends less toward the OS (Fig. 2.3E, *Bottom* and Fig. 2.3F). This shows that the ER network changes to accommodate the mitochondrial cluster and is consistent with the shift toward larger mitochondria at the top and periphery of single cone clusters at night (Fig. 2.3D). At most timepoints ER–mitochondrial apposition ratios are lower for the DD group (Fig 2.3F), suggesting that light exposure drives tighter ER–mitochondrial associations.

Mitogenesis Genes Peak before Night Onset.

Increased mitogenesis could result in more cone mitochondria at night. Mitogenesis is controlled at the transcriptional level (Ploumi et al., 2017; Scarpulla et al., 2012): upstream signals lead to mitochondrial DNA (mtDNA) replication, protein synthesis, and fission creating new mitochondria (Fig. 2.4A). We measured mRNA transcript levels of mitogenesis genes using

qPCR with whole retinas (Artuso et al., 2012). The early nuclear transcription factors *pgc1α* and *pgc1β* rise in the morning, while the mitochondrial transcription factor *tfam*, DNA polymerase *polg1*, and deacetylase *sirt3* all peak before night onset (Fig. 2.4B). Together this suggests that canonical mitogenesis increases at night in whole retinas.

Transcripts encoding the mitochondrial fusion protein *mfn2* rise in the morning (Fig. 2.4C, *Top*), suggesting fusion could mediate the corresponding decrease in mitochondrial number in cones; a recent study found that cones contribute roughly half of the mitochondrial proteins in adult zebrafish retina (Hutto et al., 2020). No significant changes were detected in the zebrafish cone mitochondrial enlarging factor *es1* (Masuda et al., 2016) (Fig. 2.4C, *Middle*). As a control we examined *aanat2* (Wang et al., 2015), which displays robust circadian changes in expression (Fig. 2.4C, *Bottom*). Transcript levels between LD and DD groups were similar, and *tfam*, *polg1*, and *sirt3* met statistical cutoffs for rhythmicity, indicating that retinal expression of mitogenesis genes is regulated primarily by the circadian clock.

Mitochondrial-Associated Autophagosomes Peak in Daytime.

A selective form of autophagy called mitophagy clears damaged or unnecessary mitochondria (Youle and Narendra, 2011). While several pathways can trigger mitophagy (Kawajiri et al., 2010; Strappazzon et al., 2015), all coalesce on recruitment of LC3 to maturing mito-autophagosomes. We performed IHC at all timepoints using LD or DD transgenic zebrafish expressing GFP fused to LC3 in cones (gnat2:GFP-LC3) (George et al., 2014) and antibodies against the mitochondrial respiratory chain (Fig. 2.4D). LC3-positive autophagosomes overlapping with blue and UV cone mitochondrial clusters were quantified. The number of mitochondrial-associated autophagosomes increases twofold at light onset (Fig. 2.4E). While changes to autophagosome numbers met statistical cutoffs for circadian rhythmicity, more mitochondrial-associated autophagosomes were present in the DD group in the evening, possibly indicative of enhanced mitochondrial turnover in prolonged darkness.

When viewed using EM, autophagosomes appear as lucent, multivesicular structures (Fig. 2.4F, *Left*, yellow arrowheads), while mitochondria are electron dense and contain cristae folds. We validated our IHC findings by quantifying the number of electron-lucent structures in all cone mitochondrial clusters imaged using SBFSEM. More lucent structures are present in clusters at ZT6 (Fig. 2.4F, *Right*), when more mitochondrial-associated autophagosomes were detected using IHC. Several clusters contain >30 lucent structures in the daytime, suggestive of a mitophagic event at this timepoint.

Cone Mitochondria Mislocalize toward the Cell Body Hours before Light Onset.

Degraded mitochondrial material canonically enters the endolysosomal pathway (Strappazzon et al., 2015), but in neurons it can translocate and leave the cell (Davis et al., 2014; Melentijevic et al., 2017). Mitochondria mislocalize toward the nucleus in degenerating human cones (Litts et al., 2015) and in a zebrafish cone model of mitochondrial calcium overload (Hutto et al., 2020). Four hours before light onset (05:00, ZT20), we observed mislocalized cone mitochondria using IHC with gnat2:mito-cpYFP transgenic zebrafish and three different mitochondrial respiratory chain markers (Fig. 2.4G, yellow arrowheads). The structures are feasibly the size of a single mitochondrion (0.5- to 1-μm length), contain both cone mito-cpYFP and respiratory proteins, and lie between the cluster and the nucleus. They were present only at overnight timepoints ZT16 and ZT20, and in multiple animals over two generations. While we could not unequivocally identify these structures in SBFSEM, mitochondrial trafficking may occur between the cluster and cell body prior to light onset.

Mitochondria Share Material and Extrude It from the Cell in Darkness.

In nearly all cones, we found dark deposits inside and between mitochondria throughout the day in SBFSEM images (Fig. 2.5A, *Top*). Similar deposits are present in published EM images of cone mitochondrial clusters in other zebrafish (figure 2 of (Tarboush et al., 2014)),

walleye (figures 5 and 7 of (Januschka et al., 1987)), frogs (figure 2 of (Mercurio and Holtzman, 1982)), pigeons (figure 16 of (ISHIKAWA and YAMADA, 1969)), shrews (figures 2, 7, and 10 of (Lluch et al., 2003)), and ground squirrels (figure 5 of (Sajdak et al., 2019)), as well as mice and albino zebrafish. When manually segmented and 3D rendered, we found these electron-dense lamellar whorls can span several micrometers, contacting the matrices of multiple mitochondria and/or the OS (Fig. 2.5A, *Bottom*). Most deposits lie inside of single mitochondria, but they appear in the cytosol and occasionally cross the plasma membrane (Fig. 2.5B, *Top*). This apparent extrusion most often occurs as single events, but some cells displayed multiple concurrent exit sites (Fig. 2.5B, *Bottom*).

Other neurons can eject mitochondrial material via nanotunnel-like extensions (Melentijevic et al., 2017). Three-dimensional analysis revealed that in cones, extruded material either remains near the cell surface or forms stalks that can reach 5 μm, terminating in diffuse lamellar extracellular sacs (Fig. 2.5C, *Top*). The stalks appear as 40- to 90-nm electron-dense rings surrounding a hollow core. In the extracellular space stalks and sacs can connect, creating networks that link discrete populations of mitochondria within a cluster (Fig. 2.5C, *Bottom*). These deposits and their extrusion in darkness were observed in nearly all cones but seldom in rods; in one instance extrusion was observed in two neighboring rods (Fig. 2.5D).

To quantify cone mitochondrial deposits and extrusion events in day and night, we used a ranking system to blindly score clusters imaged with SBFSEM. The presence of mitochondrial deposits is similar between day and night (Fig. 2.5E, *Left*). However, extrusion events occur almost exclusively at night, and most cells had multiple events (Fig. 2.5E, *Right*). While the

composition of the deposits is not known, they provide a physical link between cone mitochondria and the interphotoreceptor matrix (IPM).

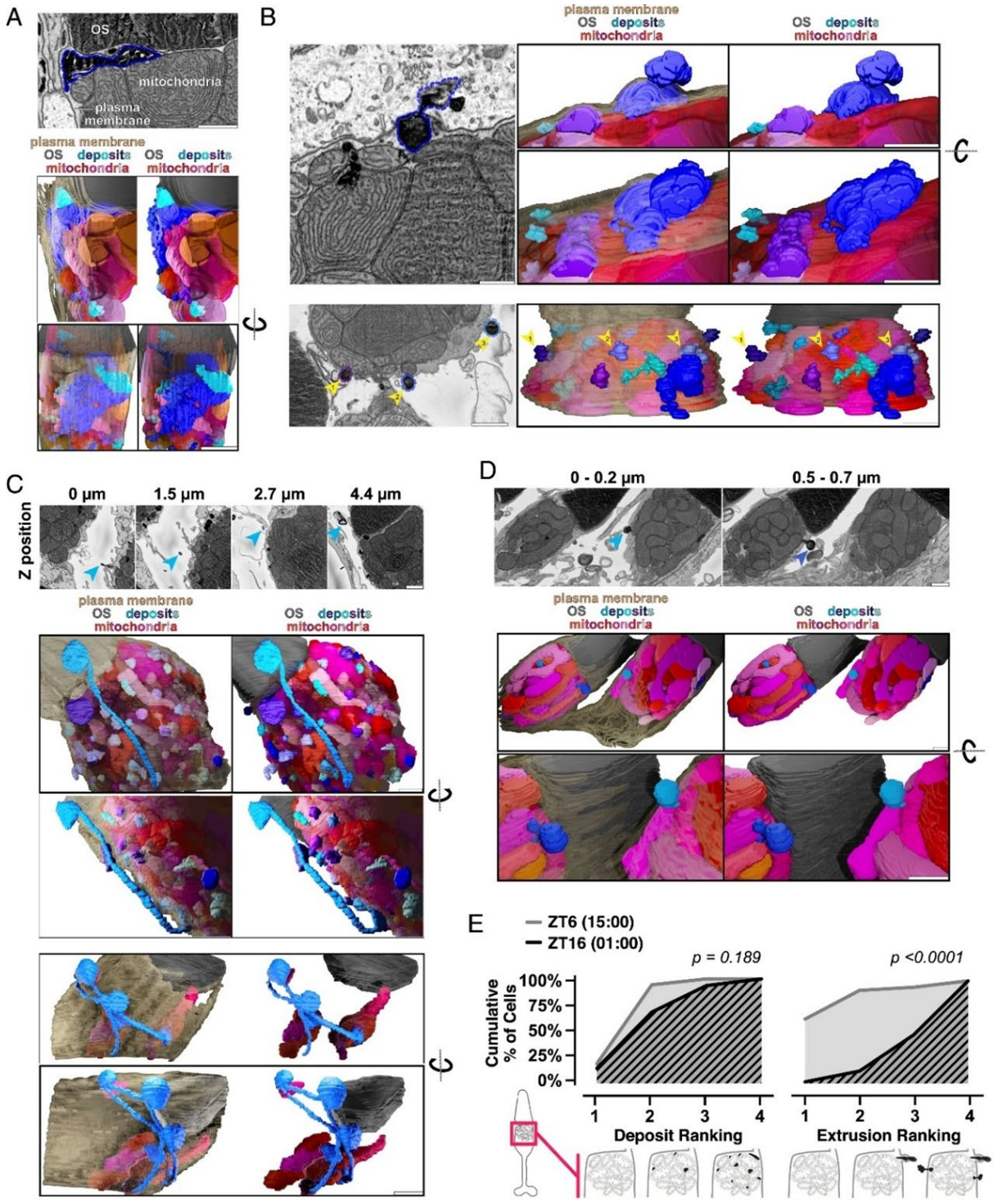

Figure 2.5 Mitochondria share material and extrude it from the cell in darkness.
A. SBFSEM image (Top) of deposits associated with cone mitochondria and corresponding 3D renderings (Bottom). One large deposit (blue outline) below the OS is associated with multiple mitochondria.
B. SBFSEM images showing extrusion of mitochondrial-associated deposits from cones, with 3D renderings. (B, Top) Extrusion of one deposit (blue outline). (B, Bottom) Multiple extrusion events in one cell (blue-violet outlines, yellow arrows).
C. SBFSEM images showing stalks and networks in the extracellular space, and corresponding 3D renderings. (C, Middle) One extruded deposit tethered to mitochondria by a stalk (blue arrows). (C, Bottom) Branched network of extruded material contacting three distinct populations of cone mitochondria from one cell.
D. Extrusion of mitochondrial-associated deposits from two neighboring rods. (D, Top) SBFSEM minimum intensity projections over 0.2-μm depth highlighting extrusion events (blue arrows). (D, Bottom) Three-dimensional rendering. (All scale bars, 1 μm.) Beige, plasma membrane; gray, OSs; reds, mitochondria; blues, deposits.
E. Quantification of deposits and extrusion events at ZT6 (gray) and ZT16 (black). For deposits: 1 (no mitochondrial deposits) to 4 (every mitochondrion having a deposit). For the number of extrusion events: 1 (no events) to 4 (more than three events).

Mitochondrial Succinate Metabolism Is More Active in Darkness Due to Altered Succinate Dehydrogenase Activity.

Mitochondrial metabolism in whole mouse retinas is more active in darkness (Du et al., 2016). However, ~96% of photoreceptors in mouse retinas are rods (Tsukamoto et al., 2001), while zebrafish retinas have ~50% cones (Larison and Bremiller, 1990; Raymond et al., 2014). To measure mitochondrial activity in cones, we performed enzyme histochemistry with fresh-frozen retina sections from LD or DD albino zebrafish collected throughout the day. Some albino mouse (LaVail et al., 1987) and zebrafish (Vihtelic et al., 1999) strains undergo light-induced retinal degeneration, but under normal facility lighting our albino zebrafish display healthy central retinal morphology and mitochondrial clusters. Activities of succinate dehydrogenase (SDH, complex II) and cytochrome *c* oxidase (COX, complex IV) were assayed separately (Andrews et al., 1999); their roles in mitochondrial metabolism are highlighted in Fig. 2.6A. Histochemistry was performed for all timepoints in parallel, and stain intensities of single cones were measured from light microscopy images (Fig. 2.6B).

While COX activity remains robust and stable throughout the day, SDH activity in cones increases 25 to 30% in darkness (Fig. 2.6C). SDH activity in the DD group is elevated at all

times of day, suggesting possible repression of SDH activity by light in cones. Additionally SDH activity appears primarily in red-green double cones, compared to strong COX activity observed in all cone subtypes, rods, and the inner retina (Fig. 2.6B, arrowheads).

As validation, we used metabolite labeling coupled with gas chromatography mass spectroscopy (GC/MS) to assay activity of SDH in light- or dark-adapted zebrafish retinas around ZT6. Whole retinas were incubated with U-^{13}C labeled succinate (dark green boxes, Fig. 2.6A), which SDH converts to U-^{13}C fumarate; fumarate is readily interconverted to malate via

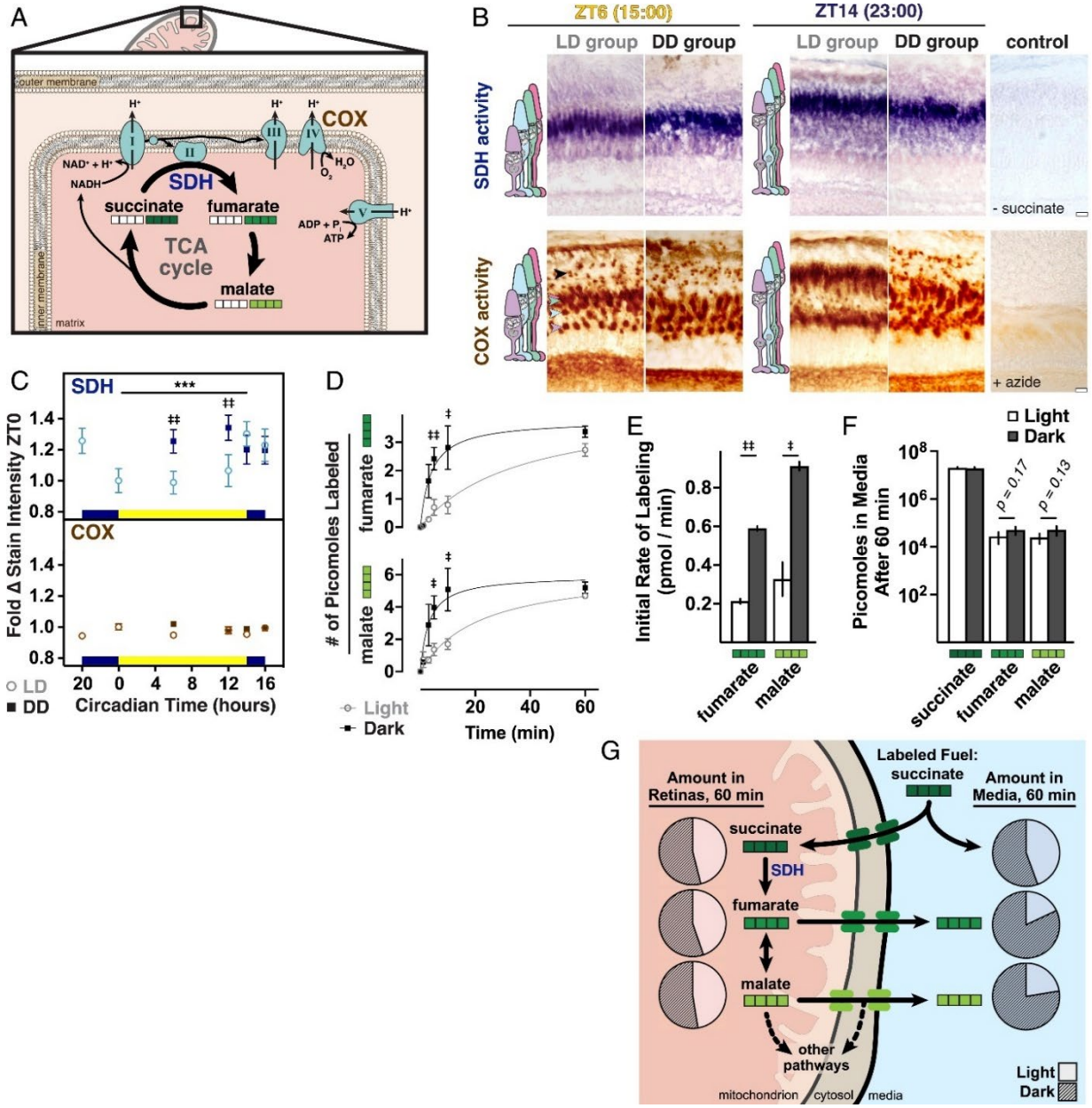

Figure 2.6 Mitochondrial metabolism is more active in darkness due to altered SDH activity.
A. Schematic of SDH in the tricarboxylic acid (TCA) cycle and electron transport chain, including COX also assayed in B. White squares represent 12C carbons; green squares,13C carbons for labeling experiments (D–F).
B. Light microscopy images of histochemical staining for SDH (blue) and COX (brown) activities. Shown are frozen sections from albino zebrafish at ZT6 and ZT14 (23:00) from LD and DD groups. Negative controls lacked substrate or contained an inhibitor. Arrowheads indicate corresponding cone subtype and rod (black) mitochondrial clusters. (Scale bars, 10 μm.)
C. Quantification of mean SDH and COX stain intensities in single clusters from LD (open circles) or DD (dark squares) groups; data normalized to ZT0. ‡‡P < 0.001. ***P < 0.0001.
D. Mean incorporation of 13C label from U-13C succinate into fumarate and malate. Whole retinas from light- or dark-adapted zebrafish were incubated in U-13C succinate in light or dark; 13C incorporation was determined with GC/MS.
E. Initial rates of formation of fumarate and malate from U-13C succinate in light and dark from the first 5 min of incubation. In D and E, ‡P < 0.05; ‡‡P < 0.001.
F. Amounts of U-13C-labeled succinate, fumarate, and malate in media after 60-min light or dark incubation with retinas in U-13C succinate.
G. Schematic of steady-state metabolites inside and outside of retinas after 60-min incubation with labeled succinate. Pie charts denote relative amounts of metabolites in light (unfilled areas) and dark (filled areas).

the enzyme fumarase (Andersen, 1980). Labeled fumarate and malate accumulate faster in dark-adapted retinas (Fig. 2.6D). A 2.75-fold higher initial rate of formation for both fumarate and malate (Fig. 2.6E) is consistent with higher SDH activity in darkness observed using histochemistry. To determine if succinate uptake was altered in darkness, we assayed labeled metabolites in media after 60 min, but did not find significantly lower amounts of labeled succinate (Fig. 2.6F). Fig. 2.6G depicts steady-state metabolite labeling in retinas and media after 60 min in light or darkness; succinate levels are similar in light and dark, but metabolites downstream of SDH accumulate in the media.

Discussion

Comparisons of Cone Mitochondria between Species and Cone Subtypes.

In zebrafish cones, hundreds of heterogeneous mitochondria pack between the nucleus and OS (Tarboush et al., 2014). In this report we quantified mitochondrial number, size, complexity, and 3D distribution in zebrafish cone subtypes. Compared with mouse cones (Sloat et al., 2016), zebrafish cone mitochondria are more numerous, smaller, and densely packed,

with elaborate cristae patterning (Perkins et al., 2003). The dense packing and disparate mitochondrial volumes between cone subtypes may reflect nutrient and oxygen access in the avascular zebrafish retina (Stone et al., 2008); double cones closer to the RPE and blood supply could fuel more mitochondria. These spatial constraints, the high SDH activity we observed in double cones, and previous studies showing unique metabolic activity in short-wavelength cones (Kam et al., 2019; Nork et al., 1990) suggest that diverse metabolic strategies support cone subtypes.

Half the animals in our SBFSEM study had larger green cone mitochondrial clusters than the others; the same retinal area was imaged for all animals and single cones did not display this feature. Retinomotor movements occur in cone subtypes at slightly different times (Menger et al., 2005), so our timepoints may have captured intermediate states for green cones. Alternately, zebrafish green cones may exist as multiple subtypes. Blue and UV cones in zebrafish each express one form of the light-sensitive protein opsin; green cones express four opsins across the adult retina (Chinen et al., 2003; Takechi and Kawamura, 2005), but single-cell analysis is needed to determine if green cone subtypes exist.

Mitochondrial Size in Photoreceptors.

Mitochondrial size is linked to energetic output; in other cells smaller mitochondria respire less (Chen et al., 2005; Maryanovich et al., 2015). However, in zebrafish cones small, morphologically simple mitochondria may contribute more toward energy production. Zebrafish single cone mitochondria are smaller and simpler at night, when energy demands and mitochondrial respiration are likely highest. Small mitochondria in cones populate the cluster periphery, closest to oxygen and fuels. Cristae in these small mitochondria generally display the organized, linear structure linked to higher energetic output (Perkins et al., 2003).

Like other species (ISHIKAWA and YAMADA, 1969; Knabe and Kuhn, 1996) zebrafish cones form megamitochondria, maintained by the enlargement factor ES1 (Masuda et al., 2016;

Utsumi et al., 2020). We did not detect changes to *es1* mRNA transcripts in whole retinas, but observed juxtaposed megamitochondria in all cones throughout the day. The biological role of megamitochondria is unknown, but their densely packed cristae suggest roles beyond canonical respiration (Slautterback, 1965). Membrane lipids concentrated in megamitochondrial cristae can form a conduit for oxygen (Desaulniers et al., 1996; Urschel and O'Brien, 2008). Many cone megamitochondria exhibit a central body with projections extending toward the cluster periphery; these projections toward the ER could be a site for mitogenesis (Knabe and Kuhn, 1996). Further, cone megamitochondria (Knabe et al., 1997; Lluch et al., 2003) and mitochondrial-derived ellipsosomes (MacNichol et al., 1978; Nag and Bhattacharjee, 1995) in other species guide light toward the OS. Zebrafish visual sensitivity is regulated by light and the circadian clock (Li and Dowling, 1998), so daily mitochondrial rearrangements may contribute to vision.

Mitochondrial Turnover in Photoreceptors.

Maintenance of healthy mitochondria and mtDNA is crucial, particularly in the retina. mtDNA mutations (Lefevere et al., 2017) and disrupted autophagy (Rodríguez-Muela et al., 2015) are associated with retinal degeneration, and aging human cones accumulate mtDNA mutations and mitochondrial abnormalities (Barron et al., 2001; Nag and Wadhwa, 2016). In some forms of age-related macular degeneration, cone mitochondrial clusters remodel and mitochondria translocate toward the nucleus (Litts et al., 2015).

Genes required for mitogenesis (Scarpulla et al., 2012) undergo circadian changes in retinal expression in a manner that supports mitogenesis at night onset, although it is unknown which retinal cell(s) this occurs in. At ER–mitochondrial contact sites the ER stimulates mitophagy (Hamasaki et al., 2013) by recruiting autophagic machinery (Huang et al., 2018) and initiating mitochondrial fission (Friedman et al., 2011). In single cones, ER concentrates around the cluster during the day, when clusters contain more autophagosomes and fewer

mitochondria. Together this suggests that cones undergo daily mitochondrial turnover involving ER.

SDH Activity and Potential Regulation in the Retina.

Fewer mitochondria during the day could result in the reduced cone SDH activity we detected using histochemistry. Zebrafish cones have higher SDH activity than other retinal cells, consistent with studies of human (Andrews et al., 1999; Barron et al., 2001) and salamander retinas (Moore and Gruberg, 1974). Cone SDH activity increases at night, when regulation from the zebrafish circadian clock (Cahill, 2002; Li et al., 2008) could promote mitochondrial succinate uptake (Cai et al., 2019). However, we did not find evidence of increased succinate uptake in darkness, and frozen sections used for histochemistry don't require transporters for substrate uptake. Thus, our observations of cone SDH activity likely resulted from changes to expression or posttranslational modifications, rather than succinate availability.

Light (Gu et al., 2002; Popov et al., 2010) and time of day (Akimoto et al., 2005; Reddy et al., 2006) can affect SDH expression in other cells. Additionally, SDH can be regulated by competitive inhibition (Ackrell et al., 1974; Potter and DuBois, 1943), phosphorylation (Acín-Pérez et al., 2014; Nath et al., 2015), acetylation (Cimen et al., 2010), and succinylation (Park et al., 2013). mRNA transcripts for the mitochondrial deacetylase SIRT3 increase in retinas prior to night onset, but regulation of SDH by SIRT3 in retinas has not been explored. In photoreceptors, both SIRT3 and the mitochondrial desuccinylase SIRT5 are necessary for normal function (Lin et al., 2016). Further, cristae structure can influence respiration (Cogliati et al., 2016; Guo et al., 2018), in part by driving SDH supercomplexation (Liu et al., 2018). SDH catalyzes a reversible reaction in mouse retinas (Bisbach et al., 2020a); we used succinate to quantify forward capacity of SDH.

Mitochondrial Deposits in Photoreceptors.

In photoreceptors, whorled deposits contact the matrices of multiple mitochondria. The deposits are distinct from melanosomes; they are present in albino zebrafish photoreceptors. We did not investigate their composition, but they resemble osmiophilic structures observed in and around mitochondria of other cells, proposed to have roles in lipid metabolism (figure 8 of (Blanchette-Mackie and Scow, 1983) and figure 4 of (Tarlow et al., 1977)), mitochondrial degradation (Soubannier et al., 2012; Sugiura et al., 2014), and peroxisome synthesis (Sugiura et al., 2017). Further, ER stacks can encircle mitochondria, forming a lamellar structure to initiate mitophagy (Huang et al., 2018). Collectively this suggests that photoreceptor mitochondrial deposits may mediate lipid homeostasis and/or mitochondrial clearance.

Nightly Extrusion of Mitochondrial Material.

Mitochondrial deposits are extruded from cones at night. The events we report are morphologically distinct from photoreceptor endocytosis (Hollyfield et al., 1985; Hollyfield and Rayborn, 1987), exocytosis (Rea et al., 2004; Wen et al., 2017), and from published examples of mitochondrial extrusion in other cells (Gasko and Danon, 1972; Géminard et al., 2002; Lyamzaev et al., 2008; Simpson and Kling, 1968; Unuma et al., 2015). Unlike these events, extrusion of cone mitochondrial deposits shows no evidence of fusion with the plasma membrane, and the released material remains associated with the cell surface and underlying mitochondria.

The extruded material can connect to the extracellular space via thin stalks that terminate in diffuse lamellar sacs. Neurons have been reported to release and tether mitochondrial material (Davis et al., 2014; Melentijevic et al., 2017) via thin stalks ~200 nm wide and terminal multivesiculate sacs of ~3-μm diameter. The extracellular structures attached to photoreceptors are smaller (~60-nm stalks and ~1-μm sacs), and sacs do not contain vesicles. The stalks are smaller than tunneling nanotubes (Gerdes and Carvalho, 2008), which can transport mitochondria (Lu et al., 2017; Sartori-Rupp et al., 2019; Wang and Gerdes, 2015).

Photoreceptors can exchange proteins via an unknown mechanism (Ortin-Martinez et al., 2017), but we did not observe connections between cones. The extracellular structures could link cones to the IPM, a scaffold of carbohydrates and bound proteins (Hollyfield, 1999; Ishikawa et al., 2015) where cones occupy a distinct metabolic microenvironment (Adler and Southwick, 1992; Johnson et al., 1986). At night the zebrafish outer retina becomes disorganized by retinomotor movements, so the extracellular structures could physically anchor cones to the IPM.

In summary, we report a quantitative analysis of daily mitochondrial dynamics in cone photoreceptors. At night, when energy demands are likely highest, a mitogenesis event in retinas precedes increases in cone metabolic activity and the number of small mitochondria in single cones. During the day, mitochondrial number decreases, perhaps mediated by fusion and/or mitophagy. We also report a dense lamellar material that is shared between mitochondria and extrudes from the cell at night, sometimes forming extracellular networks. These daily changes to cone mitochondria can support energy production at night, regulated by light and the circadian clock. This study did not include phototransduction mutants or lengthy dark adaptation; differences we report between LD and DD groups could be attributed to effects of light masking and/or master circadian rhythms (Altimus et al., 2010; Mrosovsky et al., 1999). Elucidating the makeup of mitochondrial deposits, regulation of SDH, role of ER–mitochondrial contacts, and rates and locations of mitochondrial turnover in healthy cones will contribute to an understanding of how mitochondrial abnormalities in aging and disease affect vision.

Materials and Methods

Zebrafish Maintenance and Retina Collection.

Research was authorized by the University of Washington Institutional Animal Care and Use Committee. Wild-type, transgenic, and albino adult zebrafish were maintained on a 14-

h/10-h light/dark cycle. Twenty-four hours prior to experiments, fish were fasted in either continuous darkness (DD) or standard room light (LD).

Serial Block-Face Scanning Electron Microscopy.

Wild-type or albino zebrafish eyes were fixed and prepared in resin blocks as described previously (Kanow et al., 2017). Serial sections were cut at 50-nm thickness and imaged in the outer retina, 100 to 200 μm from the optic nerve. Z-stack images were processed and measured using the TrakEM2 plugin for ImageJ (research resource identifier [RRID]:SCR_008954).

Immunohistochemistry.

Albino or transgenic zebrafish eyes were fixed, cryosectioned, stained, and confocal imaged as described previously (Hutto et al., 2020). Z-stacks from each timepoint were blindly analyzed using ImageJ (RRID:SCR_002285).

Quantitative PCR.

RNA was extracted from wild-type zebrafish eyes, reverse transcribed into cDNA, and analyzed using qPCR. Cosinor curves fitted to each dataset were used to determine circadian rhythmicity according to cutoff values (more than twofold change and $P < 0.05$ from ANOVA analysis) (DeVera and Tosini, 2020); data meeting this cutoff display dashed lines.

Enzyme Histochemistry.

Histochemical enzyme activity was assayed similarly to previous studies in human (Andrews et al., 1999) and mouse retina (Chinchore et al., 2017). Briefly, albino zebrafish eyes were dissected, frozen in optimal cutting temperature compound and cryosectioned for parallel staining. SDH and COX activity stain solutions were applied for 10 min at 37 °C, then washed,

mounted, and imaged with a light microscope. Stain intensity of single cones was blindly quantified using ImageJ.

Isotopic ^{13}C Succinate Labeling and Mass Spectrometry.

Light- or dark-adapted wild-type zebrafish eyes were dissected and incubated in 1 mM D-[U-^{13}C]-succinate with 1 mM unlabeled glucose for the specified timepoints, then washed in phosphate buffered saline and flash frozen in liquid nitrogen. Metabolites were extracted from retinas, derivatized, and analyzed using GC/MS.

Data Analysis.

Data were processed using Microsoft Excel (RRID:SCR_016137); statistical tests were performed using GraphPad Prism (RRID:SCR_002798). The 3D renderings and animations from SBFSEM were created using Blender (RRID:SCR_008606) ("OSF | Giarmarco_PNAS_2020_rawdata.zip," n.d.).

Data Availability

Single cell data from IHC, SBFSEM, histochemistry, succinate labeling data have been deposited in Open Science Framework (https://osf.io/qaed8).

Acknowledgments

Funding for this work was provided by the University of Washington (UW) Art and Rita Levinson undergraduate research scholarship (D.C.B.), NIH NEI 5T32-EY007031 (M.M.G. and K.M.R.), NIH NEI R01-EY026020 (S.E.B.), NIH NEI R01-EY06641 (J.B.H.), NIH NIA T32-AG000057 (K.A.T.), and UW Vision Core grant NIH NEI P30-EY001730 (to Maureen Neitz). We thank Amandeep Dhami, Ashlee Evans, Carson Adams, Stephanie Sloat, and Alexey Merz for

help with data analysis and thoughtful discussion; Stan Kim provided zebrafish care at the UW Institute for Stem Cell and Regenerative Medicine Aquatics Center.

Chapter 3 – Cone photoreceptors transfer damaged mitochondria to Müller glia

Citation

The work described in this chapter was published in the *Cell Reports*:

Cone photoreceptors transfer damaged mitochondria to Müller glia

R.A. Hutto, K.M. Rutter, M.M. Giarmarco, E.D. Parker, Z.S. Chambers, S.E. Brockerhoff, Cone photoreceptors transfer damaged mitochondria to Müller glia, Cell Reports 42 (2) 112115, DOI: 10.1016/j.celrep.2023.112115 (2023).

The *Cell Reports* publication and supplementary information are available online: https://www.cell.com/cell-reports/fulltext/S2211-1247(23)00126-2

Introduction

Mitochondrial dysfunction is a pathological marker for neurodegenerative diseases. Mitophagy is a key strategy that cells use to maintain healthy mitochondria. One form of mitophagy involves the transfer of damaged mitochondria for transcellular degradation (transmitophagy). In neurons, transmitophagy was first reported between retinal ganglion cell axon mitochondria and adjacent astrocytes (Davis et al., 2014). Recent findings demonstrate the physiological role of this process in Alzheimer's disease (Lampinen et al., 2022) and in maintaining healthy dopaminergic neurons (Morales et al., 2020). Transmitophagy is also critical for nonneuronal cells. In adipocytes, the transfer of damaged mitochondrial fragments to macrophages mitigates the negative consequences of thermogenesis-induced reactive oxygen species (ROS) (Rosina et al., 2022).

Photoreceptor (PR) cells are the postmitotic retinal neurons responsible for detecting light and initiating shape-detecting vision. Mitochondria are abundant in PRs presumably due to the significant energy requirements of these cells, particularly in the dark (Okawa et al., 2008). Mitochondria are concentrated in the ellipsoid region of the cell and are thought to remain in this region (Hoang et al., 2002). PRs reside in an oxidative environment near the choroidal blood supply. The high energy demands, oxidative stress, and long-lived presence of PRs necessitate robust strategies to remove and replenish damaged mitochondria.

Here, we developed three stress models to determine how mitochondrial homeostasis in cone PRs is affected by chronic stress. We exploited the zebrafish model due to the abundance of cones and live-imaging capabilities. In addition, recent work indicates that cone PRs are more sensitive to oxidative stress than rods (Azuma et al., 2022). Cones also use more ATP than rods (Ingram et al., 2020), likely making them more susceptible to mitochondrial dysfunction.

Our results show that cone mitochondria respond similarly to different stress paradigms. This includes migration away from the ellipsoid, acidification, and transcellular transfer to Müller glia (MGs). This phenomenon is also detected in unstressed cones but at lower levels. Our

research has uncovered transmitophagy in cones as a response to mitochondrial damage and it adds to the repertoire of functions attributed to MGs. We propose that this response increases under stress and helps explain the robustness of the cone PR.

Results

Mitochondria in cone PRs are mislocalized after stress

We examined mitochondrial mislocalization across different mitochondrial stress paradigms using cone-specific gnat2:mtmKate2 transgenic zebrafish to visualize cone mitochondria.

We induced stress by treating zebrafish larvae with chloramphenicol, an inhibitor of mitochondrial RNA translation (Shichino and Iwasaki, 2022) (Fig. S3.1A–C), or cold (16℃), which increases ROS in fish neural tissue (Tseng et al., 2011) (Fig. S3.1D). Both stresses caused mislocalization of mitochondria away from the ellipsoid (Fig. 3.1A,B).

Since chloramphenicol and cold affect whole larvae, we developed a method that induces stress only in cone PRs. We generated a transgenic zebrafish strain that expresses mitochondrial-targeted Killer Red (KR) only in cone PRs (gnat2:mtKR). KR produces superoxide radicals when exposed to 540–590 nm light (Bulina et al., 2006). We paired this transgene with gnat2:mtBFP fish to visualize cone mitochondria. To prevent KR activation during early development, we minimized exposure to 420–650 nm light up to 4 days postfertilization (dpf) before then exposing larvae to 565 nm LED pulses from 4 to 6 dpf (Fig. 3.1C). Our activation strategy increased ROS production in cones (Fig. 3.1D) and caused significant mislocalization of mitochondria in larvae with activated mtKR (mtKR+, LED+) but not in larval cones with inactivated mtKR (mtKR+, LED) or in larval cones treated with LED exposure but not expressing mtKR (mtKR, LED+) (Fig. 3.1E).

To ensure that the mitochondrial mislocalization we observed is not caused by cell death, we used both Tg(TBP-GAL4;UAS:- secA5-YFP) fish (van Ham et al., 2010) and TUNEL

staining. Secreted Annexin5 in the secA5-YFP fish accumulates on the outer surface of the plasma membrane of early apoptotic cells. Neither mtKR expression or LED treatment significantly increased the number of secreted Annexin5 positive (secA5+) cone PRs (identified by gnat2:mtBFP expression; Fig. 3.1F and S3.1E). There were very few mislocalized mitochondria in secA5+ cells; the increase in mislocalized mitochondria of activated mtKR fish occurred in secA5 cells (Fig. 3.1G). Similarly, TUNEL staining did not increase (Fig. 3.1H and

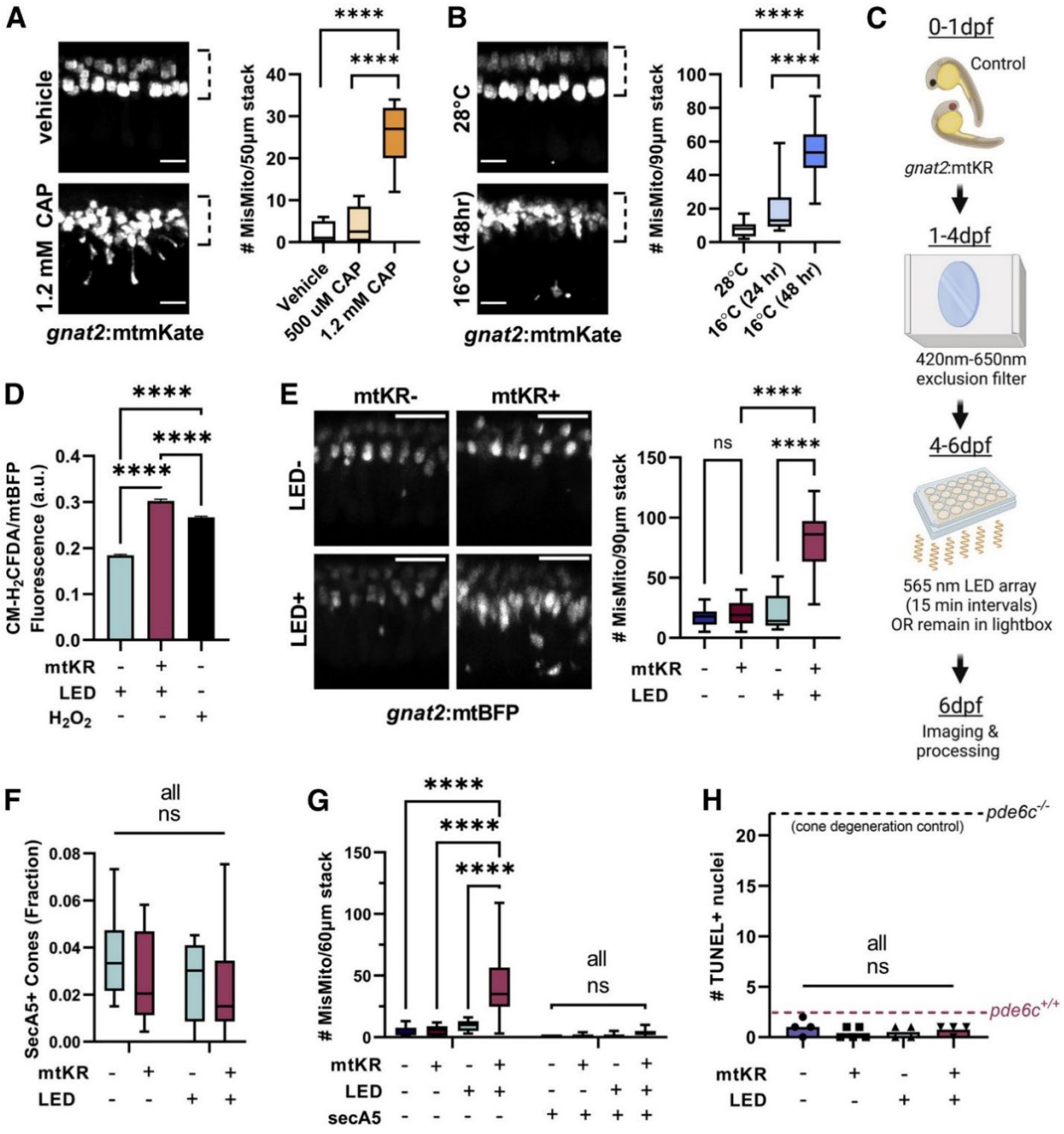

Figure 3.1 Stress causes mislocalized mitochondria in cones
(A) Chloramphenicol (CAP) causes cone mitochondria (*gnat2*:mtmKate) to migrate away from the ellipsoid region (dotted line). Mislocalized mitochondria were quantified per fish. n = 11 fish for vehicle and 1.2 mM CAP conditions and n = 8 for 500 µM CAP. ****p < 0.0001 using one-way ANOVA. Scale bar: 5 µm.
(B) Cold (16°C) causes cone mitochondria to migrate from the cone ellipsoid (dotted line). Mislocalized mitochondria were quantified per fish. n = 10 28°C, n = 6 16°C (24 h), and n = 20 16°C (48 h) fish. ****p < 0.0001 using one-way ANOVA. Scale bar: 5 µm.
(C) Schematic for *gnat2*:mtKillerRed (mtKR) experiments. Embryos were put in a chamber reducing 420–650 nm light to prevent KillerRed activation while maintaining light/dark cycles. At 4 dpf, fish were either kept in the chamber or put on a plate above an LED array of 565 nm light. After 48 h, fish were processed/imaged.
(D) CM-H_2DCFDA fluorescence in cone mitochondria (*gnat2*:mtBFP) shows increased mitochondrial ROS upon *gnat2*:mtKR activation. Fluorescence was normalized to mtBFP to correct for depth in the eye. ****p < 0.0001 with one-way ANOVA. mtKR−: 26,035 mitochondrial clusters from 8 eyes, mtKR+: 24,144 clusters from 13 eyes, and H_2O_2: 40,632 clusters from 15 eyes.
(E) Only mtKR fish activated by the LED array (mtKR+, LED+, see protocol in C) have increased cone mitochondrial mislocalization. Cone mitochondria labeled with *gnat2*:mtBFP. Scale bar: 10 µm. n = 13 fish for mtKR−, LED− and mtKR+, LED+; n = 16 for mtKR+, LED−; and n = 14 for mtKR−, LED+. ****p < 0.0001 with one-way ANOVA.
(F) Quantification of secreted Annexin5+ (secA5; apoptotic) cones, identified by the presence of *gnat2*:mtBFP. Neither LED treatment nor mKR activation is associated with cone cell death. Total cones in a 60 µm stack were estimated by quantification of ellipsoid mitochondrial clusters across n = 5 fish. All comparisons are not significant (ns) with two-way ANOVA. mtKR−, LED−: n = 6; mtKR−, LED+: n = 9; mtKR+, LED−: n = 8; mtKR+, LED+: n = 19.
(G) Increases in mislocalized mitochondria (*gnat2*:mtBFP) upon mtKR activation were only observed in non-apoptotic cells (secA5−). Few mislocalized mitochondria were found in apoptotic cells. Same n as (F). ****p < 0.0001 with a two-way ANOVA.
(H) TUNEL+ nuclei across a 10 µm slice from 6 dpf eyes. No difference detected regardless of LED exposure or the presence of mtKR. Positive control is the *pde6c*$^{-/-}$ cone degeneration model (black dotted line) and negative control is *pde6c*$^{+/+}$ wild-type (WT) sibling (magenta dotted line). n = 4 for all but mtKR+, LED− (n = 5). All comparisons are ns with one-way ANOVA.

S3.1F). In contrast, we observed increased cell death and more mislocalized mitochondria in dying cells after chloramphenicol or cold treatment (Fig. S3.1G-L). Because of these findings, we conducted our studies primarily with gnat2:mtKR fish, and we used the mtKR, LED+ fish as the control for mtKR+, LED+ fish.

Mislocalized cone mitochondria can be found both inside and outside of cones

mtKR LED activation led to substantial visible morphological changes to mitochondria (Fig. 3.2A). Many cone mitochondria appeared translucent due to reduced cristae and possible

swelling (Fig. 3.2A, right panel). Abnormal mitochondria resided both within and outside of the ellipsoid region, unlike healthy electron-dense mitochondria, which we only observed within the ellipsoid region (Fig. 3.2B). In controls, there were few unhealthy mitochondria outside of the

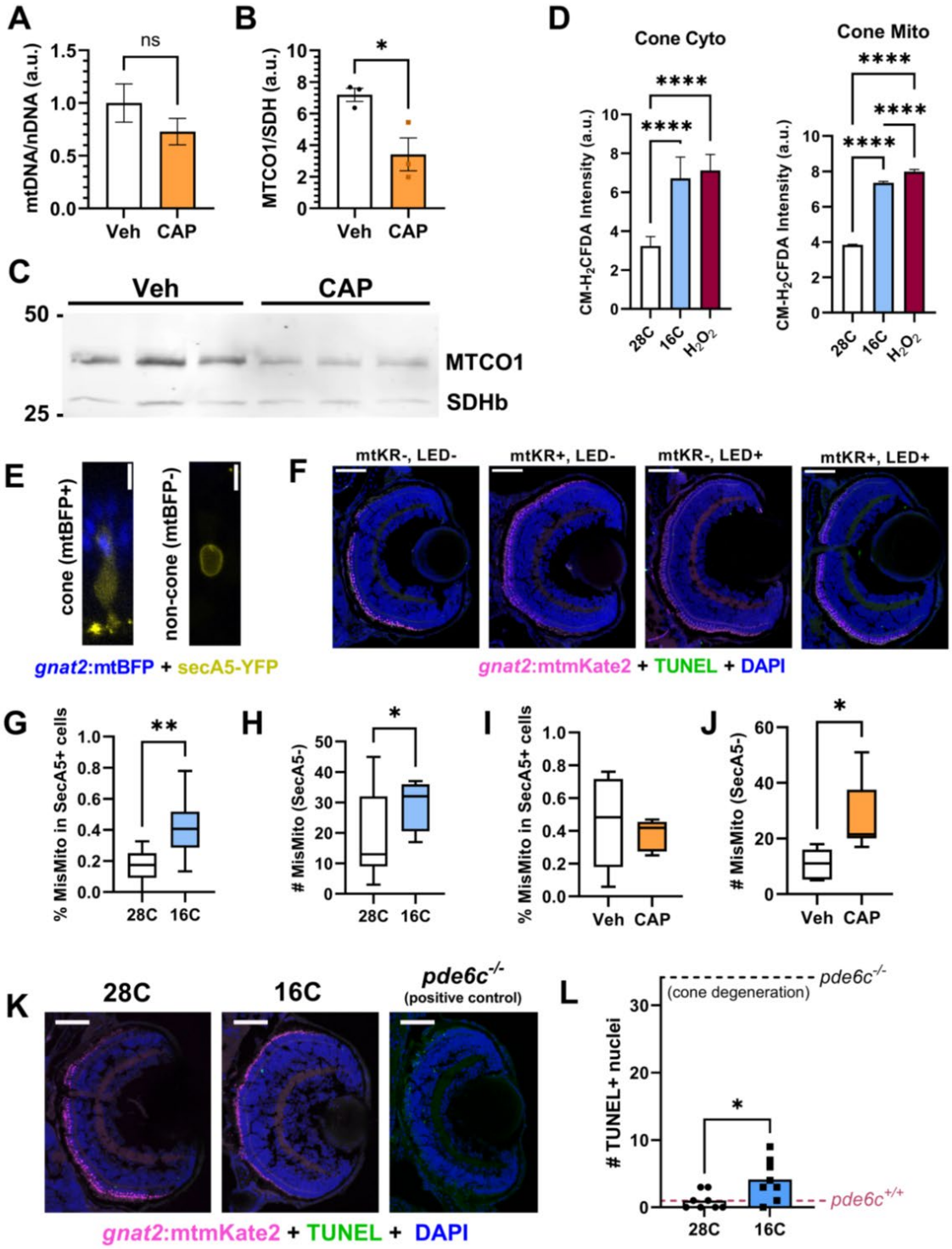

Supplemental Figure 3.1 Cell death and phenotypes associated with different stressors.
A. qPCR quantification of mtDNA(mt-ND1)/nDNA(*polg1*) ratio in vehicle and CAP-treated fish, normalized to Veh=1. n=5 Veh, n=4 CAP samples of DNA from 10 independent pooled larval samples. ns using an unpaired t-test.
B. Quantification of *mtco1* (mitochondrial-encoded) and *sdhb* (nuclear-encoded). n=3 samples of protein isolate from 6 independent pooled larval samples for each condition. Blot is cropped from 25 kDa to 50 kDa. *p<0.05 using an unpaired t-test.
C. Western blot of MTCO1 (higher MW) and SDHb (lower MW) used in B. Blot is cropped from 25 kDa to 50 kDa.
D. Analysis of cytoplasmic and mitochondrial ROS at 28°C and 16°C using CM-H2DCFDA and markers for cone mitochondria (*gnat2*:mtBFP) and cone cytosol (*gnat2*:tdTomato). H2O2 is a positive control. ****p<0.001 and ***p<0.01 using Kruskal-Wallis test (non-normal distribution). 28°C: n= 210 cell slices, 39592 mitochondria from 5 eyes; 16°C: n=201 cell slices, 34372 mitochondria from 6 eyes; H2O2: n=282 cell slices, 40679 mitochondria from 7 eyes.
E. Examples of secA5-YFP+ cells. Cells containing any *gnat2*:mtBFP were designated as cones. Scale=5 μ m.
F. TUNEL stain (green) of Tg(*gnat2*:mtmKate2) (magenta) fish showing very few TUNEL+ nuclei (blue) in any retinal layers regardless of KillerRed expression or LED exposure. Scale=50 μ m
G. Fraction of mislocalized cone mitochondria (*gnat2*:mtBFP) found in secA5+ (apoptotic) cells in 28°C and 16°C fish. *p<0.05 using Welch's t-test. n=11 28°C fish and n=10 16°C fish.
H. Count of mislocalized cone mitochondria in secA5- cells, which increases in cold stress. *p<0.05 using Welch's t-test. n=11 28°C fish and n=10 16°C fish.
I. Fraction of mislocalized cone mitochondria (*gnat2*:mtBFP) found in secA5+ cells in vehicle and CAP-treated fish. ns with Welch's t-test. n=8 vehicle fish, 6 CAP-treated fish.
J. Count of mislocalized cone mitochondria in secA5- cells, which increases with CAP treatment. *p<0.05 using Welch's t-test. n=8 vehicle fish, 6 CAP-treated fish.
K. TUNEL stain (green) of Tg(*gnat2*:mtmKate2) (magenta) fish showing a modest increase in TUNEL+ nuclei (blue) following cold stress. Scale=50 μ m
L. Quantification of TUNEL+ nuclei from panel K. Experimental slices were run with a positive control (*pde6c*-/- cone degeneration model, black dotted line) and negative control (*pde6c*+/+ WT sibling, magenta dotted line). N=8 for both conditions. *p<0.05 using Welch's t-test.

ellipsoid. All mitochondria outside the ellipsoid appeared damaged, as in response to mitochondrial Ca2+ stress (Hutto et al., 2020).

We predicted that mislocalized mitochondria would be found primarily within cone PRs. To our surprise, some were partially or completely outside cone PRs (Fig. 3.2C,D). These were present with and without mtKR, but mtKR increased the number of both intra- and extracellular mislocalized mitochondria (Fig. 3.2D). Mislocalized cone mitochondria were present even outside the PR layer (Fig. 3.2C,E). The identity of mislocalized fluorescence was further

confirmed as mitochondria by colocalization with the mitochondrial protein cytochrome c oxidase 1 (MTCO1) (Fig. 3.2F) (Giarmarco et al., 2020).

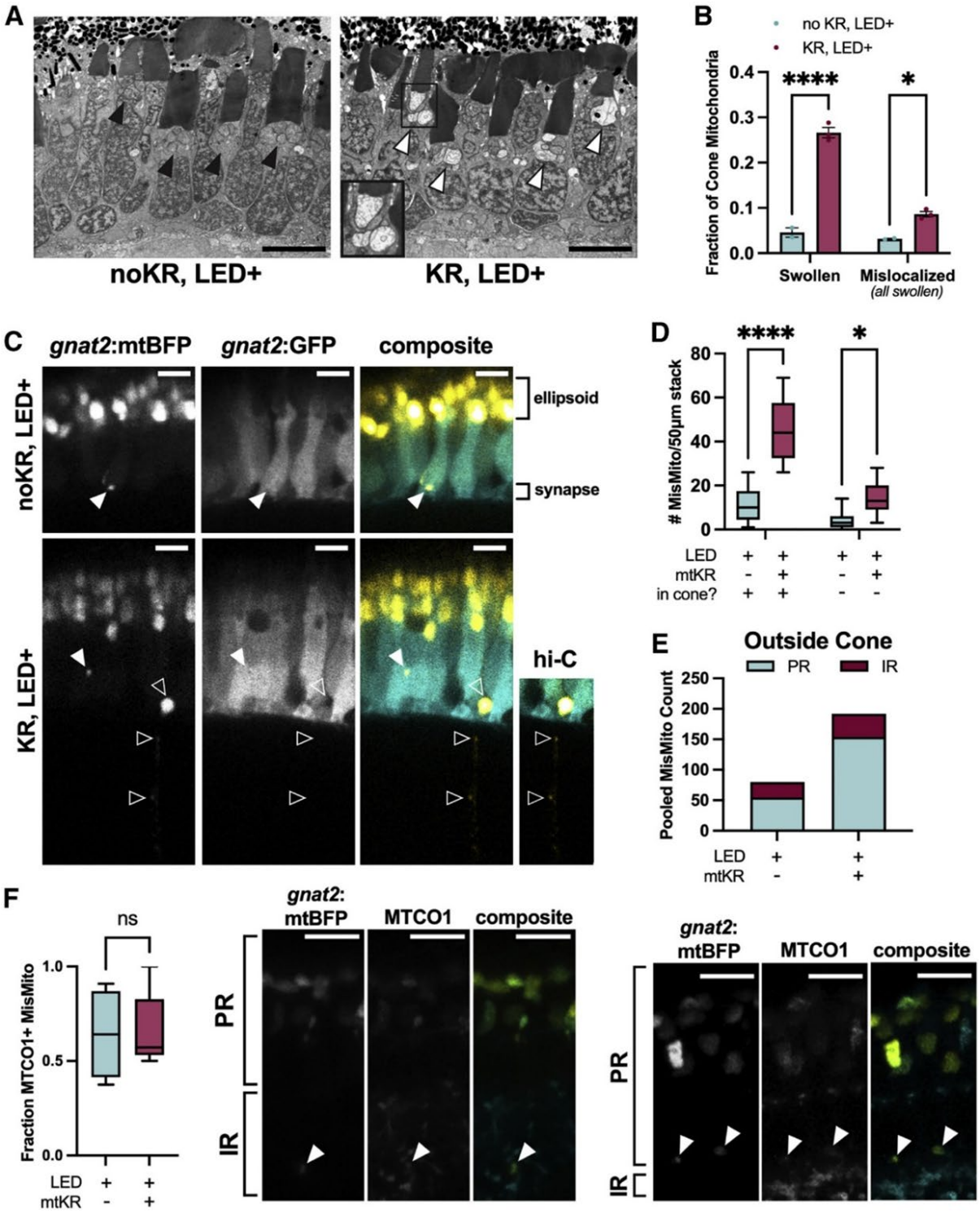

Figure 3.2 Mislocalized mitochondria are abnormal and reside in and outside of cone photoreceptors
(A) Transmission electron micrographs taken at the optic nerve. Cones with activated mKR have many mitochondria with disturbed, swollen morphology both in and outside of the ellipsoid clusters; an inset (black box) shows a cone ellipsoid containing multiple swollen mitochondria. Black arrowhead: ellipsoid cluster with typical mitochondria morphology, white arrowhead: ellipsoid cluster with swollen mitochondria. Scale bar: 5 μm.
(B) Quantification of individual cone mitochondria from slices in (A). A greater fraction of mitochondria are swollen and mislocalized in mKR+ cones. All mislocalized mitochondria had swollen morphology. n = 2 kR− fish (641 and 759 total mitochondria) and n = 3 kR+ fish (520, 613, and 566 total mitochondria). $^{*}p < 0.05$ and $^{****}p < 0.0001$ using a two-way ANOVA.
(C) Imaging of Tg(*gnat2*:mtBFP, *gnat2*:GFP) fish reveals that mislocalized cone mitochondria reside inside cones (filled arrowheads) and partially or completely outside of cones (unfilled arrowheads). Hi-C, high-contrast to enhance visibility of mitochondria. Scale: 5 μm.
(D) Quantification of mislocalized mitochondria by colocalization of cone GFP; cone− includes mitochondria that appear partially or completely out of cones (see C). mtKR increases cone mitochondria number both inside and outside cones. $^{*}p < 0.05$ and $^{****}p < 0.0001$ using a two-way ANOVA. n = 13 fish each condition.
(E) Pooled cone-mislocalized mitochondria totals across all fish binned by retinal region. IR, inner retina; PR, photoreceptor layer.
(F) Immunohistochemistry images of mislocalized mitochondria (filled arrows) colocalized with MTCO1 in PR and inner retina IR. Fraction of mislocalized cone mitochondria colocalized with mitochondrial protein, MTCO1. mKillerRed−: 74 mislocalized mitochondria from 4 eyes mtKillerRed+: 104 mislocalized mitochondria from 5 eyes. Comparisons are ns with unpaired t test. Scale: 5 μm.

MGs contain mislocalized cone mitochondria

These findings prompted us to ask if cone mitochondria were present within MGs. MG cells are resident glia that extend radially across all cellular layers of the retina and have many essential roles (Reichenbach and Robinson, 1995). MGs closely associate with PRs; their outer limiting membrane (OLM), which is formed by tight junctions between MGs, forms extensive contacts with PR inner segments.

After mtKR activation, mitochondria from cones were within MG processes (visualized using Tg(GFAP:GFP) fish) in the PR layer and in the inner retina (IR) closer to the MG cell body (Fig. 3.3A,B). The total number of mislocalized mitochondria both inside and outside of MGs increased compared with controls (Fig. 3.3C), although the fraction of cone mitochondria within MGs was not significantly different between cones with mtKR vs. cones without it (Fig. S3.2A). In vivo imaging captured migration of a cone mitochondrion into an MG (Fig. 3.3D).

These findings indicate that many cone mitochondria that leave cones are taken up by MGs. The increase in the number of cone mitochondria in MGs due to ROS production in cone mitochondria suggests that we have revealed a transfer process that normally occurs under basal conditions and that increases in response to stress.

As further support for a normal transfer process that is stimulated by stress, we used a new mtKR activation strategy with a 24 h LED treatment followed by shielding from activating wavelengths. Transfer of mitochondria to MGs increased during the first 24 h to approximately 40% before stabilizing (Fig. S3.2B). We asked whether microglia, which can phagocytize apoptotic PRs and debris, also take up mislocalized cone mitochondria. In both control and mtKR-activated fish containing the microglial transgene Tg(mpeg1:GFP)gl22 (Ellett et al., 2011), there were very few cone mitochondria detected in microglia (Fig. S3.2C), consistent with the low levels of cell death associated with mtKR activation.

Longitudinal sections from serial block-face (SBF) scanning electron microscopy (EM) stacks of activated mtKR retinas revealed several mislocalized mitochondria between cones that resemble the damaged morphology of mitochondria within cones (Fig. 3.3E). A top-down stack collected from an activated mtKR fish shows an abundance of damaged mitochondria between cones at the position of the OLM (Fig. 3.3F). 3D reconstruction confirmed that these cone mitochondria are indeed within MGs and found near the OLM as well as near the PR synaptic layer (Fig. 3.3G). We also captured what appeared as extrusion of damaged mitochondria (Fig. S3.2D). Reconstruction suggests entry into a neighboring MG cell (Fig. S3.2E). Additional mitochondrial extrusion events from other cones are documented by single EM images (Fig. S3.2F and S3.2G).

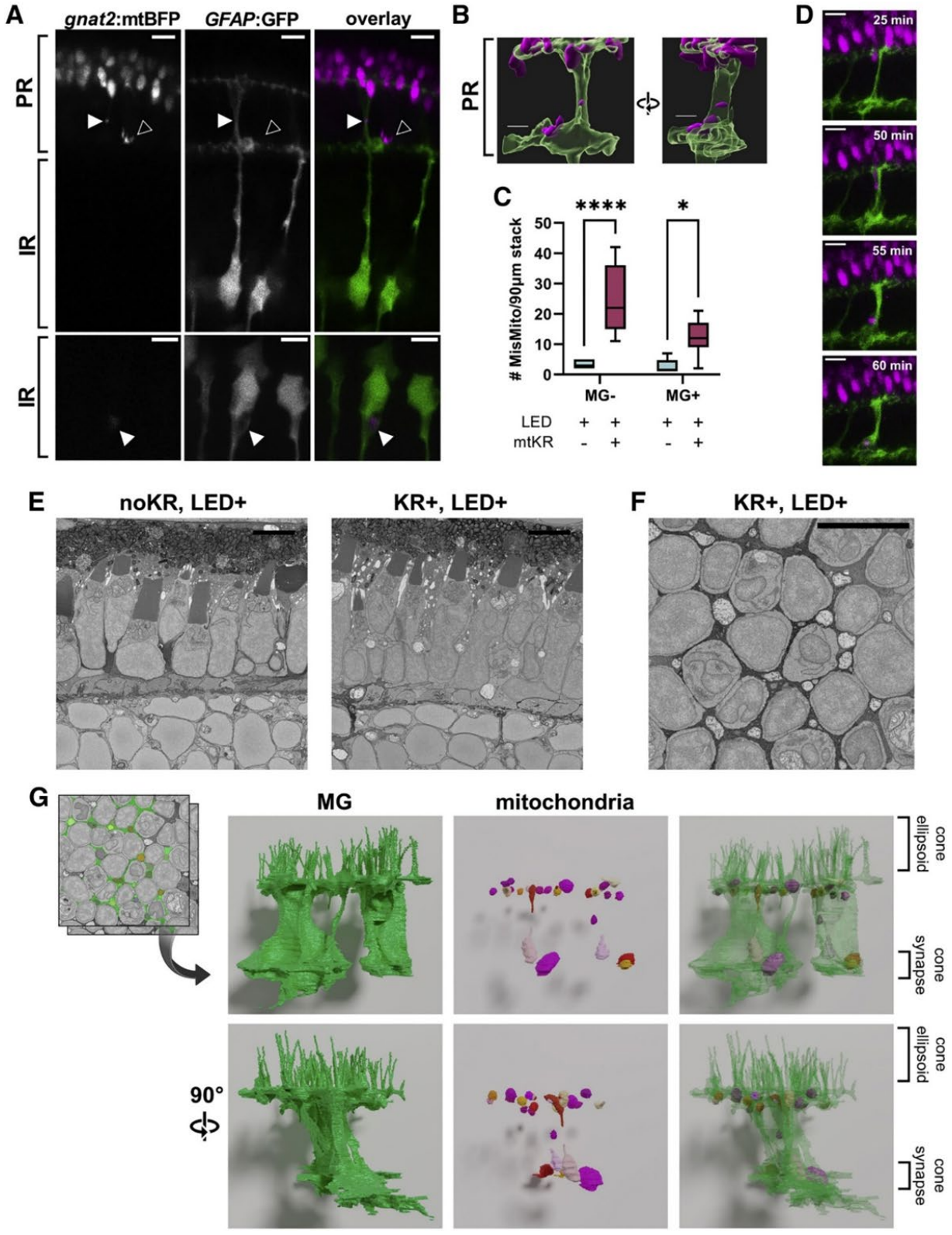
A
gnat2:mtBFP
GFAP:GFP
overlay
PR
IR
IR
B
PR
C
****
*
MisMito/90µm stack
50
40
30
20
10
0
MG-
MG+
LED + + + +
mtKR - + - +
D
25 min
50 min
55 min
60 min
E
noKR, LED+
KR+, LED+
F
KR+, LED+
G
MG
mitochondria
cone ellipsoid
cone synapse
90°
cone ellipsoid
cone synapse

Figure 3.3 Mislocalized cone mitochondria are found in Müller glia (MG) cells
PR, photoreceptor layer; IR, inner retina; OLM, outer limiting membrane.
(A) *In vivo* imaging of fish expressing *gnat2*:mtBFP and *GFAP*:GFP shows mislocalized mitochondria both inside (filled arrow) and outside (unfilled arrow) MGs. Both images were obtained from mtKR+, LED+ fish. Scale: 5 μm.
(B) 3D reconstruction of mislocalized mitochondrion encapsulated by an MG process from the first panel of (A). Scale: 3 μm.
(C) Quantification of mislocalized cone mitochondria classified by colocalization with MGs. Activation of mtKR increases both MG+ and MG− mislocalized mitochondria. $^{*}p < 0.05$ and $^{****}p < 0.0001$ using a two-way ANOVA. n = 6 noKR fish, n = 7 kR+ fish.
(D) Images from a 4 h, 5 min interval *in vivo* timelapse of a Tg(*gnat2*:mtBFP, *GFAP*:GFP,*gnat2*:mtKR) fish post-LED treatment. Scale: 5 μm.
(E) Longitudinal micrographs from SBFEM for mtKR− and mtKR+ fish (both LED treated). The mtKR fish contains several swollen, electron-lucent mitochondria between cone cell bodies near the photoreceptor nuclear layer and synapse. Scale: 5 μm.
(F) Transverse section from SBFEM stack of a mtKR+ fish at the OLM where abundant swollen/lucent mitochondria can be observed between cone cells in MG. Scale: 5 μm.
(G) 3D reconstruction of MG cytosol (green) and the swollen mitochondria (multicolor) observed both at the OLM further down MG processes.

Cone mitochondria in Müller cells are targets of mitophagy

We then used cone-specific expression of the lysosomal marker LAMP1-GFP (gnat2:LAMP1-GFP) to determine if autophagy machinery is recruited to mislocalized mitochondria in cones (Fig. 3.4A). While some mislocalized mitochondria colocalized with cone LAMP1 in both control and mtKR fish, ROS stress triggered a more robust increase in LAMP1 mislocalized mitochondria (Fig. 3.4B). Accordingly, a smaller fraction of mislocalized mitochondria were LAMP1+ in mtKR fish (Fig. 3.4C).

To investigate mitophagy further, we used an in vivo mitophagy marker: mt-SRAI (Katayama et al., 2020). mt-SRAI is a fluorescence resonance energy transfer (FRET) sensor with TOLLES and YPet. The ratio of TOLLES:YPet fluorescence is low in healthy mitochondria and high in acidified/degraded mitochondria. Using gnat2:mtSRAI fish, we did find mitochondria undergoing degradation within the PR layer and IR. (Fig. 3.4D). Activated mtKR fish had

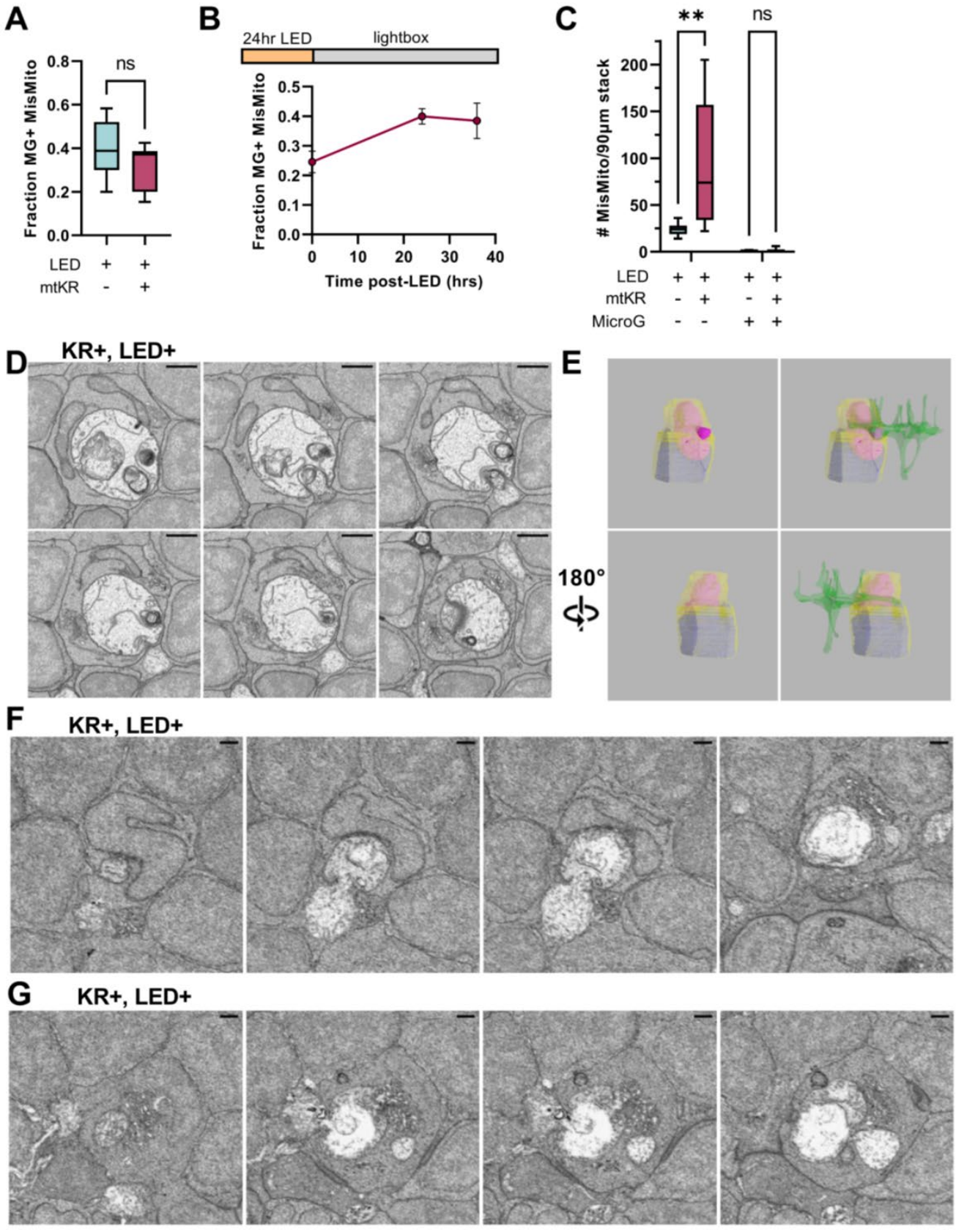
A
Fraction MG+ MisMito
0.8
0.6
0.4
0.2
0.0
ns
LED + +
mtKR - +
B
24hr LED
lightbox
Fraction MG+ MisMito
0.5
0.4
0.3
0.2
0.1
0.0
0 10 20 30 40
Time post-LED (hrs)
C
**
ns
MisMito/90µm stack
200
150
100
50
0
LED + + + +
mtKR - + - +
MicroG - - + +
D
KR+, LED+
E
180°
F
KR+, LED+
G
KR+, LED+

Supplemental Figure 3.2 Mislocalized mitochondria in glia and during extrusion from photoreceptors
A. No significant change in the fraction of mislocalized cone mitochondria in MG was observed upon mtKR activation. n=6 KR-LED+ fish, n=7 KR+LED+ fish. ns using Welch's t-test.
B. Fraction of mislocalized cone mitochondria in MG immediately after 24 LED activation and 24/36 hrs after LED cessation. Points =mean and bars = SEM. n=6 fish at time 0, n=8 fish at 24hr and 36hr.
C. Quantification of mislocalized cone mitochondria in microglia using Tg(*gnat2*:mtBFP, *mpeg1*:GFP) fish. Very few cone mitochondria are found in microglia with or without mtKR. n=7 fish each condition. **p<0.01 with 2-way ANOVA.
D. Transverse sections from SBFEM stack of a mtKR+ LED+ fish. Some material from a morphologically disturbed cone mitochondrion appears to be transferred into a neighboring Muller glial cell. Scale=1 μ m.both at the OLM further down MG processes.
E. 3D reconstruction of cone mitochondrion transfer event. Cone plasma membrane (yellow), cone mitochondria (magenta), cone nucleus (blue), and Muller glia (green).
F. Transverse sections from SBFEM stack of a mtKR+ LED+ fish depicting an additional example of a putative transfer event of cone mitochondria to a nearby Muller glial cell. Cone mitochondrion is in process of leaving cone cell. Scale=1 μ m.
G. Transverse sections from SBFEM stack of a mtKR+ LED+ fish depicting an additional example of a putative transfer event of cone mitochondria to a nearby Muller glial cell. Scale=1 μ m.

significantly more acidified mislocalized mitochondria than controls (Fig. 3.4E). A much higher fraction of mislocalized mitochondria were targeted for degradation than ellipsoid mitochondria in both control and mtKR fish, though an increase in the fraction of degraded mitochondria was noted in the ellipsoid of mtKR fish (Fig. S3.3A). Thus, cone mitochondrial stress increases mislocalization and degradation of mitochondria. This finding combined with the lack of robust cone-derived LAMP1 recruitment to mislocalized mitochondria suggests that cells other than cones may be responsible for disposing of cone mitochondria.

mtKR is not compatible with additional red fluorophore tags, so we used unstressed fish to assess the localization of cone mitochondria with gnat2:mtSRAI. Overall, mislocalized cone mitochondria outside of cone PRs (gnat2:TdTomato) were much more likely to be acidified than those inside cones, and they were often present in long trails consistent with radially oriented MGs (Fig. S3.3B,C). To verify this, we used gnat2:mtSRAI and GFAP:TdTomato fish. Trails of acidified cone mitochondrial remnants spanned the IR along MG processes (Fig. 3.4F).

Correlative light and electron microscopy further confirmed that the cone-derived mitochondrial

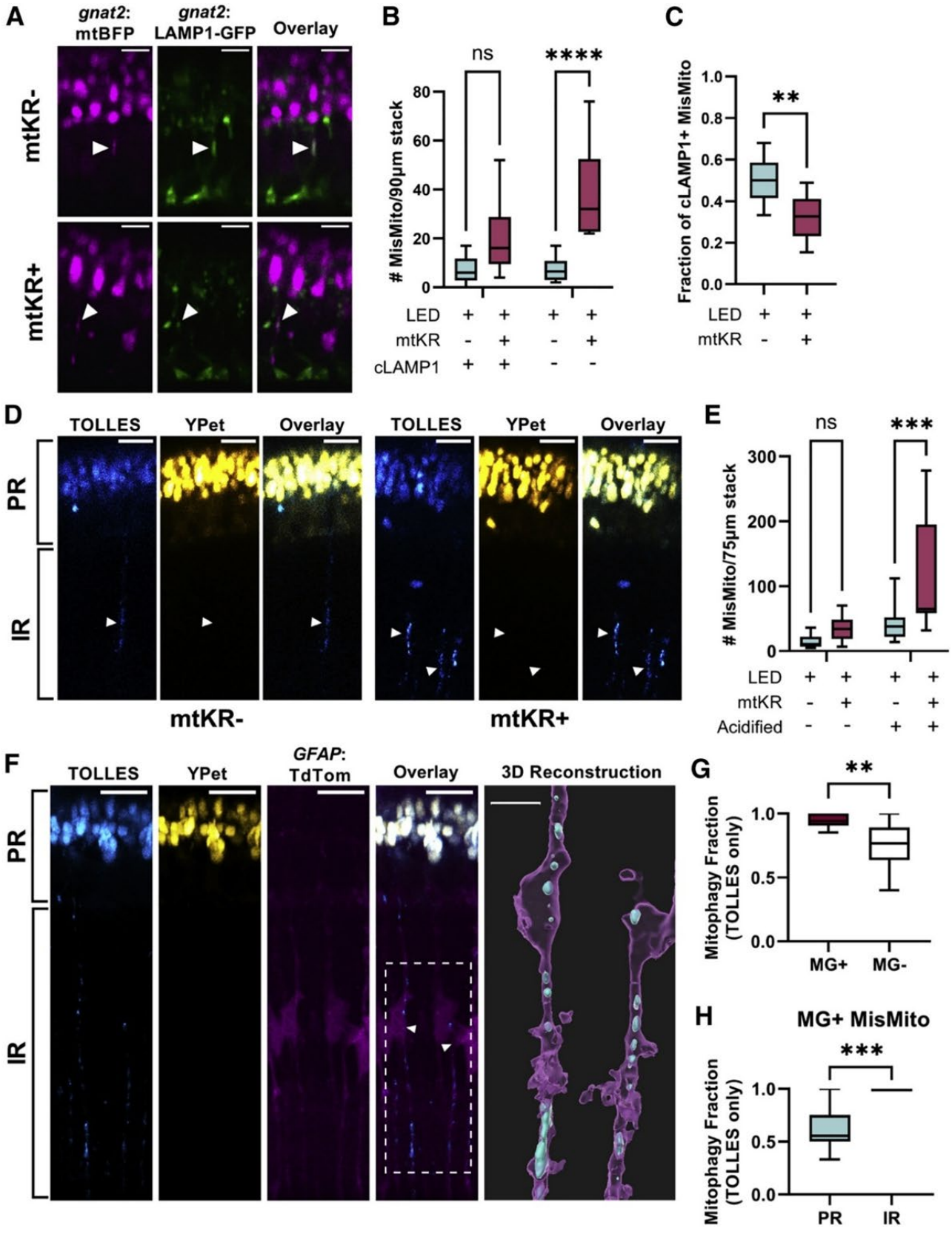

Figure 3.4 Cone mitochondria degradation occurs in MGs
(A) *In vivo* imaging of Tg(*gnat2*:mtBFP, *gnat2*:LAMP1-GFP) fish; mislocalized mitochondria colocalized with cone lysosomes (filled arrows) in mtKR− and mtKR+ fish. Scale: 5 μm.
(B) Quantification of (A) shows a marked increase in mislocalized mitochondria unassociated with cone lysosomes upon ROS stress. cLAMP1, cone LAMP1. n = ****p < 0.0001 using a two-way ANOVA. n = 10 fish each condition.
(C) Fraction of cLAMP1+ mislocalized mitochondria from data in (A) and (B). While mtKR have more mislocalized mitochondria, a lower fraction is associated with cone lysosomes compared with controls. n = 10 mtKR+ fish, n = 9 mtKR− fish (1 excluded from fraction due to <5 total mislocalized mitochondria). **p < 0.01 using Welch's t test.
(D) *In vivo* imaging of Tg(*gnat2*:mtSRAI) with and without mtKR (LED treated). PR, photoreceptor layer; IR, inner retina. Mitochondria that have lost YPet fluorescence (acid and protease sensitive) are in acidified compartments. Arrowheads indicate "trails" of acidified cone mitochondria in the IR. Scale: 10 μm.
(E) Quantification of acidified mislocalized mitochondria from dataset in (D). 3D volumes were generated in Imaris, manually binned as mislocalized/ellipsoidal, and identified as acidified if mean fluorescence TOLLES > Ypet. noKR n = 12; KR+ n = 9 fish. ***p < 0.001 with two-way ANOVA.
(F) *In vivo* imaging of normal, unstressed Tg(*gnat2*:mtSRAI, *GFAP*:TdTomato) fish (no mtKR, no LED). Trails of TOLLES+ mislocalized cone mitochondria colocalize with MG processes in the IR. Scale: 10 μm. Imaris was used to generate a 3D reconstruction (scale: 5 μm) of two of these MGs; their cell bodies are noted by an arrowhead and the ROI by a dotted line in the overlay fluorescent image (magenta: MG, cyan: TOLLES+ MisMito).
(G) Mitophagy fraction (acidified/total) of mislocalized mitochondria inside and outside MGs in unstressed fish. Mitochondria were manually binned by presence of YPet (see STAR Methods). n = 11 fish. **p < 0.01 with Welch's t test.
(H) Mitophagy fraction (acidified/total) of cone mitochondria in MG, binned by location in the retina. Mitochondria observed in inner retinal portions of MG were acidified. n = 11 fish. ***p < 0.001 with Welch's t test.

material in these long trails resided within cells in the center of the inner nuclear layer (Fig. S3.3F). Cone mitochondria in MGs were overwhelmingly acidified compared with their mislocalized counterparts not in MGs (Fig. 3.4G). Furthermore, of the cone mitochondria inside MGs, those in processes in the PR layer were far less likely to be acidified compared with those in the IR (Fig. 3.4H; 100% acidified in the IR of all fish). These results indicate that while mitophagy of mislocalized mitochondria can occur within cones, it is more extensive in MGs. As initial confirmation of this hypothesis, we detected MG-derived acidified and unacidified phagosomes using a fish with the tandem marker for autophagosomes, GFAP:GFP-mCh-LC3 fish (Fig. S3.3D,E). We found that after cold stress, a much greater fraction of the mislocalized

cone mitochondria in MGs were associated with acidified phagosomes than with unacidified phagosomes.

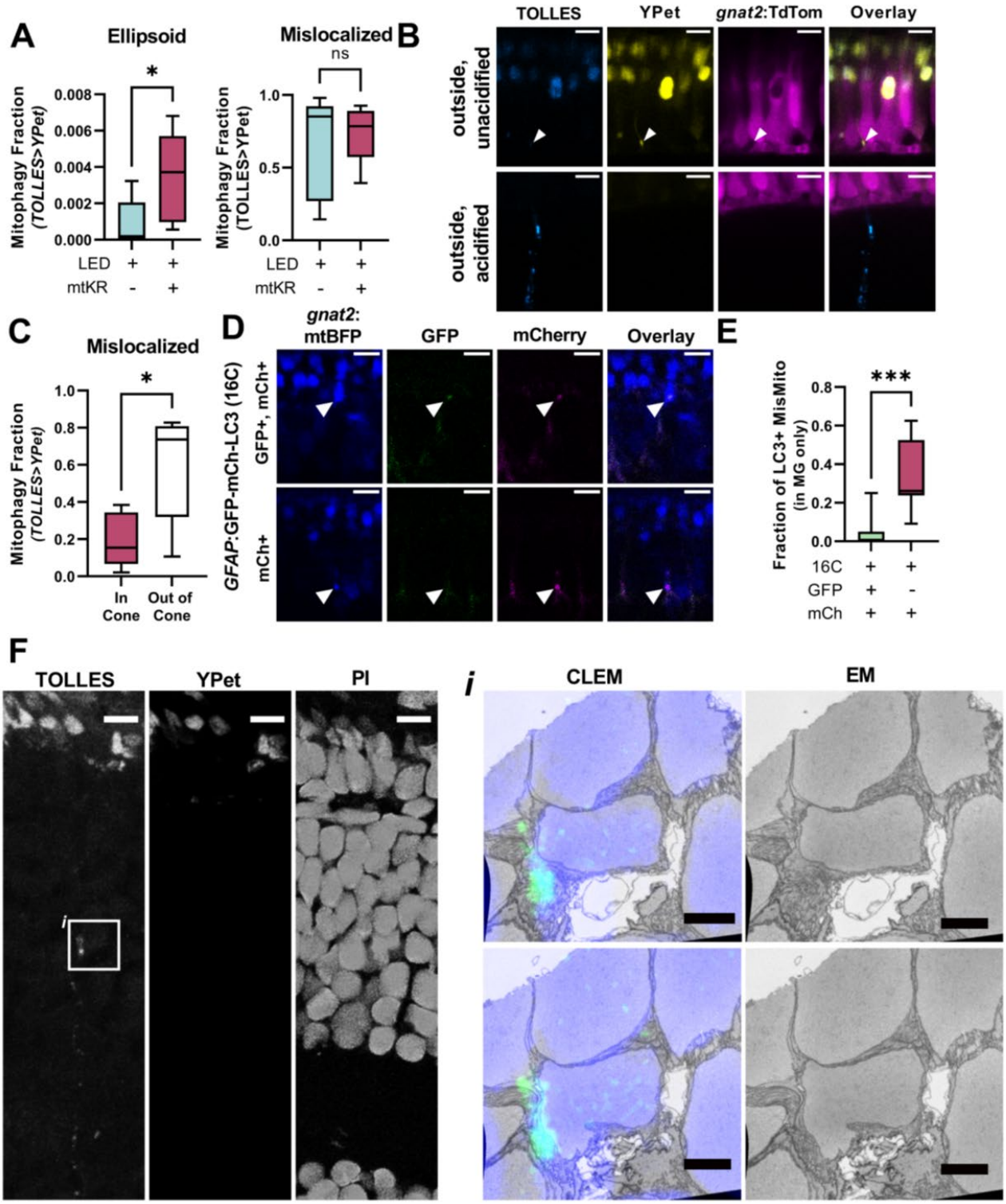

Supplemental Figure 3.3 Cone mitochondria are degraded in Müller glia
A. Mitophagy fraction (fraction of mitochondria with TOLLES>YPet, by volume) in ellipsoid and mislocalized mitochondria. Ellipsoid mitochondria have higher mitophagy in mtKR fish, but similar fractions are found in mislocalized mitochondria. Mitophagy is much higher in mislocalized mitochondria compared to ellipsoid mitochondria. n=11 KR-LED+ fish, n=9 KR+LED+ fish. *p<0.05 with Welch's t-test.
B. Confocal images from unstressed Tg(*gnat2*:mtSRAI, *gnat2*:TdTomato) fish, showing both acidified and unacidified cone mitochondria outside of cones. Scale=5 μ m
C. Mitophagy fraction (fraction of mitochondria with TOLLES>YPet, by counts) from data shown in B. A greater fraction of mitochondria outside of cones are acidified compared to those inside cones. n=5 fish. *p<0.05 using paired t-test.
D. Confocal images from cold-stressed Tg(*gnat2*:mtBFP, *GFAP*:GFP-mCh-LC3) fish showing colocalization of cone mitochondria and MG-derived phagosomes (arrows), both preacidification (GFP+,mCh+) and post-acidification (mCh+). Scale=5 μ m
E. Quantification of cone mitochondria in MG by association with either acidified or unacidified MG-derived phagosomes. Significantly more cone mitochondria are in acidified MG-derived phagosomes than unacidifed. n=10 fish. ***p<0.001 with paired t-test.
F. Correlative light and electron microscopy of cone mitochondria in the inner retina. The three left panels are confocal images showing acidified (TOLLES+ only) and unacidified (YPet+) cone mitochondria nuclei detected using propidium iodide (PI) . Scale=5 μ m. The slice imaged by confocal was processed for SBF-SEM and the inner retina region in *i* was aligned between the confocal and EM images. For the CLEM overlay in F*i*, acidified cone mitochondrial material is depicted in green and nuclei in blue. Scale=1 μ m

Discussion

The mtKR transgenic model

KR was a particularly useful tool that we used to examine the effects of oxidative stress on cone PR mitochondria. KR has been used to destroy cells selectively (Bulina et al., 2006; Yano et al., 2021), but it also has been used to study physiologic responses to oxidation (Korzh et al., 2011; Teh et al., 2010). We targeted KR specifically to cone PR mitochondria, and we constructed an optogenetic stimulus array for chronic activation of KR. Our EM analyses of these fish indicated that PRs appeared normal despite obvious morphological defects in cone mitochondria. Cristae were reduced, and mitochondria appeared large and translucent but not fragmented. We confirmed that LED-treated KR fish had elevated mitochondrial ROS compared with control fish, but this did not increase cone cell death. This model is a valuable tool for studying cone responses to elevated ROS beyond the larval stage examined here and in the

context of retinal diseases. Although we detected significant increases in mitochondrial stress with KR and LED compared with LED alone, one potential caveat that requires further investigation is how LED treatment could influence circadian activity. Shorter LED treatments than used in this study could alleviate this concern.

Transfer and degradation of mitochondria

A significant proportion of cone mitochondria not in PRs were in MGs. 3D reconstructions of confocal and SBF scanning EM images together with in vivo time-lapse imaging indicated that these mitochondria had been transferred to MGs. To dissect the fate of mislocalized mitochondria, we used transgenic strains with markers often used to assess stages of mitophagy: LAMP1, SRAI, and LC3 (Indira et al., 2018; Katayama et al., 2020; Samuvel et al., 2022). Acidification of mislocalized mitochondria, while occurring in cones, was especially pronounced outside of cones and in MGs. We also observed MG-derived LC3 accumulating on cone mitochondria that had been transferred to MGs. These results suggest that cone mitophagy operates near capacity and that, under stress, PRs dramatically increase the transfer of damaged mitochondria to MGs. This mechanism represents a significant process for PRs, since degradation occurred primarily outside of the ellipsoid region; in the ellipsoid, most mitochondria are unacidified (only 0.097% ± 0.035% acidified in control fish and 0.33% ± 0.082% acidified in mtKR+, by volume; see Figure S3.4A). These findings also align with previous work in mitoQC and mChGFP-LC3 mouse models showing enrichment of mitolysosomes and autophagosomes in the outer nuclear layer, away from the ellipsoid of PRs and where MG processes extend between PRs (McWilliams et al., 2019).

Transmitophagy was first observed in retinal neurons and astrocytes (Davis et al., 2014). Axonal protrusions filled with damaged mitochondria from retinal ganglion cells (RGCs) were surrounded by astrocytes near the optic nerve head (ONH). The evidence for transfer of damaged mitochondria to astrocytes was the presence of RGC-derived acidified mitochondria,

some of which were surrounded by Lamp1 inside of astrocytes at the ONH. These findings are similar to ours, although we require the development of more markers to fully compare the details of these two seemingly related processes. The use of astrocytes and not MGs reflects the specific association between astrocytes and RGC axons, whereas MGs ensheath the RGC cell body (Holländer et al., 1991). Neuron-astrocyte transmitophagy also occurs in Parkinson's and Alzheimer's disease (Lampinen et al., 2022; Morales et al., 2020). Release of mitochondria from cells can elicit an inflammatory response (Liu et al., 2021). The lack of stress-induced microglia activation in our study suggests that a direct connection, either vesicular or tubular, may facilitate transport of mitochondria from cones to MGs. Our EM data thus far also support vesicular transfer based on appearance of apparent budding from cones to MGs (Fig. S3.2D–G).

In other neuronal systems, not only has the transfer of damaged mitochondria for disposal and recycling been reported but the reverse mitochondrial transfer from glia back to neurons is associated with neuronal survival after injury both in vitro and in vivo (Hayakawa et al., 2016). Transfer of mitochondria isolated from macrophages was also found to reduce neuropathic and inflammatory pain mediated through CD200 receptor signaling within the peripheral nervous system (van der Vlist et al., 2022). In both studies, the purpose of the transfer is more than just to equilibrate ATP. Thus, transmitophagy represents a sub-topic within the broader field of mitochondrial transfer, and transfer of healthy mitochondria to rejuvenate cells is also important. Future studies in the mtKR model could assess whether any retinal glia supplement their mitochondria to cones.

Transmitophagy is a broadly used pathway not confined to the nervous system. For example, cardiomyocytes damaged by ischemia-reperfusion release large vesicles termed exophers that contain dysfunctional mitochondria. In the absence of macrophages that clear these damaged extruded mitochondria, resident cardiomyocyte mitochondria produce less ATP, which compromises cardiac function (Artuso et al., 2012). Similarly, when macrophages are

depleted and not available to clear oxidatively damaged mitochondria released by brown adipocytes, cold-induced thermogenesis is impaired (Rosina et al., 2022). These studies support the hypothesis that transmitophagy is protective and prevents intracellular accumulation of dysfunctional mitochondria.

PR specialization and outsourcing functions

PR neurons are optimized for light detection and signal transmission; they employ specialized biochemical mechanisms for vesicular transport both for the outer segments (Wensel et al., 2021), where phototransduction occurs, and for synaptic transmission (Thoreson, 2021). PRs use their cellular resources to maintain precise and robust responses to light by outsourcing cellular functions. For example, they are metabolically coupled with the retinal pigment epithelium both for nutrient cycling (Hurley, 2021) and for regeneration of 11-cis retinal after light exposure (Palczewski and Kiser, 2020). We propose that the transfer of damaged mitochondria is another outsourcing mechanism that helps PR survival by preserving resources and limiting damage to minimize disturbance to the essential functions of light detection and signaling.

Limitations of the study

Our findings stimulate many future exciting questions. We have not defined the signaling mechanism leading to specific removal of damaged mitochondria from the ellipsoid, the mechanisms of movement within the PR, how mitochondria are transferred to glia, or the details of the transcellular degradation process. Further, our strategies were optimal for experiments using larvae. Verifying our findings in adults needs to be a separate study. Understanding how PRs maintain healthy mitochondria may help to develop strategies to treat and prevent disease and broadly inform research in the relatively new field of intracellular mitochondrial transfer in biology.

STAR★Methods

Key resources table

REAGENT or RESOURCE	SOURCE	IDENTIFIER
Antibodies		
MTCO1	Abcam, ab14705	RRID:AB_2084810
SDHB	Abcam, ab14714	RRID:AB_301432
IRDye 680RD donkey anti-mouse IgG (H + L)	LI-COR Biosciences, 925–32212	RRID: AB_2716622)
FluoTag-X2 anti-TagFP Alexa Fluor 647	NanoTag Biotechnologies	N0502-AF647-L
Chemicals, peptides, and recombinant proteins		
Chloramphenicol	Thermo Scientific	Cat#AC227920250
dye CM-H_2DCFDA	Thermo Fischer	Cat#C6827
RNase A	New England Biolabs	Cat#T3018-2
iTaq™ Universal SYBR® Green Supermix	Bio-Rad	Cat#1725120
Critical commercial assays		
DNeasy Blood & Tissue kit	Qiagen	Cat#69504
Millipore ApopTag Fluorescein In Situ Apoptosis Detection Kit	EMD Millipore	Cat#S71100
Experimental models: Organisms/strains		

Tg(*gnat2*:*mtSRAI*)^{w268}	This study	N/A
Tg(*gnat2*:mtBFP)^{w269}	This study	N/A
Tg(*gnat2*:mtKillerRed)^{w270}	This study	N/A
Tg(*gnat2*:mtmKate2)^{w271}	This study	N/A
Tg(*gnat2*:LAMP1-GFP)^{w272}	This study	N/A
Tg(*GFAP*:GFP-mCh-LC3)^{w273}	This study	N/A
pde6c^{w59}	(Stearns et al., 2007)	http://zfin.org/ZDB-ALT-080206-1
Tg(*gnat2*:GFP)^{w206}	(Kennedy et al., 2007)	http://zfin.org/ZDB-ALT-181217-7
Tg(*GFAP*:TdTomato)	(Shin et al., 2014)	N/A
Tg(*gnat2*:TdTomato)	(Sloan et al., 2020)	N/A
Tg(*GFAP*:GFP)	(Bernardos and Raymond, 2006)	http://zfin.org/action/feature/view/ZDB-ALT-060623-4
Tg(*mpeg1*:GFP)gl22	(Ellett et al., 2011)	http://zfin.org/ZDB-ALT-120117-1
Tg(*TBP*-GAL4;*UAS*:secA5-YFP)	(Blume et al., 2020; van Ham et al., 2010)	N/A
Recombinant DNA		
Su9-EGFP	Addgene plasmid # 23214	RRID:Addgene_23214
mTagBFP	Addgene plasmid # 75175	RRID:Addgene_75175
mKate2	Addgene plasmid # 48345	RRID:Addgene_48345
SRAI	RIKEN DNA Bank	#RDB18223
KillerRed	(Bulina et al., 2006)	N/A

p5E-gfap	Addgene plasmid # 82401	RRID:Addgene_82401
LAMP1	(Drerup and Nechiporuk, 2016)	N/A
GFP-mCh-LC3	(George et al., 2016)	N/A
Software and algorithms		
Imaris 9.9	Oxford Instruments	RRID:SCR_007370
ImageJ	(Schindelin et al., 2012)	RRID:SCR_002285
Blender	www.blender.org	RRID:SCR_008606

Experimental model and subject details

Zebrafish

Experiments with zebrafish were authorized by the University of Washington Institutional Animal Care and Use Committee. All fish used in this study were maintained in the University of Washington South Lake Union aquatics facility at 27.5°C on a 14/10 h light/dark cycle. Fish used for confocal imaging and TUNEL staining were maintained in the $Roy^{-/-}$ genetic background, while fish used for western blotting, immunohistochemistry, qPCR, and electron microscopy were maintained in the AB or $Roy^{+/-}$ genetic background (iridophore pigmentation present). The *pde6c*^{w59} fish strain is described (Stearns et al., 2007). Animals used in this study were in the larval stages prior to sexual maturation.

Method details

Transgenic zebrafish generation

Six transgenic zebrafish lines were generated for this study: Tg(*gnat2*:mtmKate2), Tg(*gnat2*:mtBFP), Tg(*gnat2*:mtKillerRed), Tg(*gnat2*:LAMP1-GFP), Tg(*gnat2*:mtSRAI), and Tg(*GFAP*:GFP-mCh-LC3). Gateway-Tol2 assembly was used for generation of all constructs. For cone-specific expression, we used the zebrafish *gnat2* promoter cloned into a 5′ entry vector (Kennedy et al., 2007). All targeting of fluorophores to cone mitochondria was accomplished using the mitochondrial F0-ATPase targeting sequence cloned into a pME vector (cloned from Su9-EGFP, a gift from David Chan, Addgene plasmid # 23214; RRID:Addgene_23214). To generate the Tg(*gnat2*:mtBFP) line, we used a 3′ entry vector containing mTagBFP from Nicholas Cole (Addgene plasmid # 75175; http://n2t.net/addgene:75175; RRID:Addgene_75175) (Fowler et al., 2016). For the Tg(*gnat2*:mtmKate2) line, we used a 3′ entry vector containing mKate2 from Anna Planas & Tomas Santalucia (Addgene plasmid # 48345; http://n2t.net/addgene:48345; RRID:Addgene_48345) (Buj et al., 2013). For generation of Tg(*gnat2*:KillerRed), the KillerRed DNA was gifted to us by Pablo Peixoto; the original mitochondrial targeting sequence of the construct was not used and instead was replaced with the Su9 sequence (Bulina et al., 2006). The construct was cloned into a destination vector with a sBFP2 heart marker (a gift from Cecilia Moens) for aid in transgenic identification without activation of KillerRed. For generation of Tg(*gnat2*:mtSRAI), the SRAI sensor DNA was obtained from RIKEN DNA Bank (#RDB18223) and cloned into a 3′ entry vector; the original mitochondrial targeting sequence of the construct was not used and instead was replaced with the Su9 sequence (Katayama et al., 2020). We obtained the LAMP1 DNA from Alex V. Nechiporuk (Drerup and Nechiporuk, 2016). GFP-mCh-LC3 DNA was generated as previously described (George et al., 2016). The zebrafish GFAP promoter, p5E-gfap, was a gift from Judith Eisen (Addgene plasmid # 82401; http://n2t.net/addgene:82401; RRID:Addgene_82401) (Fowler et al., 2016). All constructs were injected into embryos at the 1-cell stage with Tol2 transposase mRNA. Larvae mosaic for the transgene were raised to adulthood to identify founder carriers. Single F0 founders were used to generate F1 fish that were screened for a

single insertion of the transgene; fish from the F2 generation and onward were used in this study.

The Tg(*gnat2*:GFP), Tg(*GFAP*:TdTomato) and Tg(*gnat2*:TdTomato) zebrafish lines are described (Kennedy et al., 2007; Shin et al., 2014; Sloan et al., 2020). Tg(*GFAP*:GFP) and Tg(*mpeg1*:GFP)gl22 fish lines are from the Zebrafish International Resource Center (from the Raymond and Leischke labs, respectively) (Bernardos and Raymond, 2006; Ellett et al., 2011). The Tg(*TBP*-GAL4;*UAS*:secA5-YFP) line was generated by Randy Peterson's lab and gifted to our facility by Diana Mitchell (Blume et al., 2020; van Ham et al., 2010).

Western blotting

Protein isolation and western blotting were performed using standard procedures (Bisbach et al., 2020b) with the following details. 6 larval bodies obtained at 6 dpf were pooled in each independent sample for protein isolation. 40 µg of protein from each of these pooled samples was loaded per well. For primary antibodies, MTCO1 (Abcam, ab14705, RRID:AB_2084810) and SDHB (Abcam, ab14714, RRID:AB_301432) were both used at a 1:1000 dilution. The secondary antibody IRDye 680RD donkey anti-mouse IgG (H + L) (LI-COR Biosciences, 925–32212, RRID: AB_2716622) was used at 1:5000 dilution.

DNA isolation and qPCR

Total DNA was isolated from pooled larval samples (10 larvae each, 6 dpf) using a DNeasy Blood & Tissue kit (Qiagen Cat#69504). An Applied Biosystems 7500 Fast Real-Time PCR System in conjunction with iTaq Universal SYBR Green Supermix (Bio-Rad, 1,725,120) was used for qPCR measurements according to the manufacturer's instructions. Relative quantification of mitochondrial DNA content was performed by normalizing CT values of mitochondrially-encoded NADH dehydrogenase 1 (*mt-ND1*) to nuclear-encoded DNA polymerase subunit gamma-1 (*polg1*) within each sample using previously characterized

primers (Artuso et al., 2012). Sample measurements were conducted in three technical replicates for each biological sample, and 5 biological replicates per condition were assayed.

Immunohistochemistry and TUNEL staining

Zebrafish larvae were collected at 6 dpf and fixed in 4% paraformaldehyde. Larvae were cryoprotected using sucrose gradients and embedded in OCT. 10µm sections were cut and warmed for 2 h. Sections were stained using a standard protocol (Hutto et al., 2020). (Antibodies: [1:1000] MTCO1 antibody (abcam 14,705) and [1:500] Tag-FP antibody (FluoTag-X2 anti-TagFP Alexa Fluor 647 N0502-AF647-L)).

TUNEL assay was performed using EMD Millipore ApopTag Fluorescein In Situ Apoptosis Detection Kit (S71100) with the following modifications: hydrated sections with IHC PBS (pH 7.4) for 5 min, permeabilized with 20 µg/mL Proteinase K for 5 min, 5 min IHC PBS (pH 7.4) wash, 5 min incubation with equilibration buffer, 2 h TdT enzyme solution incubation, 2 washes with Stop/Wash buffer followed by IHC PBS (pH 7.4) wash, and 1 h Anti-Digoxigenin Conjugate incubation. Nuclei were stained using Hoechst 33,342, trihydrochloride trihydrate (10 µM; Life Technologies, H3570). Images collected on Leica SP8 (RRID: SCR_018169).

Stress treatments

For chloramphenicol treatments (CAP, Thermo Scientific, Cat#AC227920250), larvae were incubated in either 500 µM or 1.2mM CAP from 3 dpf to 6dpf with ethanol vehicle (0.1% v/v), using previously reported effective concentrations as a ref (Byrnes et al., 2018). Media was refreshed with treatment each day. For cold stress treatments, zebrafish were placed in a covered benchtop incubator set to 16°C (Benchmark Scientific, Cat# H2200-HC) fitted with a 4100K lightbulb for a 14/10 h light/dark cycle. Fish were kept in the incubator starting at 4 dpf (48 h treatment) or 5 dpf (24 h treatment). Confocal imaging was conducted at ambient temperature.

For cone-specific ROS generation in Tg(gnat2:mtKillerRed) fish, embryos were kept in a chamber outfitted with a UV-blue bandpass optical filter (Newport, Cat# FSR-BG3) to ensure fish were kept on the standard light/dark cycle but KillerRed would not be activated. At 4dpf, fish were sorted using blue heart fluorescence to identify Tg(gnat2:mtKillerRed) fish and either kept in the chamber or set up on the stimulating LED array. For stimulation of KillerRed, we constructed the optogenetic stimulus array with 565nm LED Stars (LED Supply, CREEXPE2-COL-X, PC Amber), an aluminum heatsink (Uxcell,a14111400ux0256), an LED driver (LED Supply, 0A011-D-V-xxx), and a power supply (Meanwell, LRS-200-24). LEDs were attached to the heatsink using heat-resistant glue in an array to fit under the 12 wells of a 48-well plate. The heatsink was fitted with 3D-printed housing to suspend the plate over the array. Two small fans were placed on opposite sides of the heat sink to disperse warm air. A mechanical outlet timer was used to set the intervals of LED stimulation (15 min on, 15 min off). Fresh media was replaced every 24 h and fish were collected for analysis at 6 dpf.

ROS measurements

ROS were detected using the dye CM-H_2DCFDA (Thermo Fischer, Cat#C6827). Larval eyes were enucleated at 6 dpf and incubated in an oxygenated, supplemented Ringer's media previously described that optimizes retinal tissue viability *ex vivo* (Giarmarco et al., 2018). Eyes from each experimental group were pooled and incubated in the same media containing 50 µM CM-H_2DCFDA for 30 min while covered on a gentle rocker. For H_2O_2 positive controls, this incubation media was supplemented with 10 mM H_2O_2. After incubation, eyes were washed three times with supplemented Ringer's media and embedded with the lens facing downward in 0.5% low melting point agarose for confocal imaging. Embedded eyes were covered with the supplemented Ringer's media throughout imaging.

Transmission and serial block-face scanning electron microscopy

Zebrafish larvae were fixed and embedded in blocks of resin at 6 dpf for TEM or SBEM imaging (Hutto et al., 2020). Samples were imaged using a JEOL JEM-1230 transmission electron microscope or Zeiss Sigma VP scanning electron microscope. The step size for the SEM was 50nm and the thin sections imaged on the TEM were 80 nm. Z-stacks containing Müller glia and mitochondria were aligned and manually traced using the TrakEM2 plugin in ImageJ (RRID:SCR_008954) (Cardona et al., 2012) (for using TrakEM2 in general) (Saalfeld et al., 2012, 2010); (for aligning). 3-D reconstructions and animations were created using Blender (RRID:SCR_008606).

Confocal imaging of live larvae

For confocal imaging experiments, larvae were maintained in embryo media containing 0.003% 1-phenyl 2-thiourea (PTU, Sigma-Aldrich P7629) starting at 24 h post-fertilization. At 6dpf zebrafish larvae were anesthetized using 0.02% (w/v) Tricaine then transferred to 0.5% low melting point agarose containing embryo media with 0.003% PTU and 0.02% (w/v) Tricaine (Sigma-Aldrich, E10521). Larvae were positioned in agarose in a Petri dish mounted to a slide, then covered with embryo media and 0.02% (w/v) tricaine to prevent drying out. Imaging was performed with a Leica SP8 (RRID: SCR_018169). For all experiments other than Fig. 3.4F, detectors were set to standard mode for quantitative imaging. For Fig. 3.4F, due to the dim fluorescence of both SRAI in the inner retina and Tg(*GFAP*:TdTom) at the 6 dpf stage, detectors were changed to BrightR collection for a larger dynamic range. For all experiments, eye volume and the fluorophore intensity determined how much useful imaging depth was available, which was identical in controls for that experiment.

Image analysis and processing

All analyses of confocal images were conducted on images that were not processed with Leica's Lightning algorithm. Lightning processing for presentation of images was only used for

the dim signals in Fig. 3.4F. Image analysis was conducted using ImageJ + Fiji software (SCR_002285) and researchers were blinded to sample identity using the “Blind Analysis Tools” plugin developed by Astha Jaiswal and Holger Lorenz (Schindelin et al., 2012). When identifying mislocalized mitochondria, researchers were blinded to other image channels. Colocalization analyses of mislocalized mitochondria were performed qualitatively on blinded samples after mitochondria identification and subsequent unblinding of the additional channels. For co-localization with microglia, mislocalized cone mitochondria were identified blinded to sample identity and blinded to other fluorescence channels, then mitochondria were assessed for colocalization with microglia while remaining blinded to sample identity. Imaris 9.9 (RRID:SCR_007370) was used for 3D surface reconstructions of fluorescence confocal data. For SRAI quantification, which required comparing the mean fluorescence of TOLLES and YPet for objects in 3D space, Imaris 9.9 was used to generate 3D surfaces of mitochondria in an image with the same surface algorithm applied to all samples. The total mitochondrial surface was divided into ellipsoid and mislocalized mitochondria manually by using the 3D reconstruction in tandem with a 3D slicer of original images for reference. Mitochondrial volumes with a mean fluorescence signal in the TOLLES channel higher than the YPet channel were designated as acidified. For the SRAI experiment in Fig. 3.4F, imaging in BrightR mode prevented quantification of the channels in this manner and instead mitochondria were binned as positive or negative for YPet fluorescence.

Correlative light and electron microscopy (CLEM)

Zebrafish larvae expressing both Tg(*gnat2*:mtKillerRed) and Tg(*gnat2*:mtSRAI) were treated with PTU, raised on the LED array described above starting at 4dpf, and collected at 6 dpf. Whole larvae were incubated 30 min at room temperature (RT) on a rotator in fixative (2% glutaraldehyde and 4% paraformaldehyde in 0.1 M sodium cacodylate buffer), and washed with PBS. Following 2 h cryoprotection in 30% sucrose, larvae were embedded in OCT and frozen at

−20°C. 60 µm cryosections were collected into PBS, washed with 2X saline sodium citrate (SSC) buffer, then incubated with RNase A (1:200 in 2X SSC; New England Biolabs, T3018-2) for 20 min at 37°C. Sections were washed 3 times in excess 2X SSC, then counterstained with propidium iodide (PI; 1 µg/mL; Life Technologies, P3566) for 5 min at RT.

For fluorescence imaging, individual sections were sandwiched between a slide and coverslip in a drop of 500 ng/mL PI in 2X SSC. TOLLES, YPet, and PI image stacks were collected with a Leica SP8 confocal using a 63X oil objective; XY resolution was 90 nm/pixel and Z resolution was 300 nm. After confocal imaging, sections were released into PBS and processed as described for SBEM imaging (Giarmarco et al., 2020). SBEM images were collected using a VolumeScope SEM (Apreo, Thermo Fisher Scientific) at a voxel size of 8 × 8 × 50 nm (Morales et al., 2020). Alignment of confocal and SBEM stacks was performed in ImageJ with the BigWarp plugin (Bogovic et al., 2016) using nuclei to assign landmarks.

Quantification and statistical analysis

Statistics

Numerical results in text are reported as mean ± standard error of the mean unless otherwise stated. Statistical tests were performed using Graphpad Prism v 9.4 software. For statistical analysis, replicates (*n*) were always defined as biological replicates, not technical replicates.

Information on what constitutes *n* (e.g., fish, mitochondria, cells) is listed in the figure legend of each experiment. For all box-and-whisker plots, the whiskers show the minimum and maximum values while the box boundaries represent the 25th and the 75th quartile with a line at the median. For one-way ANOVA tests, Tukey's multiple comparisons test was used. For two-way ANOVA tests, Šídák's multiple comparisons test was used.

Acknowledgements

We thank Stanley Kim for managing our fish facility and Sharm Knecht for assisting with the SBF scanning EM (SBFSEM) required for the correlative light and electron microscopy (CLEM) analysis. Funding for this project was provided by P30EY001730 (UW Vision Core; Neitz), R01EY026020 (S.E.B.), F31EY033983 (K.M.R.), and T32EY007031 (R.A.H.). The graphical abstract was created with BioRender.com.

Author contributions

R.A.H. performed the major role in the original conceptualization of this project. R.A.H., M.M.G., and K.M.R. designed, performed, and interpreted experiments. S.E.B. helped design and interpret experiments. S.E.B. wrote the paper. R.A.H. and K.M.R. edited the paper, and all authors reviewed the final text. E.D.P. and Z.S.C. performed experiments.

Chapter 4 – Retinopathy-associated inosine monophosphate dehydrogenase 1 mutations cause metabolic and filament defects in cones

This work is currently under review.

The other contributing authors are M.M. Giarmarco, V. Truong, Y. Wang, M. Eminhizer, Y. Xiang, W.M. Cleghorn, G. Sanchez, A.L. Burrell, J.M. Kollman, J. Du, and S.E. Brockerhoff

Introduction

Autosomal dominant retinitis pigmentosa (ad-RP) and Leber congenital amaurosis (LCA) are photoreceptor degenerative diseases that lead to blindness. Mutations in several proteins, including inosine monophosphate dehydrogenase I (IMPDH1), a key enzyme in the de novo purine biosynthesis pathway (Burrell and Kollman, 2022; Sakti et al., 2023) cause these diseases. IMPDH1 is abundant in both rod and cone photoreceptors (Cleghorn et al., 2022; Karlsson et al., 2021; Plana-Bonamaisó et al., 2020) and unlike the typical ad-RP phenotype where rods die first and cones secondarily die, patients with IMPDH1 mutations often have an early cone defect (Bennett et al., 2020; Sakti et al., 2023; Wada et al., 2005; Wendel et al., 2024).

IMPDH1 sits at a branch point between adenine and guanine synthesis where it converts inosine monophosphate (IMP) into xanthine monophosphate (XMP) reducing NAD+ to NADH. IMPDH1 forms octamers that can stack to form filament structures in cells. It can be allosterically regulated by downstream products, ATP and GTP (Buey et al., 2015; Fernández-Justel et al., 2019a, 2019b). These filaments can interact with other metabolic proteins involved in purine or pyrimidine metabolism for further regulation (Pedley and Benkovic, 2017). The retina has a specific IMPDH1 isoform that is less sensitive to GTP inhibition (Burrell et al., 2022). Zebrafish photoreceptors predominantly express a specific impdh1a transcript (tvX1) (Cleghorn et al., 2022). This variant has similar structural and functional characteristics as human retinal IMPDH1 (Cleghorn et al., 2022).

Purine metabolism is essential for nucleotide production which is necessary for DNA and RNA synthesis, energy currency including ATP and GTP, and production of signaling molecules, such as cGMP. Photoreceptor energy demand is uniquely high – a mouse rod photoreceptor is reported to consume 10^8 ATP per second, which is used to maintain the membrane potential (Okawa et al., 2008). Photoreceptor outer segment membranes are packed with proteins required for phototransduction. Rhodopsin, a protein responsible for initial light detection, has

approximately 60,000,000 molecules per mouse outer segment (Skiba et al., 2023). 10% of mouse rod outer segments are renewed daily (Umapathy et al., 2023; Young, 1967). cGMP is essential for phototransduction in photoreceptors. Phosphodiesterase 6 (PDE6) is an enzyme in photoreceptors that hydrolyzes cGMP to GMP in the light which allows cyclic nucleotide gated (CNG) channels to close (Arshavsky et al., 2002). PDE6 mutations can increase cGMP levels leading to photoreceptor death (Farber and Lolley, 1974; Power et al., 2020). Photoreceptor degeneration stemming from a nonsense mutation in the Pde6b gene can be delayed by treating mice with an IMPDH inhibitor (Yang et al., 2020).

The mechanism behind IMPDH1 related degeneration is unknown. Knocking out Impdh1 has no impact on zebrafish photoreceptor structure and mice have a mild retinopathy (Aherne et al., 2004; Cleghorn et al., 2022). This suggests that mutations in IMPDH1 that cause degeneration cause a gain of function. Further, several mutations are clustered near ATP and GTP binding sites (Burrell et al., 2022; Sakti et al., 2023), and a subset of these (termed class 1) mutations disrupt the inhibitory allosteric regulation of the protein by GTP (Burrell et al., 2022; Burrell and Kollman, 2022). One hypothesis is that, in vivo, hyperactive IMPDH1 could cause elevated levels of downstream guanine nucleotides, including cGMP, which would promote cell death. However, evaluating IMPDH1-associated photoreceptor cell death has not been possible due to the lack of IMPDH1 mutant animal models.

Here we present the first IMPDH1 mutant disease models with zebrafish expressing the class 1 D226N or K238E mutation specifically in cone photoreceptors. We focused our studies testing if IMPDH1 mutations near the ATP and GTP binding spots led to hyperactivity and elevated cGMP in vivo. We evaluated steady state purine and pyrimidine metabolism and metabolic flux of glucose through glycolysis and the pentose phosphate pathway (PPP). Finally, we evaluated Impdh1 filament size and localization to look for protein aggregation. Our results indicate that a hyperactive version of Impdh1 leading to elevated cGMP is likely not the cause of photoreceptor death in our models. Other changes in metabolism, Impdh1 protein

polymerization and localization, provide new clues regarding the cause of cell death. The availability of the animal models we generated in this study will allow further evaluation of these new hypotheses.

Results

Zebrafish models with Impdh1 class I mutations show hyperactivity *in vitro*

We generated two zebrafish models each with a different class I Impdh1 mutation, K238E and D226N (Fig. 4.1A). Mutated versions of the retinal form of the zebrafish *impdh1a* cDNA were targeted to cone photoreceptors using the cone transducin promotor, *gnat2* (Kennedy et al., 2007; Fig. 4.1B and Methods). We also generated a transgenic wild type (*Tg* WT) *impdh1a* line to test if increased *impdh1a* expression impacted our results (Fig. 4.1B). All transgenes contained a *myc* tag at the C-terminus to differentiate between endogenous and transgenically expressed protein (Fig. 4.1B). Western blots of larval eyes from the stable

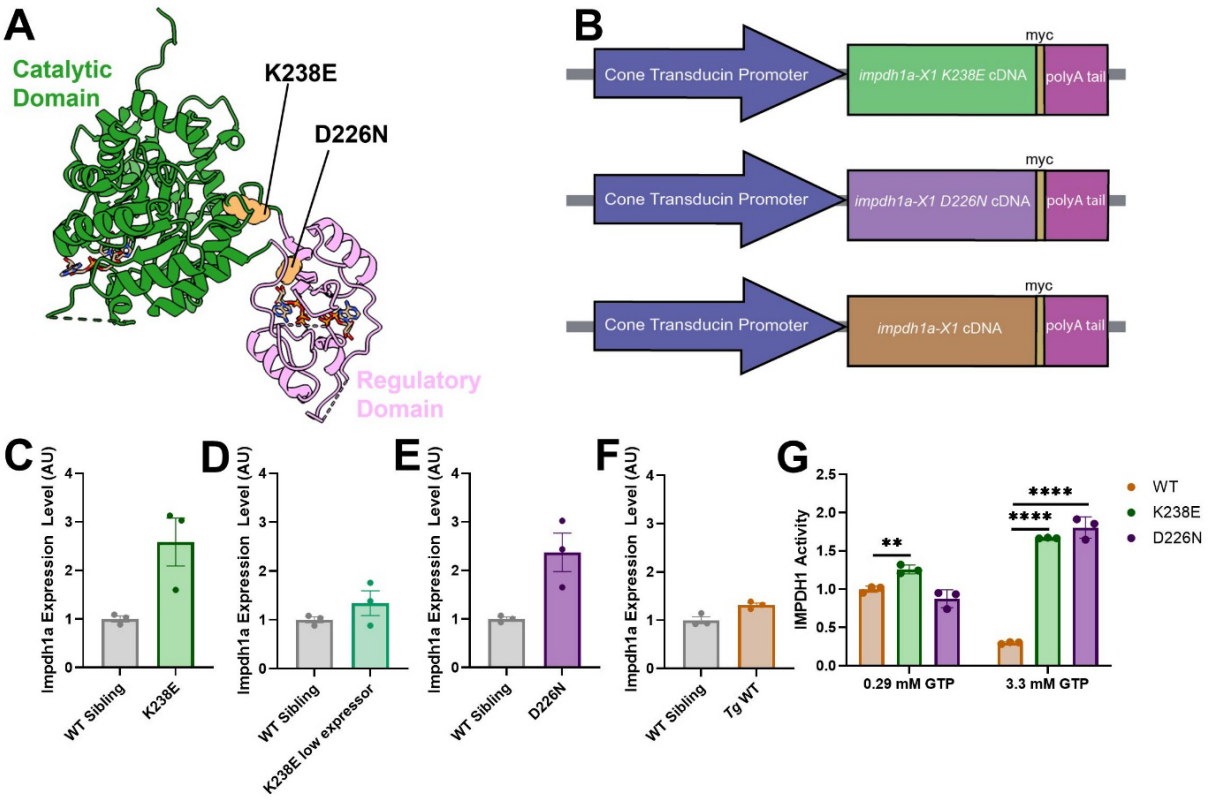

Figure 4.1: Zebrafish *impdh1* transgenic line generation.
A. Two disease associated Impdh1 mutations (orange) on Impdh1 monomer that were stably expressed in zebrafish.
B. Schematic describing transgenic zebrafish lines. All lines are under a cone transducing promoter, have a myc tag and a polyA tail. Either Impdh1 mutations (K238E or D226N) or WT *impdh1a* cDNA were injected.
C. *impdh1* expression level from 7dpf zebrafish larval eyes expressing K238E *impdh1* mutation or WT siblings. n = 3 for K238E and WT siblings. Error bars are s.e.m.
D. *impdh1* expression level from 7dpf zebrafish larval eyes expressing K238E *impdh1* mutation or WT siblings. n = 3 for K238E and WT siblings. Error bars are s.e.m.
E. *impdh1* expression level from 7dpf zebrafish larval eyes expressing D226N *impdh1* mutation or WT siblings. n = 3 for D226N and WT siblings. Error bars are s.e.m.
F. *impdh1* expression level from 7dpf zebrafish larval eyes expressing WT *impdh1* or WT siblings. n = 3 for WT *impdh1* and WT siblings. Error bars are s.e.m.
G. Purified Impdh1 protein activity assay. Both K238E and D226N are not inhibited by high concentrations of GTP. n = 3 for WT, K238E, and D226N. **** = p≤0.00005 ** = p≤0.005 as determined by unpaired t test. Error bars are s.d.

transgenic strains indicated that expression levels ranged from 0.88 – 3.1x (Fig. 4.1C-F, Fig. S1A-D) compared to endogenous Impdh1a. Enzyme assays using purified wild type (WT) and mutated zebrafish Impdh1a protein showed that both mutations eliminated the negative allosteric regulation of the protein by GTP, similar to the results observed using human IMPDH1 (Fig. 4.1G) (Burrell et al., 2022).

In humans, the IMPDH1 mutations K238E and D226N cause photoreceptor degeneration (For review, see Sakti et al., 2023). To evaluate if cones degenerate in our

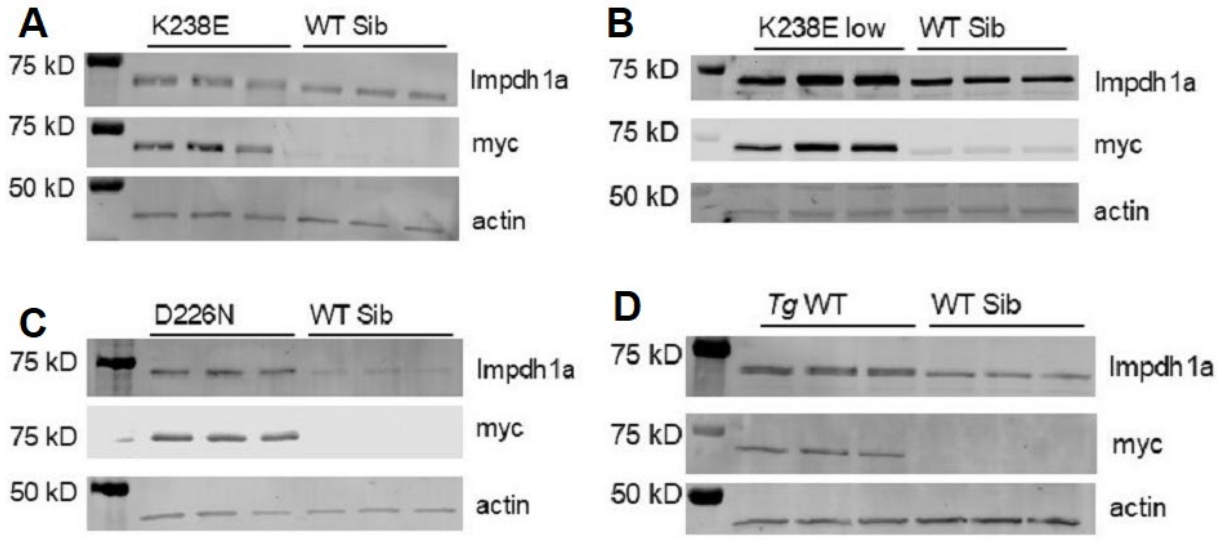

Supplemental Figure 4.1: Expression levels of *impdh1* transgenic lines range from 0.88 – 3.1x.
A. Western blot probed with custom Impdh1 antibody, myc antibody, and beta actin (loading control). K238E transgenic larvae are in lanes 2-4 and WT siblings are in lanes 5-7 (all 7 dpf).
B. Western blot probed with custom Impdh1 antibody, myc antibody, and beta actin (loading control). K238E transgenic larvae are in lanes 2-4 and WT siblings are in lanes 5-7 (all 7 dpf).
C. Western blot probed with custom Impdh1 antibody, myc antibody, and beta actin (loading control). D226N transgenic larvae are in lanes 2-4 and WT siblings are in lanes 5-7 (all 7 dpf).
D. Western blot probed with custom Impdh1 antibody, myc antibody, and beta actin (loading control). WT Impdh1 transgenic larvae are in lanes 2-4 and WT siblings are in lanes 5-7 (all 7 dpf).

transgenic models, we crossed our strains with a previously established line expressing eGFP in the cone cytosol (*Tg*(*gnat2:eGFP*); Kennedy et al., 2007). At one month of age, zebrafish with the K238E Impdh1 mutation, showed no signs of cone loss (Fig. 4.2A,B). K238E mutant zebrafish showed signs of degeneration starting at 2 months and had significant degeneration at 4 months (Fig. S4.2A-D). Some residual cones were present up to one year of age (Fig. 4.2C,D). To verify that cone degeneration was not due to expression levels of the transgene, we evaluated cone loss in another zebrafish line with the K238E mutation expressed at only 1.3x WT levels (Fig. 4.1D, Fig. S4.2E,F). This strain also showed significant cone degeneration by 4.5 months (Fig. S4.2E,F). In contrast, cones in zebrafish expressing *impdh1a* containing the D226N mutation did not have significant cone loss by 2 years old (Fig. 4.2E,F, Fig. S4.2G,H). Transgenic WT *impdh1a* zebrafish showed no signs of degeneration at all timepoints tested (Fig. 4.2B,D,F Fig. S4.2A-D, G-I). Prior to any degeneration, all transgenic *impdh1a* zebrafish models were sighted and had normal forward and reverse OKR responses (Fig. 4.2G, Fig. S4.2J-L).

Glucose usage remains unchanged with D226N mutant, but cellular redox status is perturbed

We hypothesized that if Impdh1a were hyperactive, we would detect additional guanine

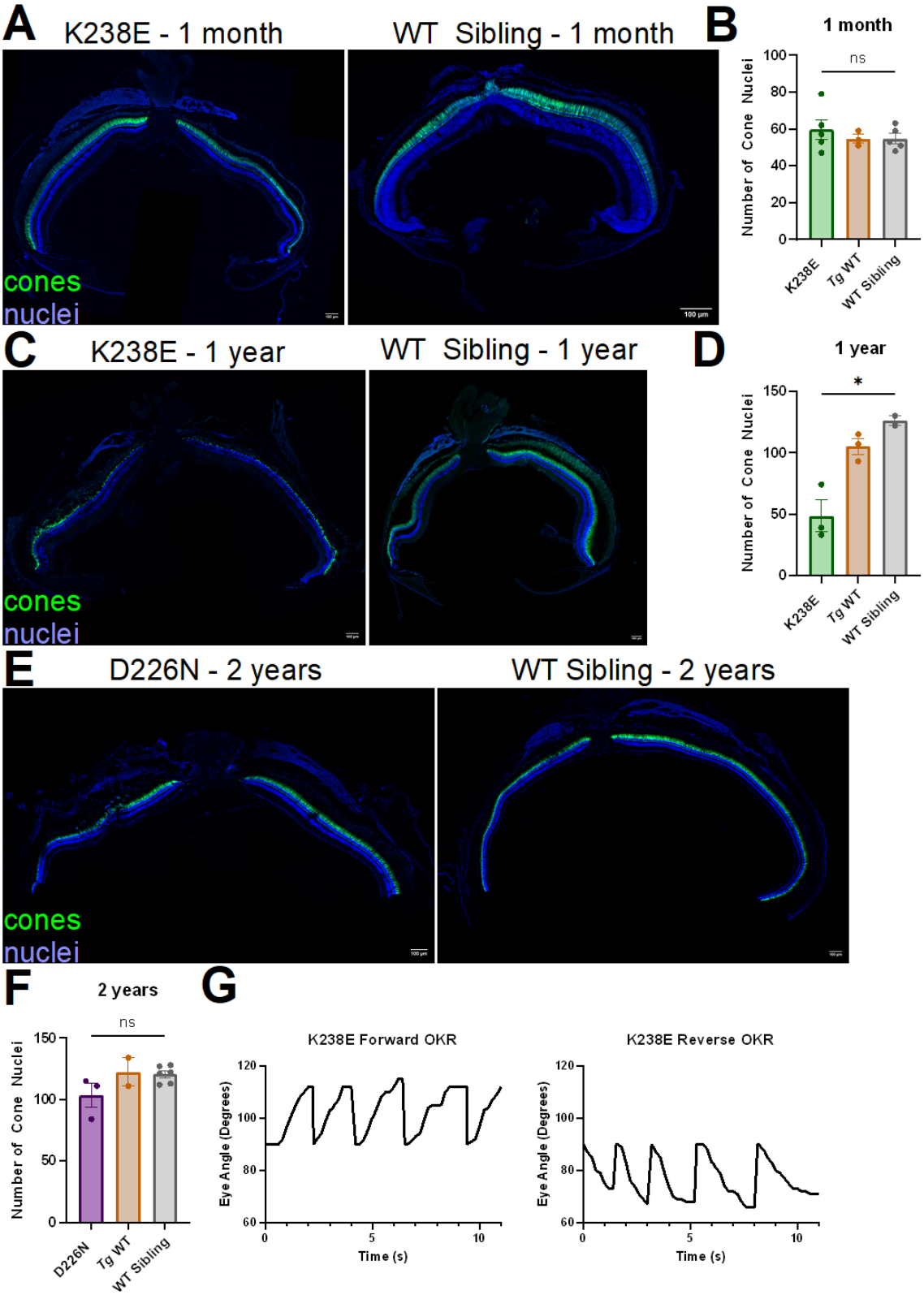

Figure 4.2: K238E has severe cone degeneration by 1 year whereas D226N does not show significant signs of cone degeneration by 2 years.
A. 1 month old zebrafish with K238E mutation (left) show no signs of degeneration as compared to wild type sibling (right). Cone cytosol is in green (*gnat2:EGFP* with GFP antibody) and nuclei are in blue. Scale bar = 100μm.
B. Cone nuclei were counted across 1/3 of the dorsal side of the retina. There was no significant change in cone nuclei for K238E compared with WT sibling at 1 month. n = 5 for K238E and WT siblings, n = 3 for *Tg* WT. ns = not significant as determined by unpaired t test. Error bars are s.e.m.
C. K238E has significant cone loss by 1 year of age (left) as compared to wild type sibling (right). Cone cytosol is in green (*gnat2:EGFP* with GFP antibody) and nuclei are in blue. Scale bar = 100μm.
D. Cone nuclei count of zebrafish expressing K238E IMPDH1 mutation or wild type sibling. There was significantly less cone nuclei in zebrafish expressing K238E *impdh1* mutation as compared to wild type sibling. n = 3 for K238E and *Tg* WT, n = 2 for WT sibling. * = p≤0.05 as determined by unpaired t test. Error bars are s.e.m.
E. 2 year old zebrafish with D226N mutation (left) show no signs of degeneration as compared to wild type sibling (right). Cone cytosol is in green (*gnat2:EGFP* with GFP antibody) and nuclei are in blue. Scale bar = 100μm.
F. Cone nuclei were counted across 1/3 of the dorsal side of the retina. There was no significant change in cone nuclei for D226N compared with WT sibling at 2 years. n = 3 for D226N, n = 2 for *Tg* WT, and n = 6 for WT sibling. ns = not significant as determined by unpaired t test. Error bars are s.e.m.
G. Zebrafish larvae containing K238E *impdh1* mutation OKR trace. Zebrafish larvae have forward (right) and reverse (left) OKR response at 5dpf.

nucleotides. This could require increased shunting of glucose-6-phosphate into the PPP leading to the synthesis of more ribose-5-phosphate. To evaluate this, we measured flux through the PPP in isolated retinas incubated in 1,2 ^{13}C glucose. When 1,2 ^{13}C glucose goes through glycolysis, both heavy labels remain in the end products of glycolysis, whereas if 1,2 ^{13}C glucose is shunted to the PPP, only one heavy labeled carbon remains (Fig. 4.3A). There was no difference in the rate of production of ^{13}C-3PG for the D226N mutant or Tg WT as compared to non-transgenic siblings (Fig. 4.3B). We also did not detect a difference in the steady state amount of m+1 3PG (PPP derived) between D226N mutants or *Tg* WT compared to WT siblings amount of m+1 3PG (PPP derived) between D226N mutants or *Tg* WT compared to WT siblings (Fig. 4.3C). These results indicate that the amount of glucose being shunted to the PPP remains unchanged.

To convert IMP to XMP, IMPDH1 reduces NAD^+ to NADH. Another prediction, if Impdh1 were hyperactive, is that NADH to NAD^+ ratio would increase. Measuring the lactate to pyruvate ratio is a way to assess the cellular NADH to NAD^+ ratio (Williamson et al., 1967). The

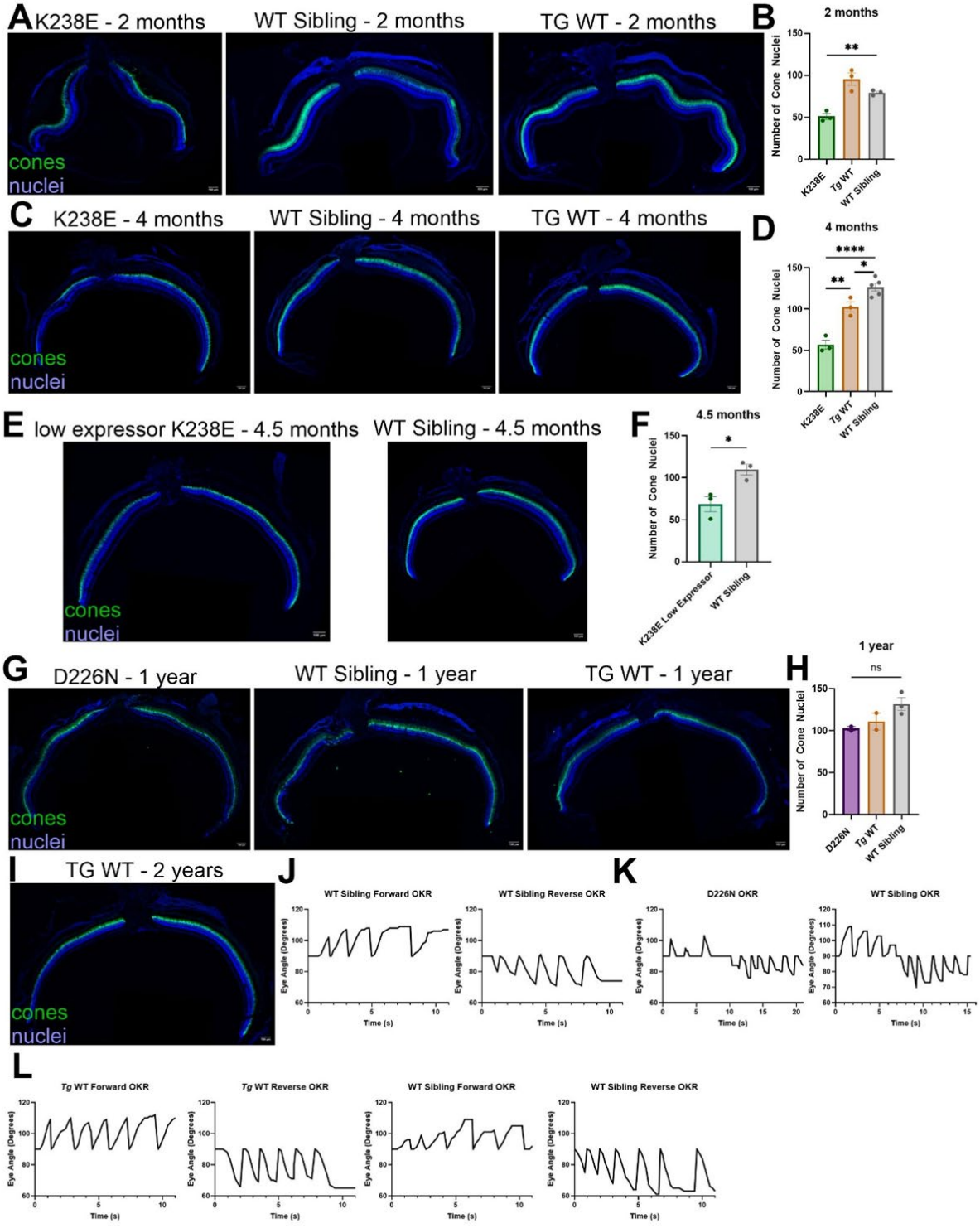

Supplemental Figure 4.2: K238E mutants have early signs of degeneration and D226N have no signs of cone loss at one year and normal larval visual function.
A. K238E has significant cone loss at 2 months old (left) as compared to wild type sibling (center). TG WT (left) shows no sign of cone loss. Cone cytosol is in green (*gnat2:EGFP* with GFP antibody) and nuclei are in blue. Scale bar = 100μm.
B. Cone nuclei were counted across 1/3 of the dorsal side of the retina. There was significant cone loss for K238E compared with WT sibling at 2 months, but not with *Tg* WT. n = 3 for all groups. ** = p≤0.005 as determined by unpaired t test. Error bars are s.e.m.
C. K238E has significant cone loss at 4 months old (left) as compared to wild type sibling (center). TG WT (left) shows no sign of cone loss. Cone cytosol is in green (*gnat2:EGFP* with GFP antibody) and nuclei are in blue. Scale bar = 100μm.
D. Cone nuclei were counted across 1/3 of the dorsal side of the retina. There was significant cone loss for K238E compared with WT sibling and *Tg* WT at 4 months. n = 3 for K238E and *Tg* WT and n = 5 for WT sibling. * = p≤0.05 ** = p≤0.005 **** = p≤0.00005 as determined by unpaired t test. Error bars are s.e.m.
E. Zebrafish with K238E expressed at a lower level has significant cone loss at 4.5 months old (left) as compared to wild type sibling (center). Cone cytosol is in green (*gnat2:EGFP* with GFP antibody) and nuclei are in blue. Scale bar = 100μm.
F. Cone nuclei were counted across 1/3 of the dorsal side of the retina. There was significant cone loss for zebrafish containing lower expressed K238E compared with WT sibling at 4.5 months. n = 3 for both groups. * = p≤0.05 as determined by unpaired t test. Error bars are s.e.m.
G. 1 year old zebrafish with D226N mutation (left) show no signs of degeneration as compared to wild type sibling (right). Cone cytosol is in green (*gnat2:EGFP* with GFP antibody) and nuclei are in blue. Scale bar = 100μm.
H. Cone nuclei were counted across 1/3 of the dorsal side of the retina. There was no significant change in cone nuclei for D226N compared with WT sibling at 1 year. n = 2 for D226N and *Tg* WT and n = 3 for WT sibling. ns = not significant as determined by unpaired t test. Error bars are s.e.m.
I. *Tg* WT zebrafish at 2 years old show no signs of cone degeneration. Cone cytosol is in green (*gnat2:EGFP* with GFP antibody) and nuclei are in blue. Scale bar = 100μm.
J. WT siblings of zebrafish larvae containing K238E *impdh1* mutation OKR trace. Zebrafish larvae have forward (right) and reverse (left) OKR response at 5dpf.
K. Zebrafish larvae containing D226N *impdh1* mutation OKR trace (right) and WT sibling (left). Zebrafish larvae have forward and reverse OKR response at 5dpf.
L. Zebrafish larvae containing endogenous (WT sibling) or transgenic WT IMPDH1 (*Tg* WT) OKR trace. Zebrafish larvae have forward and reverse OKR response at 5dpf.

lactate:pyruvate ratio was significantly decreased with the D226N mutant (Fig. 4.3D). Total lactate levels remained constant between all samples (Fig. 4.3E), but total pyruvate levels were significantly higher in the D226N mutant (Fig. 4.3F). This suggests a decrease in NADH compared to NAD^+.

Manipulating Impdh1 activity does not significantly impact cGMP levels in the retina

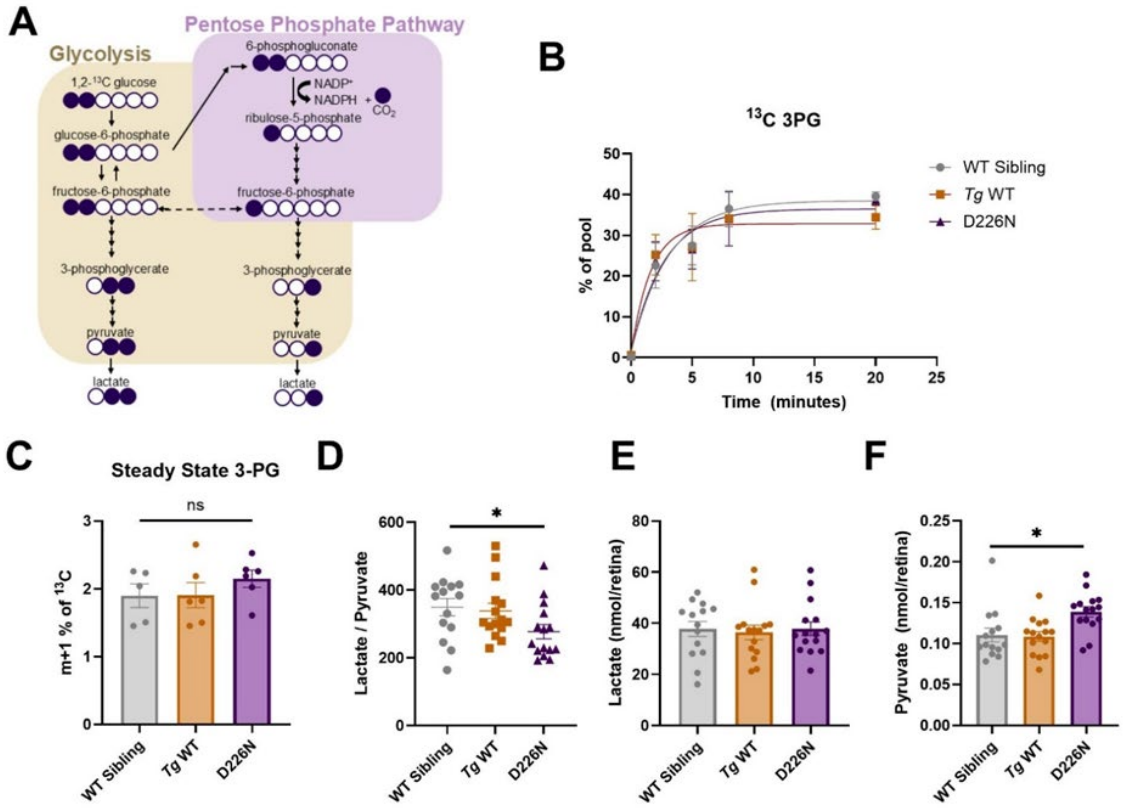

Figure 4.3: Glucose usage remains unchanged for Impdh1 mutant D226N.
A. Schematic illustrating labeling pattern using 1,2 ^{13}C glucose. If glucose goes through glycolysis, two heavy carbons remain whereas if glucose is diverted to the pentose phosphate pathway, only one heavy carbon remains.
B. Accumulation of ^{13}C 3PG over time. There are no differences in levels of labeled 3PG over time between D226N, *Tg* WT or WT sibling zebrafish retinas. n = 3 for all time points and groups except WT sibling at 8 hour time point (n = 2). Error bars are s.e.m.
C. Steady state levels of pentose phosphate derived 3PG (m+1). D226N mutation did not increase glucose diversion to pentose phosphate pathway. n = 5 for WT sibling and n = 6 for D226N and *Tg* WT. ns = not significant as determined by unpaired t test. Error bars are s.e.m.
D. Total lactate to pyruvate levels of D226N, *Tg* WT, or WT sibling zebrafish retinas. Zebrafish with D226N mutation have a lower lactate to pyruvate ratio. n = 14 for WT sibling and n = 15 for D226N and *Tg* WT. * = p≤0.05 as determined by unpaired t test. Error bars are s.e.m.
E. Total lactate levels (nmol/retina) for D226N, *Tg* WT, or WT sibling zebrafish retinas. There were no significant differences in total lactate levels. n = 14 for WT sibling and n = 15 for D226N and *Tg* WT. Error bars are s.e.m.
F. Total pyruvate levels (nmol/retina) for D226N, *Tg* WT, or WT sibling zebrafish retinas. Total pyruvate was higher for zebrafish with D226N *impdh1* mutation. * = p≤0.05 as determined by unpaired t test. n = 14 for WT sibling and n = 15 for D226N and *Tg* WT. Error bars are s.e.m.

cGMP is a key signaling molecule in phototransduction. It is well established that increases in cGMP lead to photoreceptor degeneration (Iribarne and Masai, 2018; Power et al., 2020). cGMP is made from GTP (Fig. 4.4A). We hypothesized that by manipulating the rate-limiting enzyme in *de novo* purine biosynthesis, Impdh1, we could manipulate GTP levels and consequently alter cGMP pool sizes. Hyperactive Impdh1 could cause high steady state levels of cGMP. To evaluate this, we used mass spectrometry to measure steady state cGMP in retinas/eyes from *Tg* K238E, *Tg* D226N, or *Tg* WT zebrafish and compared these results to age-matched non-transgenic retinas. We found no increase in steady state levels of cGMP for either *Tg impdh1* mutant or *Tg* WT as compared to non-transgenic zebrafish retinas (Fig. 4.4B,C).

In photoreceptors, cGMP concentrations are maintained by the activity of phosphodiesterase 6 (PDE6), which converts cGMP to GMP in the light (Arshavsky et al., 2002). Loss of PDE6 in either rods or cones leads to photoreceptor degeneration (Farber and

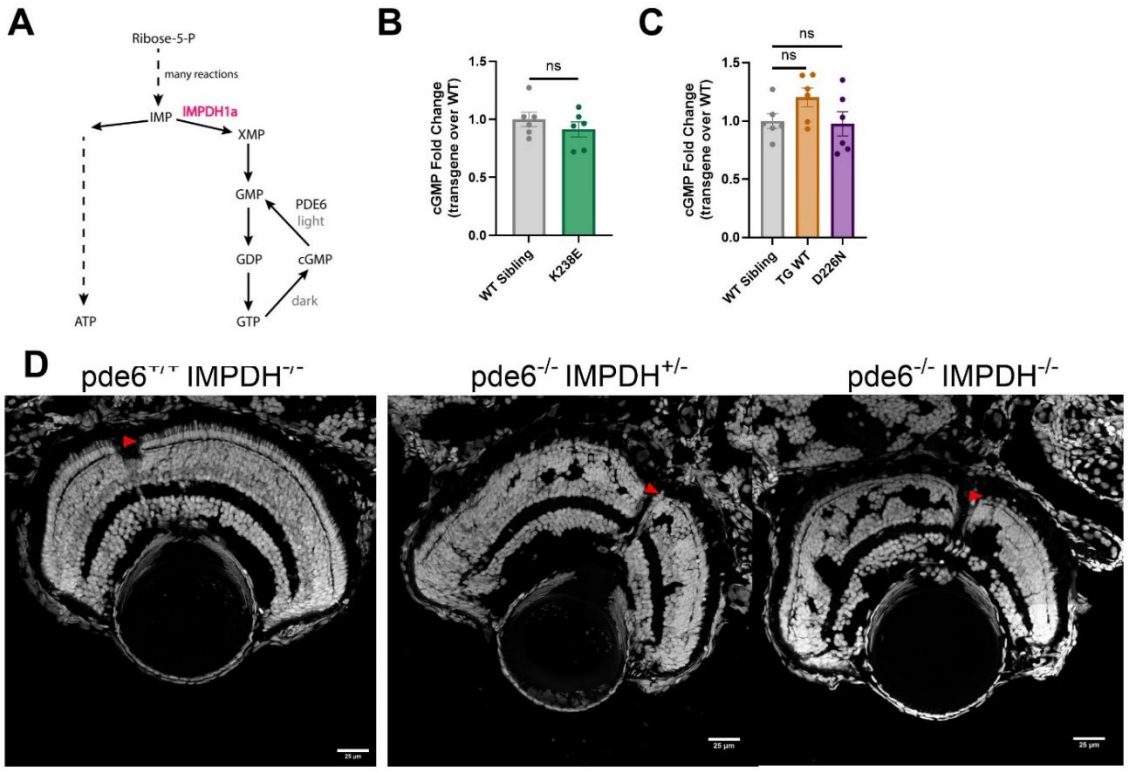

Figure 4.4: Altering Impdh1 does not impact cGMP levels.
A. Schematic of *de novo* purine biosynthesis of cGMP with IMPDH1a highlighted in red. In the light, PDE6 converts cGMP into GMP.
B. Steady state levels of cGMP from K238E mutant zebrafish or WT siblings. ns – not significant as determined by t test. Zebrafish with class 1 mutant, K238E, do not have raised steady state levels of cGMP. n = 6 for both groups. ns = not significant as determined by unpaired t test. Error bars are s.e.m.
C. Steady state levels of cGMP from *Tg* WT, D226N mutant, or WT zebrafish. ns – not significant as determine by t test. Zebrafish with class 1 mutant, D226N, do not have raised steady state levels of cGMP. n = 6 for all groups. ns = not significant as determined by unpaired t test. Error bars are s.e.m.
D. Larval optic nerve slices with nuclei stained with Hoechst. Scale bar = 25μm. Impdh1 KO zebrafish shows no signs of degeneration whereas Pde6c mutant has severe signs of degeneration at 5dpf. The Pde6c mutant, Impdh1 KO zebrafish also show signs of severe degeneration by 5dpf. Knocking out Impdh1 did not rescue or delay degeneration of model with high cGMP. Red arrows point to cone layer.

Lolley, 1974; Kennedy et al., 2007; Power et al., 2020). To further evaluate whether cGMP levels could be influenced by changes in Impdh1a activity, we crossed a previously characterized Impdh1a knockout (KO) zebrafish (Cleghorn et al., 2022) with a zebrafish strain lacking the cone catalytic subunit of Pde6c (*pde6c*^{w59}) (Stearns et al., 2007). Loss of Pde6C causes rapid degeneration of zebrafish cones (Stearns et al., 2007). Knocking out Impdh1a does not cause photoreceptor degeneration but does cause a 50% decrease in retinal guanine levels (Cleghorn et al., 2022). We hypothesized that the loss of Impdh1 could slow cGMP production and thus rescue the Pde6C mutant by reducing levels of cGMP. By 5dpf, cone nuclei were absent from Pde6C mutant, but not from Impdh1 KO zebrafish as expected (Fig. 4.4D). However, cone loss in the Pde6C mutant zebrafish was not rescued by knocking out Impdh1 (Fig. 4.4D).

Impdh1 mutations cause alteration in steady state purine or pyrimidine metabolism

To more broadly analyze whether nucleotides were altered in our transgenic lines, we next measured steady state levels of both purine and pyrimidine metabolites. IMPDH1 converts IMP into XMP which can be converted into GMP and other downstream metabolites (Fig. 4.5A). If IMPDH1 is inhibited, IMP can be shunted to make AMP and its' other associated products or inosine (Fig. 4.5A). We isolated eyes from zebrafish with the K238E mutation prior to

degeneration and analyzed steady state metabolites from the purine and pyrimidine pathways.

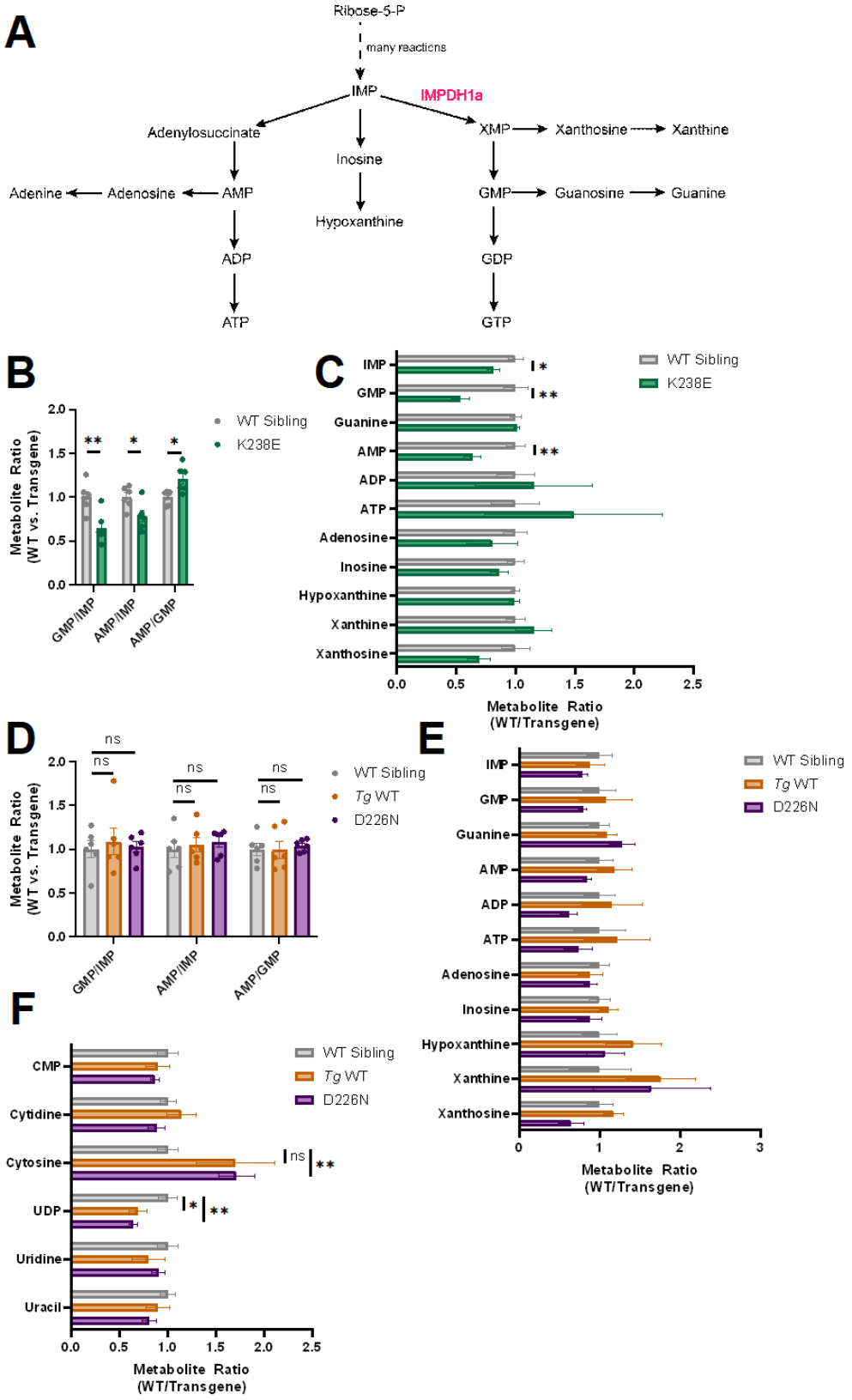

Figure 4.5: Impdh1 mutants impact purine or pyrimidine steady state metabolites.
A. Schematic showing *de novo* purine biosynthesis. IMPDH1a highlighted in red.
B. Steady state metabolite ratios of K238E mutant zebrafish compared to WT sibling eyes. GMP/IMP and AMP/IMP were lower in mutant compared to WT whereas AMP/GMP was higher in mutant. n = 6 for both groups. * = p≤0.05 ** = p≤0.005 as determined by unpaired t tests. Error bars are s.e.m.
C. Ratio of purine related metabolites for K238E or WT sibling zebrafish eyes. IMP, GMP, and AMP were significantly lower with K238E mutant as compared to WT. n = 6 for both groups. * = p≤0.05 ** = p≤0.005 as determined by unpaired t tests. Error bars are s.e.m.
D. Steady state metabolite ratios of D226N mutant or *Tg* WT zebrafish compared to WT sibling retinas. Neither D226N or *Tg* WT were significantly different as compared to WT siblings. n = 6 for all groups. ns = not significant as determined by unpaired t tests. Error bars are s.e.m.
E. Ratios of purine related metabolites for D226N, *Tg* WT or WT sibling zebrafish retinas. There were no significant differences between mutant and WT for purine metabolites as determined by unpaired t tests. n = 6 for all groups. Error bars are s.e.m.
F. Ratios of pyrimidine related metabolites for D226N, *Tg* WT, or WT sibling zebrafish retinas. Cytosine was significantly higher for D226N and UDP was significantly lower for both D226N and TG WT. n = 6 for all groups. * = p≤0.05 ** = p≤0.005 as determined by unpaired t tests. Error bars are s.e.m.

Zebrafish with the K238E Impdh1 mutation had lower GMP/IMP and AMP/IMP ratios (Fig. 4.5B). The AMP/GMP ratio was higher in the K238E mutant zebrafish as compared to non-transgenic siblings (Fig. 4.5B). IMP, GMP, and AMP metabolite levels were significantly lower in K238E mutants as compared to non-transgenic zebrafish (Fig. 4.5C). This suggests that instead of being hyperactive, the K238E mutation causes the protein to be inactive and to dominantly inhibit the synthesis of adenine nucleotides.

To analyze purine and pyrimidine metabolites for the D226N Impdh1a mutant zebrafish, we isolated retinas from dark adapted 3 month old zebrafish. D226N containing retinas, did not show any changes in GMP/IMP, AMP/IMP, or AMP/GMP ratios (Fig. 4.5D). *Tg* WT also had no changes in these ratios (Fig. 4.5D). Neither the D226N Impdh1 mutant or the *Tg* WT zebrafish had any changes in steady state purine metabolites (Fig. 4.5E). Cytosine, a pyrimidine metabolite, was significantly elevated for D226N but trended in the same direction for *Tg* WT (Fig. 4.5F). UDP, another pyrimidine metabolite was decreased significantly for both D226N and *Tg* WT (Fig. 4.5F). Overall, the metabolic phenotype of D226N appeared WT.

Impdh1 mutants have abnormally large filaments

WT cones have small Impdh1a filaments dispersed throughout the cell body, synapse, and occasionally the outer segment (Cleghorn et al., 2022). We analyzed the K238E Impdh1a mutant crossed with *Tg(gnat2:EGFP)* (cone cytosol marker) prior to degeneration with a custom Impdh1a antibody (Fig. 4.6A). The K238E mutant had large Impdh1a positive structures in the cone synapse (Fig. 4.6A). D226N mutant zebrafish had similar large structures in the synapse and small filamentous structures by the cone nuclei (Fig. 4.6A). These large structures are distinct from small filaments in non-transgenic zebrafish and cytosolic signal in *Tg* WT zebrafish (Fig. 4.6A).

To obtain better visualization of the Impdh1a filaments, we used expansion microscopy to enlarge our D226N samples 5.5x. With better resolution of the synapse, we observed large curved Impdh1a filaments or bundles of filaments (Fig. 4.6B,B'). We were also able to visualize the nuclear Impdh1a filaments with greater clarity and found that they are inside the nucleus (Fig. 4.6B,B''). In contrast, filaments were not identified previously in non-transgenic WT cones (Cleghorn et al., 2022).

To determine whether Impdh1a filaments could be impacting synaptic structure, we used TEM to evaluate synapse integrity. Cone synapses contained ribbons, vesicles, and no obvious defects (Fig. 4.6C) however, we noticed that in some of the mutant transgenic synapses (n = 11 structures (104 synapses) for D226N and n = 7 structures (58 synapses) for K238E), large filamentous structures were within the synapse, which was not detected in non-transgenic synapses (Fig. 4.6C).

Discussion

Photoreceptors require specific levels of cGMP for phototransduction and cGMP imbalances can lead to photoreceptor degeneration (Farber and Lolley, 1974; Power et al., 2020). In phototransduction, light activates a G protein-coupled receptor signaling pathway

where phosphodiesterase 6 (PDE6) is activated in photoreceptor outer segments. PDE6 then hydrolyzes cGMP to GMP, which leads to the closure of CNG channels (Arshavsky et al., 2002). During recovery from light stimulation, GMP from the outer segment is converted to GDP and subsequently GTP in the inner segment of photoreceptors (Wimberg et al., 2018). Guanylyl cyclase converts GTP to cGMP in photoreceptor outer segments thus re-opening CNG channels until phototransduction is re-activated. GTP derived from *de novo* purine biosynthesis is important for cGMP regeneration during phototransduction recovery (Plana-Bonamaisó et al., 2020). Light induced IMPDH1 phosphorylation can increase *de novo* purine biosynthesis

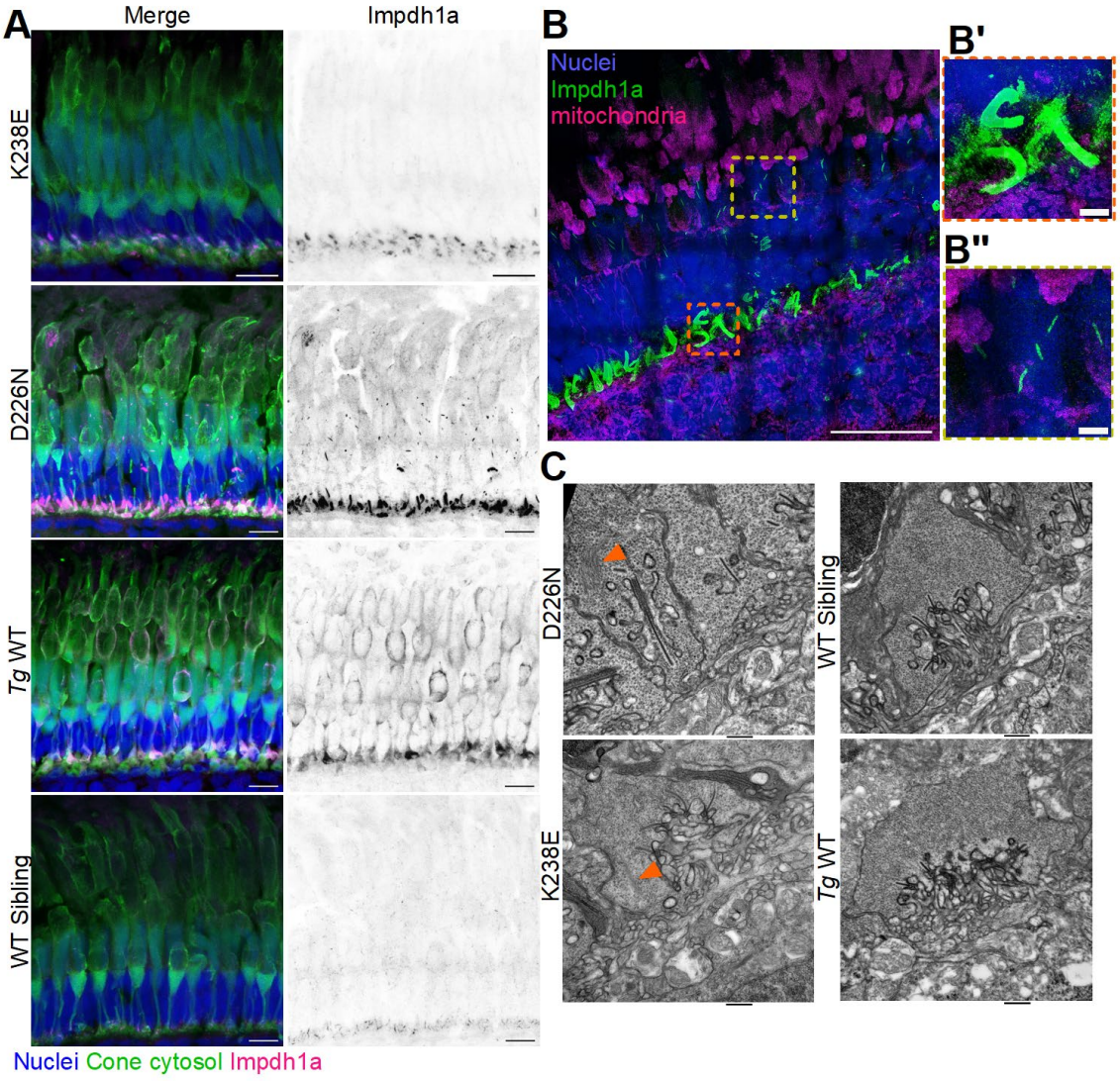

Figure 4.6: Mutant Impdh1 filaments are larger and localized to synapse (K238E) or synapse and nucleus (D226N).
A. K238E Impdh1 mutant, D226N Impdh1 mutant, *Tg* WT, or WT siblings were crossed with *TαCP:eGFP* (cone cytosol, green) and retinal sections were stained with Hoechst (nuclei, blue) and a custom Impdh1 antibody (magenta). K238E mutant has larger filaments at cone synapse. D226N mutant has larger filaments at cone synapse and nuclei whereas *Tg* WT had diffuse cytosolic Impdh1 staining. Scale bar = 10μm.
B. D226N Impdh1 mutant retinal sections expanded 5.5x. Nuclei (blue), Impdh (green), and mitochondria (magenta). B' is a zoomed in area of cone synapse (orange box) and B'' is a zoomed in area of Impdh1 filament in cone nuclei yellow box). Scale bar for C is 10μm and 1μm for B' and B''. All scale bars corrected by expansion factor (5.5).
C. TEM of cone synapses of D226N, K238E WT sibling, or *Tg* WT. IMPDH1 mutants D226N and K238E have filamentous structures in synapse (orange arrows). Zebrafish eyes were taken prior to degeneration. Scale bar for D226N is 600 nm. All other scale bars are 500 nm.

(Plana-Bonamaisó et al., 2020). In zebrafish retinas, Impdh1a mediated purine biosynthesis accounts for half of the guanine pool, the nucleobase for GTP (Cleghorn et al., 2022).

Mutations in PDE6 can lead to photoreceptor degeneration due to high levels of cGMP (Farber and Lolley, 1974; Power et al., 2020). Inhibiting IMPDH1 pharmacologically can be sufficient to delay PDE6B induced photoreceptor degeneration stemming from elevated levels of cGMP (Yang et al., 2020). Although guanine levels are dramatically reduced in retinas from zebrafish lacking Impdh1a, Pde6c-related photoreceptor degeneration was not delayed by knocking out *impdh1a* (Fig. 4.4D). Yang et al. reported that the effect of the IMPDH inhibitor was not as strong with rd1 mouse with faster degeneration (Yang et al., 2020). Similarly in the *pde6c*^{w59} mutant, it is possible that the cGMP levels are too high to be delayed by manipulating IMPDH1 alone. Additionally, cGMP could be produced by recycling purine bases through the salvage pathway. More work is needed to delineate the contributions of *de novo* purine biosynthesis and the salvage pathway in the retina during physiological and pathological states.

Hyperactive IMPDH1 could lead to elevated levels of downstream products including GMP and GTP (Fig. 4.4A). The Km of inactivated GC ranges from 1.6-3.2 mM and photoreceptor GTP concentrations have been estimated to be approximately 2.5 mM (Peshenko et al., 2011). If GTP levels were higher due to aberrant IMPDH1 activity, then cGMP could

elevate and initiate cell death. Similar to human IMPDH1 (Burrell et al., 2022; Burrell and Kollman, 2022), zebrafish Impdh1a with K238E or D226N mutations had disrupted GTP inhibition *in vitro* (Fig. 4.1G). The lack of IMPDH1 allosteric inhibition by GTP could increase *de novo* purine biosynthesis activity leading to increased cGMP levels. One of the starting substrates for *de novo* purine biosynthesis is phosphoribosyl pyrophosphate (PRPP). To produce PRPP, ribose-5-phosphate from the PPP is needed. If *de novo* purine biosynthesis flux was increased, we would expect glucose diversion to the PPP to generate more substrates. We did not see an increase in m+1 labeled 3-PG, indicating that PPP flux remains unchanged (Fig. 4.3B,C). We also observed the NAD^+/NADH ratio (using lactate/pyruvate as a proxy) was decreased in D226N mutant zebrafish, opposite of what we would expect if Impdh1 were hyperactive (Fig. 4.3D). Additionally, the steady state levels of cGMP were not elevated for either mutant (Fig. 4.4B,C). This all strongly suggests that Impdh1a with K238E or D226N mutations do not increase guanine nucleotide and cGMP synthesis and that compensatory biochemical reactions can adapt and compensate for the hyperactive IMPDH.

Although we did not find evidence for Impdh1a hyperactivity *in vivo*, there were significant alterations in steady state metabolism and Impdh1a filament polymerization and localization. Metabolites associated with *de novo* purine biosynthesis, including IMPDH1 have been known to dynamically associate into a complex coined the purinosome (Pedley and Benkovic, 2017; Zhao et al., 2015). Disruptions in protein-protein interactions or localization of these complexes could cause downstream metabolite imbalances. K238E had significantly lower GMP, AMP, and IMP suggestive of less *de novo* purine biosynthesis activity (Fig. 4.5B,C). Adenylosuccinaete synthetase (ADSS) and IMPDH are both enzymes in purinosomes (Zhao et al., 2015). A disruption in this interaction could explain the reduction in AMP and GMP levels. D226N, another class I IMPDH1 mutant, had normal steady state *de novo* purine biosynthesis, but had abnormal levels of cytosine and UDP, metabolites in pyrimidine synthesis (Fig. 4.5E,F). Notably, *impdh1a* expressed at a higher level also had significantly lower UDP and trended

higher for cytosine indicating this effect may be due to *impdh1a* expression level (Fig. 4.5F). IMPDH1 is known to interact with CTP synthase in cell culture (C.-C. Chang et al., 2018). A change in interaction between these two proteins would explain the alteration in steady state cytosine with the D226N Impdh1a mutation (Fig. 4.5F). More work is needed to determine if IMPDH1 interacts with other proteins, like ADSS and CTP synthase, in the retina. Additionally, IMPDH1 phosphorylation can impact enzyme activity (Calise et al., 2024; Plana-Bonamaisó et al., 2020). These large Impdh1a structures may have altered activity due to a change in phosphorylation.

IMPDH1 also has moonlighting roles which could be causative of photoreceptor degeneration. IMPDH1 can interact with single stranded DNA and when expressing D226N in cell culture, the affinity of IMPDH1 for single stranded DNA decreases (Mortimer and Hedstrom, 2005). IMPDH1 can also interact with polyribosomes translating rhodopsin mRNA (Mortimer et al., 2008). However, it is unclear if IMPDH1 mutations disrupt this interaction and whether it would lead to a change in rhodopsin protein levels. Further, mice with only a single rhodopsin gene only have a mild retinopathy (Lem et al., 1999).

It is unclear why D226N mutant zebrafish cones did not degenerate. One explanation may be that this mutation in humans preferentially affects rods and not cones, another possibility is that zebrafish cones are somehow protective from the effects of this mutation. Either possibility would highlight important information regarding the mechanism of photoreceptor cell death. Since we did not examine the visual responses of adult D226N cones, it is also possible that their function is altered. Overall, our study quantifies the biochemical consequences of IMPDH1 mutations *in vivo* and our findings suggest that it is protein-protein interactions and/or filament size and location that could contribute to the disease caused by these mutations.

Materials and Methods

Zebrafish Maintenance

The University of Washington Institutional Animal Care and Use Committee authorized this research. Zebrafish were kept on a 14 hour/10 hour light/dark cycle at 27.5°C at the University of Washington South Lake Union aquatics facility. Zebrafish were kept in the Roy/AB or AB background for experiments. Unless otherwise noted, zebrafish between 1 – 12 months were used for experiments (prior to degeneration). When possible, a mixture of male and female zebrafish were used for experiments.

Transgenic line generation

Mutations were introduced into WT *impdh1a_tvX1* (XM_005159007) in pCR8 (Invirtogen) using the primers D306NmutF ((ctcggttcttcttcaaattggtacgagcgattattgc), D306NmutR (gcaataatcgctcgtaccaatttgaagaagaaccgag), K318EmutF2(gtttgcgggagtcttcggaggccagaggata) and K318EmutR2 (tatcctctggcctccgaagactcccgcaaac). D306N and K318E in *impdh1a tvX1* are equivalent to D226N and K238E in and human IMPDH1 (NM_001142573.2). Constructs were generated using Gateway-Tol2 assembly. Assembly of the expression vector was done by combining the WT or mutated *impdh1a* pCR8 plasmid, an entry vector containing the previously characterized *gnat2* promoter (Kennedy et al., 2007), and a bleeding heart containing destination vector (Williams et al., 2010). Constructs were injected into 1-cell embryos with Tol2 transposase mRNA as previously described (Kennedy et al., 2007) and three transgenic zebrafish lines were generated; Tg(*gnat2:impdh1a-X1-K238E*), Tg(*gnat2:impdh1a-X1-D226N*), and Tg(*gnat2:impdh1a-X1*). Single-insertion carriers from the F2 generation and beyond were used in this study. Each new generation was evaluated for continued transgene expression. The Tg(*gnat2*:GFP) zebrafish line was established previously (Kennedy et al., 2007).

***In vitro* protein assays**

Purified IMPDH1 was diluted in 20 mM Hepes, 100 mM KCl, and 1 mM DTT, pH 7.0. 1 uM IMPDH1, 1mM ATP, 1 mM IMP, 300 μM NAD^+ and various GTP concentrations were added to a 96 well UV transparent plate. Using a Varioskan Lux microplate reader (Thermo Scientific) kept at 25°C, NADH production was measured at 340 nm by optical absorbance. 1 measurement/minute was collected for 15 minutes and absorbances were correlated with NADH concentrations generated from a standard curve. Measurements were performed in triplicate.

Western Blot

Twenty whole eyes were enucleated from 7dpf zebrafish larvae. Samples were homogenized on ice and then left on a shaker at 4°C for 30 minutes. Samples were spun down at maximum speed in a microfuge for 15 minutes and then the supernatant was collected. 12-20 ug of protein was added to each lane. Blots were probed with a custom rabbit anti-Impdh1 antibody at [1:500], mouse anti-myc antibody at [1:500] (Cell Signaling Technology, 9B11), and an anti-beta-actin antibody at [1:1000] (Abcam, ab8226) as previously described (Bisbach et al., 2020b; Cleghorn et al., 2022). Blots were washed and incubated in secondary antibodies for 1 hour prior to developing. Secondary antibodies were IRDye 680RD Donkey anti-Rabbit IgG (Li-Cor, 926-68073) and IRDye 800CW Goat anti-Mouse IgG (Li-Cor, 926-32210). The ladder used was Precision Plus Protein Duel Color Standards (Bio-Rad, 1610374) or Precision Plus Protein All Blue Prestained Protein Standards (Bio-Rad, 1610373). Signal intensity of IMPDH band was divided by signal of actin band. WT was normalized to one and transgenic line value was subtracted by 1 to account for WT expression of IMPDH1a.

Immunohistochemistry

Eyes were enucleated and put in 4% paraformaldehyde (PFA) fix at room temperature for 10 minutes. Holes were poked through the sclera and eyes were kept in PFA for an additional 2

hours at room temperature before being moved to 4°C fridge for 48 hours. Eyes were then sucrose protected overnight and embedded in OCT. Eyes were sectioned at 14-20μm and warmed on a slide warmer for 2 hours. Sections were incubated in IHC PBS for 10 minutes and then blocked with normal donkey serum-based blocking buffer for 30 minutes. Samples were then left overnight to incubate in primary antibodies at 4°C. ([1:5000] EGFP (Abcam, ab12970), [1:500] myc 9B11 (Cell Signaling Technology); [1:500] custom Impdh1 antibody (Cleghorn et al., 2022). Primaries were removed the following day and slides were washed three times with IHC PBS. Secondaries were added at [1:2000] for 1 hour at room temperature. Secondary antibodies used included Goat anti-Chicken 488 (Invitrogen, A11039), Goat anti-Rabbit 633 (Invitrogen, A21071), and Goat anti-Mouse 568 (Invitrogen, A11004). Slides were washed twice with IHC PBS and incubated with Hoechst 33342 (Invitrogen, H1399) for 10 minutes at room temperature. Sections were dried and sealed with Fluoromount G and nail polish. Slides were imaged on a Leica SP8 confocal microscope. Images were processed using ImageJ.

Nuclei Quantification

A third of the dorsal side closest to the optic nerve was used for quantification. Prior to quantification, the image was straightened and the nuclear channel was set to grayscale. Cone nuclei were quantified using the number marker tool in ImageJ.

OKR

Equipment comprised of a variable speed motor (Model LV3607; Electro Motor and Control Corporation); a Wild M3Z stereomicroscope with a bottom and ring light source; a camera attached on top, a plastic drum mounted directly above the base light source made of smooth plastic lined with paper containing alternating vertical black and white stripes (~1 cm in width), with a circular base and a motor pulley sitting 26 cm from the center of the drum (Brockerhoff, 2006). The camera was attached to a TV monitor and an iPhone 12 was positioned on a tripod

in front of the monitor to record OKR. Methylcellulose was aliquoted into a 30mm x 15mm petri dish with 5 day old larvae placed into the reagent one at a time. Fish were positioned upright and toward the edge of the petri dish for better visualization of the lined paper. This apparatus was then placed underneath the stereoscope for observation. OKR was recorded with the iPhone for 10-20 seconds. The experiment was repeated to observe zebrafish OKR in the reverse direction of the lined paper. For D226N, continuous videos of 20-30 seconds were taken with a direction switch around 10-15 seconds.

OKR Quantification

The most active eye was chosen for OKR measurements which were done manually by overlaying the video on a transparent protractor image. Changes in the angle of the eye were measured for each video frame (every 0.2 seconds). Clockwise stripe rotations were designated to be ≥90 degrees while the counterclockwise direction was designated as ≤90 degrees.

Transmission Electron Microscopy

TEM was conducted as previously described (Hutto et al., 2020).

Expansion Microscopy

20 µm cryosections were first stained via immunohistochemistry. Following 1 h blocking (5% normal donkey serum, 1% bovine serum albumin, 1% Triton-X-100 in phosphate buffer, pH 7.4), sections were incubated overnight at room temperature (RT) in primary antibodies diluted in blocking buffer (1:400 rabbit anti-Impdh1aN, (Cleghorn et al., 2022); 1:200 mouse anti-MTCO1, Abcam #ab14507). Following 3 washes with phosphate buffer, sections were incubated 2 h at RT in secondary antibodies (1:50 goat anti-rabbit AlexaFluor 546, Invitrogen #A11071; 1:50 goat anti-mouse AlexaFluor 488, Invitrogen #A11017) and Hoechst 33342 (1:10, Invitrogen #H1399). Following 3 washes with phosphate buffer, sections were incubated overnight at RT in 0.1

mg/mL acryloyl X-SE in MES buffer, pH 6.0. Sections were washed twice with phosphate buffer, then incubated overnight at RT in inactivated monomer solution (7.5% sodium acrylate, 2.5% acrylamide in MOPS buffer, pH 7.0), and washed twice again with phosphate buffer. Subsequent steps of gelation, digestion, and expansion were carried out as described by Asano et al 2018, using the proExM protocol for intact tissues. Expanded gels were immobilized using super glue and a harp (Warner Instruments), and imaged in water. Z-stack images were acquired using a Leica SP8 confocal microscope with a 40X water dipping lens and LAS-X acquisition software. Presented images were deconvolved using Leica Lightning and maximum intensity projected.

LC/MS sample collection and processing

Zebrafish were starved overnight and dark adapted for 1 hour prior to dissections. 10 whole eyes (1 month samples) or 4 retinas (3.5 month samples) were removed and flash frozen. Retina or eyes were homogenized in cold 80% methanol, stored on dry ice for 30 minutes, and centrifuged at 14,000 RPM at 4^{o}C for 15 minutes. The supernatant was dried down and reconstituted in mobile phase (30:70 in V/V of A:B) for targeted metabolomics as reported (Saravanan et al., 2023). Metabolite extracts were analyzed by a Shimadzu LC Nexera X2 UHPLC coupled with a QTRAP 5500 LC-MS/MS (Ab Sciex) with an ACQUITY UPLC BEH Amide analytic column (Waters Corp). The mobile phase was (A) 10 mM ammonium acetate (pH 8.9) in water and (B) 95/5 acetonitrile/water with 10 mM ammonium acetate (pH 8.2). The injection volume was 5 µL and the flow rate was 0.5 mL/min with a total run time of 11 minutes. The gradient elution was 95 to 61% B in 6 min, 61 to 44% B at 8 min, 61 to 27% B at 8.2 min, and 27 to 95% B at 9 min. The column was equilibrated with 95% B at the end of each run. The source and collision gas were N2. The ion source conditions in positive and negative mode were as follows: curtain gas (CUR) = 25 psi, collision gas (CAD) = high, ion spray voltage (IS) = 3800/−3800 V, temperature (TEM) = 500 °C, ion source gas 1 (GS1) = 50 psi, and ion source

gas 2 (GS2) = 40 psi. Each metabolite was tuned with standards for optimal transitions. Nicotinamide-D4 (Cambridge Isotope Laboratories) was used as an internal standard. The extracted MRM peaks were integrated using MultiQuant 3.0.3 software (AB Sciex).

GC/MS sample collection and processing

Zebrafish were dark adapted 1 hour prior to collection. Retinas were dissected in Krebs-Ringer buffer with 5mM glucose added. Retinas were then moved into 1,2 13C glucose and kept in an incubator at 37°C with 5% CO2 for various timepoints. Metabolites were extracted by adding 80% methanol and sonicated. Samples set on dry ice for 45 minutes to precipitate metabolites and then spun down at 17,000xg for 30 minutes at 4°C. Supernatant was collected and dried down. Samples were derivatized by adding 10µL of 20 mg/mL of methoxyamine HCl in pyridine. Samples were incubated for 90 minutes in a 37°C oven. 10µL of TBDMS was added and put on a heating block set to 70°C for 1 hour. Samples were run on an Agilent 5985 GC-MS, processed with MSD ChemStation software (Agilent), and corrected with IsoCor software (Millard et al., 2012).

Acknowledgements

We thank the UW SLU Aquatics for zebrafish care and maintenance, notably Nicole Fan and Stanley Kim. The UW Vision Core provide both resources for light and electron microscopy and we thank Ed Parker for processing our TEM samples. The UW Mass Spectrometry Core and especially Martin Sadilek helped with GC/MS for the glucose flux assay. We thank the following for processing samples, troubleshooting experiments, and thoughtful conversations: William Wu, Matthew Liu, Riddhi Atmakuri, Chloe Sygitowicz, Jim Hurley, and Daniel Hass.

Funding

Our funding sources are National Institutes of Health F31EY033983 (KMR), R01EY033731(SEB,JMK), EY031324 (JD), EY032462(JD), and the Retina Research Foundation (JD).

Chapter 5 – Conclusions and Future Directions

In this thesis, I describe ways cones can be robust through mitochondrial dynamics yet vulnerable to perturbations in purine metabolism. Cones are post-mitotic cells that have high energy demands. Generally, we retain cones throughout our lifetime despite high stress and energy demands. We've found that cones can adapt to energy demands by changing their mitochondria. If subjected to stress, cone mitochondria can also migrate away from the cluster, leave the cell, and be taken up by nearby Müller glia. These mechanisms can help the cell stay healthy and robust to perform essential visual functions. We evaluated a metabolic stressor – mutations in IMPDH1, one of which caused early cone degeneration. We found that disruptions in the steady-state purine pool and large mislocalized IMPDH1 filaments correlated with cone degeneration. In summary, this thesis has demonstrated:

1. Cone mitochondrial clusters can remodel throughout the day and night.
2. In darkness, cone mitochondria extrude material out of the photoreceptor cell.
3. Zebrafish larval cone mitochondria respond to various stressors by moving mitochondria away from the mitochondrial cluster towards the synapse and out of the cell.
4. Müller glia can take up unhealthy cone mitochondria.
5. cGMP levels in the retina are regulated independently of IMPDH1a.
6. IMPDH1 mutant, K238E, degenerates and has abnormal purine metabolite levels.
7. IMPDH1 mutants cause abnormally large filaments in photoreceptor synapses.

Cone mitochondria are dynamic throughout the day and night

Conclusions 1 & 2

Prior to this work, it was unclear how mitochondria adapt to changing cone energy demands. Cones have high energy demands that are highest at nighttime (Okawa et al., 2008). In Chapter 2, we described zebrafish cone mitochondria size, localization, and morphology throughout the day and night. We found that there are more small mitochondria at night in single cones (Fig. 2.1D). In all cone types, mitochondria were simpler at night (Fig. 2.2F). To

accomplish this, mitochondrial biogenesis genes peak in the evening time, and there are fewer autophagosomes (Fig. 2.4A-F). Although important for energy generation, as evident with our SDH activity increasing at night (Fig. 2.6), cone mitochondria have other interesting functions – such as guiding light to the outer segments (Ball et al., 2022). Mitochondrial dynamics throughout the day and night are critical for mitochondrial function and homeostasis.

Interestingly, we found dark, electron dense material connected to mitochondria exiting photoreceptors at night (Fig. 2.5). This was found more prevalently in cones, and rarely in rods (Fig. 2.5D). Although the exact composition of the deposits is unclear, it could be damaged mitochondrial proteins or other components for degradation outside cones. As detailed in Chapter 3, Müller glia can support cone health by turning over unhealthy cone mitochondria. It would be interesting to investigate if these deposits contact Müller glia.

Photoreceptor mitochondria can be ejected and turned over by Müller glia

Conclusions 3 & 4

In an adult zebrafish with high mitochondrial calcium, swollen, electron-lucent mitochondria migrated towards the nucleus (Hutto et al., 2020). In this case, mitochondria did not leave the cell, and cones eventually degenerated. Also in adult cones, mitochondria were seen away from the ellipsoid region under unstressed conditions (Fig. 2.4G). Mitochondrial movement may be a mechanism for maintaining healthy cone mitochondrial pools in adult zebrafish.

In Chapter 3, we hypothesized that different stressors would invoke similar mitochondrial movement. Not only did we observe mitochondrial movement away from the ellipsoid region and towards the synapse (Fig. 3.1A-E), we found that cone mitochondria can be ejected from the cell (Fig. 3.2C-E). This occurred in various types of stress – whole body and cone mitochondrial specific stress (Fig. 3.1A-E). Additionally, we found that this mitochondrial movement occurred

to a lower extent in unstressed conditions, suggesting a mechanism that healthy cones use to maintain optimal mitochondrial pools (Fig. 3.1A-E).

We capitalized on the fact that zebrafish larvae can be transparent to do time-lapse imaging with various fluorescent markers targeted to cone mitochondria. Cone mitochondria left the cell to be taken up by Müller glia (Fig. 3.3A-D). We were able to get further details on the mislocalized mitochondrial structure using TEM. We found several electron lucent mitochondria in Müller glia (Fig. 3.3E-G). We were able to correlate these electron lucent mitochondria to cone mitochondria using CLEM (Fig. S3F). Additionally, we captured a mitochondrion mid-transfer to a neighboring Müller glia (Fig. S2D-G). This data shows that cones can transfer unhealthy mitochondria to Müller glia through direct contact with glia. After being taken up by Müller glia, we found that autophagy proteins in Müller glia associated with damaged cone mitochondria (Fig. 3.4D-H).

Prior to our work, photoreceptors were not known to transfer mitochondria for degradation or otherwise. This feature is not unique to the eye, however. Retinal ganglion cells in mice have been known to transfer mitochondria to nearby astrocytes in the ganglion cell axons (Davis et al., 2014). Retinal ganglion cells have long axons that span from the retina to the brain, highlighting a reason for efficient local mitochondrial homeostasis. Transcellular mitophagy has been shown in several other tissues, as reviewed here (Borcherding and Brestoff, 2023). Outside mitophagy, some studies have shown that healthy mitochondria are transferred to cells. For example, after an ischemic stroke, healthy mitochondria from astrocytes are transferred to neurons, helping minimize damage (Hayakawa et al., 2016). An exciting avenue to explore would be to test how photoreceptors regenerate mitochondria after stress.

Mitochondrial transfer has clinical potential to treat a variety of diseases. Several eye diseases impact photoreceptor metabolism. Knowing that cones are capable of mitochondrial transfer, it would be interesting to test whether they can take up healthy mitochondria and if that

would aid in delaying or preventing retinal disease. Several strategies for mitochondrial transfer for retinal disorders are reviewed here (Chi et al., 2025).

Class I IMPDH1 mutants do not cause elevated cGMP in zebrafish retinas

Conclusion 5

In vitro class I IMPDH1 mutations are not inhibited by GTP. Hyperactive IMPDH1 could influence cGMP levels in the retina, and elevated cGMP has led to cone death in other models (Farber and Lolley, 1974; Power et al., 2020). We found no evidence of elevated cGMP in either class I mutant model, suggesting a different mechanism of degeneration. Although treating a mouse model of retinitis pigmentosa with an IMPDH1 inhibitor delayed rod degeneration (Yang et al., 2020), our data suggests that manipulating Impdh1a does not impact cGMP levels (Fig. 4.4). Our *pde6c*^{w59} mutant was not rescued by knocking out Impdh1a (Fig. 4.4D). This could be due to an early and rapid increase in cGMP leading to degeneration. The mouse RP model that had more profound delayed degeneration with an IMPDH inhibitor had a slower accumulation of cGMP and later degradation (Yang et al., 2020). Furthermore, cGMP was not decreased in an Impdh1a knockout fish, suggesting either that cGMP is not tied with Impdh1a activity or the retina has compensated by upregulating the salvage pathway (Cleghorn et al., 2022).

Zebrafish expressing K238E mutation have abnormal steady-state purine metabolism

Conclusion 6

Although steady-state cGMP levels were stable in the zebrafish cones expressing the K238E Impdh1a mutation, there were significant metabolic decreases in IMP, AMP, and GMP (Fig. 4.5B,C). If Impdh1a were hyperactive *in vivo*, I would expect IMP and AMP to be lower but GMP to be higher. This phenotype is also distinct from the knockout, where only the GMP side of the pathway was impacted (Cleghorn et al., 2022). This suggests that the production of IMP, AMP, and GMP are all slowed down. Impdh1a is known to associate with the purinosome and

these protein-protein interactions could be disrupted with the K238E mutant Impdh1a (Pedley and Benkovic, 2017; Zhao et al., 2015). For example, if fewer purinosomes were formed, there would likely be less flux through the *de novo* purine biosynthesis pathway, yielding this result. This metabolic phenotype could contribute to cone degeneration in this model.

D226N, another class I mutant, did not have an apparent metabolic defect nor showed significant signs of degeneration by 2 years (Fig. 4.2E,F; 4.5D-F). Cytosine and UDP were significantly altered in the D226N mutant but these metabolites were either significant or trended in the same direction for the *Tg* wild type Impdh1a zebrafish, suggesting that higher levels of Impdh1a could cause that phenotype (Fig 4.5F). Although structurally present, it's possible that adult cones expressing the D226N mutation are not functional. Alternatively, cones may have a protective mechanism that prevents degeneration with this mutant. It is unclear if rods would have a similar phenotype or degenerate.

IMPDH1 mutations have abnormally large, mislocalized filaments

Conclusion 7

Both Impdh1a mutant zebrafish models had large mislocalized Impdh1a filaments localized to cone synapses (Fig. 4.6A-C). *Tg* WT had diffuse cytosolic Impdh1a signal (Fig. 4.6A). Large bundles of Impdh1a filaments may disrupt normal protein-protein interactions. Phosphorylation of IMPDH1 has been shown to impact filament assembly and activity and alterations (Calise et al., 2024; Plana-Bonamaisó et al., 2020). D226N also had filaments localized inside the nucleus (Fig. 4.6B''). IMPDH filaments have been observed in the nuclei of human gliomas, and a separate study has shown IMPDH to be a transcription factor (Ahangari et al., 2021; Kozhevnikova et al., 2012). Additionally, IMPDH is known to associate with rhodopsin RNA (Mortimer et al., 2008; Mortimer and Hedstrom, 2005). D226N may have abnormal DNA or RNA associations that could lead to cell death in rods.

Future Directions

The work presented in this thesis laid foundational work for understanding mitochondrial dynamics and homeostasis in cones and for dissecting the disease mechanism of IMPDH1 related ad-RP or LCA. There are many exciting avenues to further this work.

In Chapter 2, we examined mitochondrial dynamics throughout the day and night. To be more specific, we reported on mitochondrial size, location, and complexity in different types of zebrafish cones. We also found that mitochondrial biogenesis genes peaked in the evening, and a mitochondrial fusion gene, *mfn2,* rose in the morning. We could expand this work by preventing mitochondrial biogenesis or fusion to test if mitochondrial size or shape changed. If mitochondrial dynamics were altered, it could impact cone health or function. We also found dark deposits exiting cone mitochondria into the extracellular space. The identity of the dark deposits remains unknown. Future work could entail deciphering components of the dark deposits, such as mitochondrial proteins or lipids. It would also be interesting to test if dark deposits increase with cone mitochondrial stress. Using our transgenic zebrafish with KillerRed targeted to cone mitochondria, we could test if deposits increase with higher levels of reactive oxygen species.

Under stressed conditions (and to a lower extent in unstressed conditions), cone mitochondria migrate out of the cell and into Müller glia for turnover (Chapter 3). It is unclear whether this phenomenon extends to adult zebrafish cones, other animal models, or humans. More details on the mechanism of extrusion would be helpful. If we could block the extrusion, it would be interesting to see if the cones can compensate or if they eventually degenerate. Another exciting avenue would be exploring how cones replenish their mitochondria. Using RNAscope™, we can detect mitochondrial DNA and RNA in zebrafish retinal mitochondria (Giarmarco et al., 2024). It could be that cones exclusively support their own mitochondrial biogenesis or that another cell type, such as Müller glia, supplies cones with healthy

mitochondria. Transfer of healthy mitochondria has previously been observed in other tissues (Borcherding and Brestoff, 2023).

Generating three novel animal models for Impdh1a-associated photoreceptor degeneration opens many doors for future exploration. In chapter 4, we focused on purine and pyrimidine steady-state metabolism. This could be expanded to metabolic flux experiments where we can test if the rate of metabolite production changes with different transgenic lines. Purine metabolism is largely unstudied in cones. Using our mutants and knockout model, we could test the contributions of *de novo* purine biosynthesis and the salvage pathway in healthy and diseased states.

We also observed large mislocalized Impdh1a filaments. It's unclear if Impdh1a interacts with other metabolic proteins in zebrafish cones and if that interaction is disrupted with these large filaments. A potential interaction with adenylosuccinate synthase (ADSS) in the K238E model is of interest because of the reduction in AMP. These protein-protein interactions could be evaluated by immunohistochemistry or protein proximity labeling methodology.

We also found that knocking out Impdh1a was insufficient to rescue *pde6c*^{w59}-related degeneration. This could be because cGMP levels are too high or rise too rapidly. We could test other zebrafish models with slower degeneration due to high levels of cGMP to see if degeneration could be delayed or rescued.

Summary and Impact

In Chapter 2, I describe mitochondrial homeostasis throughout the day and night. This work is critical for understanding how photoreceptors handle higher energy demands at night. The dark deposits are an exciting new avenue to further explore in healthy and diseased states. I next describe a project in Chapter 3 regarding cone mitophagy in stressed and unstressed conditions. We found that cones can transfer damaged mitochondria to Müller glia for turnover. Understanding how cones handle increased stress gives us insight into how these post-mitotic

cells are long-lived. Insights on how photoreceptors remain healthy can be informative for future therapeutics aimed at delaying photoreceptor degeneration. Finally, in Chapter 4, I discuss a fundamental project to test if cGMP is higher in cones expressing mutant Impdh1a. With this work, I was able to provide doubt for this simple hypothesis and provide evidence for new possible disease mechanisms. We generated the first Impdh1a mutant animal models that can be used to address these new hypotheses. This is critical to move the field towards treatment for IMPDH1-related ad-RP or LCA. Overall, in this thesis, I explore how cones remain healthy and the mechanism of why they die when subjected to a metabolic insult.

Bibliography

Acín-Pérez, R., Carrascoso, I., Baixauli, F., Roche-Molina, M., Latorre-Pellicer, A., Fernández-Silva, P., Mittelbrunn, M., Sanchez-Madrid, F., Pérez-Martos, A., Lowell, C.A., Manfredi, G., Enríquez, J.A., 2014. ROS-Triggered Phosphorylation of Complex II by Fgr Kinase Regulates Cellular Adaptation to Fuel Use. Cell Metab. 19, 1020–1033. https://doi.org/10.1016/j.cmet.2014.04.015

Ackrell, B.A.C., Kearney, E.B., Mayr, M., 1974. Role of Oxalacetate in the Regulation of Mammalian Succinate Dehydrogenase. J. Biol. Chem. 249, 2021–2027. https://doi.org/10.1016/S0021-9258(19)42790-7

Adler, A.J., Southwick, R.E., 1992. Distribution of Glucose and Lactate in the Interphotoreceptor Matrix. Ophthalmic Res. 24, 243–252.

Ahangari, N., Munoz, D.G., Coulombe, J., Gray, D.A., Engle, E.C., Cheng, L., Woulfe, J., 2021. Nuclear IMPDH Filaments in Human Gliomas. J. Neuropathol. Exp. Neurol. 80, 944–954. https://doi.org/10.1093/jnen/nlab090

Aherne, A., Kennan, A., Kenna, P.F., McNally, N., Lloyd, D.G., Alberts, I.L., Kiang, A.-S., Humphries, M.M., Ayuso, C., Engel, P.C., Gu, J.J., Mitchell, B.S., Farrar, G.J., Humphries, P., 2004. On the molecular pathology of neurodegeneration in IMPDH1-based retinitis pigmentosa. Hum. Mol. Genet. 13, 641–650. https://doi.org/10.1093/hmg/ddh061

Akimoto, H., Kinumi, T., Ohmiya, Y., 2005. Circadian Rhythm of a TCA Cycle Enzyme Is Apparently Regulated at the Translational Level in the Dinoflagellate Lingulodinium polyedrum. J. Biol. Rhythms 20, 479–489. https://doi.org/10.1177/0748730405280811

Altimus, C.M., Güler, A.D., Alam, N.M., Arman, A.C., Prusky, G.T., Sampath, A.P., Hattar, S., 2010. Rod photoreceptors drive circadian photoentrainment across a wide range of light intensities. Nat. Neurosci. 13, 1107–1112. https://doi.org/10.1038/nn.2617

Ames, A., Li, Y.Y., Heher, E.C., Kimble, C.R., 1992. Energy metabolism of rabbit retina as related to function: high cost of Na+ transport. J. Neurosci. 12, 840–853. https://doi.org/10.1523/JNEUROSCI.12-03-00840.1992

Amiri, M., Hollenbeck, P.J., 2008. Mitochondrial biogenesis in the axons of vertebrate peripheral neurons. Dev. Neurobiol. 68, 1348–1361. https://doi.org/10.1002/dneu.20668

Andersen, B., 1980. Lack of deviation from Michaelis–Menten kinetics for pig heart fumarase. Biochem. J. 189, 653–654. https://doi.org/10.1042/bj1890653

Andrews, R.M., Griffiths, P.G., Johnson, M.A., Turnbull, D.M., 1999. Histochemical localisation of mitochondrial enzyme activity in human optic nerve and retina. Br. J. Ophthalmol. 83, 231–235. https://doi.org/10.1136/bjo.83.2.231

Arshavsky, V.Y., Lamb, T.D., Pugh, E.N., 2002. G proteins and phototransduction. Annu. Rev. Physiol. 64, 153–187. https://doi.org/10.1146/annurev.physiol.64.082701.102229

Artuso, L., Romano, A., Verri, T., Domenichini, A., Argenton, F., Santorelli, F.M., Petruzzella, V., 2012. Mitochondrial DNA metabolism in early development of zebrafish (*Danio rerio*). Biochim. Biophys. Acta BBA - Bioenerg. 1817, 1002–1011. https://doi.org/10.1016/j.bbabio.2012.03.019

Azuma, K., Koumura, T., Iwamoto, R., Matsuoka, M., Terauchi, R., Yasuda, S., Shiraya, T., Watanabe, S., Aihara, M., Imai, H., Ueta, T., 2022. Mitochondrial glutathione peroxidase 4 is indispensable for photoreceptor development and survival in mice. J. Biol. Chem. 298, 101824. https://doi.org/10.1016/j.jbc.2022.101824

Ball, J.M., Chen, S., Li, W., 2022. Mitochondria in cone photoreceptors act as microlenses to enhance photon delivery and confer directional sensitivity to light. Sci. Adv. 8, eabn2070. https://doi.org/10.1126/sciadv.abn2070

Barron, M.J., Johnson, M.A., Andrews, R.M., Clarke, M.P., Griffiths, P.G., Bristow, E., He, L.-P., Durham, S., Turnbull, D.M., 2001. Mitochondrial Abnormalities in Ageing Macular Photoreceptors. Invest. Ophthalmol. Vis. Sci. 42, 3016–3022.

Bennett, L.D., Klein, M., John, F.T., Radojevic, B., Jones, K., Birch, D.G., 2020. Disease Progression in Patients with Autosomal Dominant Retinitis Pigmentosa due to a Mutation in Inosine Monophosphate Dehydrogenase 1 (IMPDH1). Transl. Vis. Sci. Technol. 9, 14. https://doi.org/10.1167/tvst.9.5.14

Bentmann, A., Schmidt, M., Reuss, S., Wolfrum, U., Hankeln, T., Burmester, T., 2005. Divergent Distribution in Vascular and Avascular Mammalian Retinae Links Neuroglobin to Cellular Respiration *. J. Biol. Chem. 280, 20660–20665. https://doi.org/10.1074/jbc.M501338200

Bernardos, R.L., Raymond, P.A., 2006. GFAP transgenic zebrafish. Gene Expr. Patterns 6, 1007–1013. https://doi.org/10.1016/j.modgep.2006.04.006

Bisbach, C.M., Hass, D.T., Robbings, B.M., Rountree, A.M., Sadilek, M., Sweet, I.R., Hurley, J.B., 2020a. Succinate Can Shuttle Reducing Power from the Hypoxic Retina to the O2-Rich Pigment Epithelium. Cell Rep. 31. https://doi.org/10.1016/j.celrep.2020.107606

Bisbach, C.M., Hutto, R.A., Poria, D., Cleghorn, W.M., Abbas, F., Vinberg, F., Kefalov, V.J., Hurley, J.B., Brockerhoff, S.E., 2020b. Mitochondrial Calcium Uniporter (MCU) deficiency reveals an alternate path for Ca2+ uptake in photoreceptor mitochondria. Sci. Rep. 10, 16041. https://doi.org/10.1038/s41598-020-72708-x

Blanchette-Mackie, E.J., Scow, R.O., 1983. Movement of lipolytic products to mitochondria in brown adipose tissue of young rats: an electron microscope study. J. Lipid Res. 24, 229–244. https://doi.org/10.1016/S0022-2275(20)37992-X

Bleck, C.K.E., Kim, Y., Willingham, T.B., Glancy, B., 2018. Subcellular connectomic analyses of energy networks in striated muscle. Nat. Commun. 9, 5111. https://doi.org/10.1038/s41467-018-07676-y

Blume, Z.I., Lambert, J.M., Lovel, A.G., Mitchell, D.M., 2020. Microglia in the developing retina couple phagocytosis with the progression of apoptosis via P2RY12 signaling. Dev. Dyn. 249, 723–740. https://doi.org/10.1002/dvdy.163

Bogovic, J.A., Hanslovsky, P., Wong, A., Saalfeld, S., 2016. Robust registration of calcium images by learned contrast synthesis, in: 2016 IEEE 13th International Symposium on Biomedical Imaging (ISBI). Presented at the 2016 IEEE 13th International Symposium on Biomedical Imaging (ISBI), pp. 1123–1126. https://doi.org/10.1109/ISBI.2016.7493463

Borcherding, N., Brestoff, J.R., 2023. The power and potential of mitochondria transfer. Nature 623, 283–291. https://doi.org/10.1038/s41586-023-06537-z

Brand, M.D., Orr, A.L., Perevoshchikova, I.V., Quinlan, C.L., 2013. The role of mitochondrial function and cellular bioenergetics in ageing and disease. Br. J. Dermatol. 169, 1–8. https://doi.org/10.1111/bjd.12208

Brockerhoff, S.E., 2006. Measuring the optokinetic response of zebrafish larvae. Nat. Protoc. 1, 2448–2451. https://doi.org/10.1038/nprot.2006.255

Brockerhoff, S.E., Hurley, J.B., Janssen-Bienhold, U., Neuhauss, S.C., Driever, W., Dowling, J.E., 1995. A behavioral screen for isolating zebrafish mutants with visual system defects. Proc. Natl. Acad. Sci. 92, 10545–10549. https://doi.org/10.1073/pnas.92.23.10545

Buey, R.M., Ledesma-Amaro, R., Velázquez-Campoy, A., Balsera, M., Chagoyen, M., de Pereda, J.M., Revuelta, J.L., 2015. Guanine nucleotide binding to the Bateman domain mediates the allosteric inhibition of eukaryotic IMP dehydrogenases. Nat. Commun. 6, 8923. https://doi.org/10.1038/ncomms9923

Buj, R., Iglesias, N., Planas, A.M., Santalucía, T., 2013. A plasmid toolkit for cloning chimeric cDNAs encoding customized fusion proteins into any Gateway destination expression vector. BMC Mol. Biol. 14, 18. https://doi.org/10.1186/1471-2199-14-18

Bulina, M.E., Chudakov, D.M., Britanova, O.V., Yanushevich, Y.G., Staroverov, D.B., Chepurnykh, T.V., Merzlyak, E.M., Shkrob, M.A., Lukyanov, S., Lukyanov, K.A., 2006. A genetically encoded photosensitizer. Nat. Biotechnol. 24, 95–99. https://doi.org/10.1038/nbt1175

Burrell, A.L., Kollman, J.M., 2022. IMPDH dysregulation in disease: a mini review. Biochem. Soc. Trans. 50, 71–82. https://doi.org/10.1042/BST20210446

Burrell, A.L., Nie, C., Said, M., Simonet, J.C., Fernández-Justel, D., Johnson, M.C., Quispe, J., Buey, R.M., Peterson, J.R., Kollman, J.M., 2022. IMPDH1 retinal variants control filament architecture to tune allosteric regulation. Nat. Struct. Mol. Biol. 29, 47–58. https://doi.org/10.1038/s41594-021-00706-2

Byrnes, J., Ganetzky, R., Lightfoot, R., Tzeng, M., Nakamaru-Ogiso, E., Seiler, C., Falk, M.J., 2018. Pharmacologic modeling of primary mitochondrial respiratory chain dysfunction in zebrafish. Neurochem. Int., Mitochondria in the Nervous System: From Health to Disease Part 2 117, 23–34. https://doi.org/10.1016/j.neuint.2017.07.008

Cahill, G.M., 2002. Clock mechanisms in zebrafish. Cell Tissue Res. 309, 27–34. https://doi.org/10.1007/s00441-002-0570-7

Cai, T., Hua, B., Luo, D., Xu, L., Cheng, Q., Yuan, G., Yan, Z., Sun, N., Hua, L., Lu, C., 2019. The circadian protein CLOCK regulates cell metabolism via the mitochondrial carrier SLC25A10. Biochim. Biophys. Acta BBA - Mol. Cell Res. 1866, 1310–1321. https://doi.org/10.1016/j.bbamcr.2019.03.016

Calise, S.J., O'Neill, A.G., Burrell, A.L., Dickinson, M.S., Molfino, J., Clarke, C., Quispe, J., Sokolov, D., Buey, R.M., Kollman, J.M., 2024. Light-sensitive phosphorylation regulates retinal

IMPDH1 activity and filament assembly. J. Cell Biol. 223, e202310139. https://doi.org/10.1083/jcb.202310139

Cardona, A., Saalfeld, S., Schindelin, J., Arganda-Carreras, I., Preibisch, S., Longair, M., Tomancak, P., Hartenstein, V., Douglas, R.J., 2012. TrakEM2 Software for Neural Circuit Reconstruction. PLOS ONE 7, e38011. https://doi.org/10.1371/journal.pone.0038011

Carr, S.F., Papp, E., Wu, J.C., Natsumeda, Y., 1993. Characterization of human type I and type II IMP dehydrogenases. J. Biol. Chem. 268, 27286–27290. https://doi.org/10.1016/S0021-9258(19)74247-1

Chan, D.C., 2020. Mitochondrial Dynamics and Its Involvement in Disease. Annu. Rev. Pathol. Mech. Dis. 15, 235–259. https://doi.org/10.1146/annurev-pathmechdis-012419-032711

Chang, C.-C., Keppeke, G.D., Sung, L.-Y., Liu, J.-L., 2018. Interfilament interaction between IMPDH and CTPS cytoophidia. FEBS J. 285, 3753–3768. https://doi.org/10.1111/febs.14624

Chang, J.Y.-A., Shi, L., Ko, M.L., Ko, G.Y.-P., 2018. Circadian Regulation of Mitochondrial Dynamics in Retinal Photoreceptors. J. Biol. Rhythms 33, 151–165. https://doi.org/10.1177/0748730418762152

Chen, H., Chan, D.C., 2009. Mitochondrial dynamics–fusion, fission, movement, and mitophagy–in neurodegenerative diseases. Hum. Mol. Genet. 18, R169–R176. https://doi.org/10.1093/hmg/ddp326

Chen, H., Chomyn, A., Chan, D.C., 2005. Disruption of Fusion Results in Mitochondrial Heterogeneity and Dysfunction *. J. Biol. Chem. 280, 26185–26192. https://doi.org/10.1074/jbc.M503062200

Chi, J., Fan, B., Li, Y., Jiao, Q., Li, G.-Y., 2025. Mitochondrial transplantation: a promising strategy for the treatment of retinal degenerative diseases. Neural Regen. Res. 20, 3370. https://doi.org/10.4103/NRR.NRR-D-24-00851

Chinchore, Y., Begaj, T., Wu, D., Drokhlyansky, E., Cepko, C.L., 2017. Glycolytic reliance promotes anabolism in photoreceptors. eLife 6, e25946. https://doi.org/10.7554/eLife.25946

Chinen, A., Hamaoka, T., Yamada, Y., Kawamura, S., 2003. Gene Duplication and Spectral Diversification of Cone Visual Pigments of Zebrafish. Genetics 163, 663–675. https://doi.org/10.1093/genetics/163.2.663

Cieri, D., Brini, M., Calì, T., 2017. Emerging (and converging) pathways in Parkinson's disease: keeping mitochondrial wellness. Biochem. Biophys. Res. Commun., SI: Neurodegeneration 483, 1020–1030. https://doi.org/10.1016/j.bbrc.2016.08.153

Cimen, H., Han, M.-J., Yang, Y., Tong, Q., Koc, H., Koc, E.C., 2010. Regulation of Succinate Dehydrogenase Activity by SIRT3 in Mammalian Mitochondria. Biochemistry 49, 304–311. https://doi.org/10.1021/bi901627u

Cleghorn, W.M., Brockerhoff, S.E., 2020. Zebrafish in Biomedical Research, in: The Zebrafish in Biomedical Research. Elsevier, pp. 237–244. https://doi.org/10.1016/B978-0-12-812431-4.00021-X

Cleghorn, W.M., Burrell, A.L., Giarmarco, M.M., Brock, D.C., Wang, Y., Chambers, Z.S., Du, J., Kollman, J.M., Brockerhoff, S.E., 2022. A highly conserved zebrafish IMPDH retinal isoform produces the majority of guanine and forms dynamic protein filaments in photoreceptor cells. J. Biol. Chem. 298. https://doi.org/10.1016/j.jbc.2021.101441

Cogliati, S., Enriquez, J.A., Scorrano, L., 2016. Mitochondrial Cristae: Where Beauty Meets Functionality. Trends Biochem. Sci. 41, 261–273. https://doi.org/10.1016/j.tibs.2016.01.001

Confalonieri, F., La Rosa, A., Ottonelli, G., Barone, G., Ferraro, V., Di Maria, A., Romano, M., Randazzo, A., Vallejo-Garcia, J.L., Vinciguerra, P., Petrovski, G., 2024. Retinitis Pigmentosa and Therapeutic Approaches: A Systematic Review. J. Clin. Med. 13, 4680. https://doi.org/10.3390/jcm13164680

Cross, N., van Steen, C., Zegaoui, Y., Satherley, A., Angelillo, L., 2022. Retinitis Pigmentosa: Burden of Disease and Current Unmet Needs. Clin. Ophthalmol. Auckl. NZ 16, 1993–2010. https://doi.org/10.2147/OPTH.S365486

Davis, C.O., Kim, K.-Y., Bushong, E.A., Mills, E.A., Boassa, D., Shih, T., Kinebuchi, M., Phan, S., Zhou, Y., Bihlmeyer, N.A., Nguyen, J.V., Jin, Y., Ellisman, M.H., Marsh-Armstrong, N., 2014. Transcellular degradation of axonal mitochondria. Proc. Natl. Acad. Sci. 111, 9633–9638. https://doi.org/10.1073/pnas.1404651111

Desaulniers, N., Moerland, T.S., Sidell, B.D., 1996. High lipid content enhances the rate of oxygen diffusion through fish skeletal muscle. Am. J. Physiol.-Regul. Integr. Comp. Physiol. 271, R42–R47. https://doi.org/10.1152/ajpregu.1996.271.1.R42

DeVera, C., Tosini, G., 2020. Circadian analysis of the mouse retinal pigment epithelium transcriptome. Exp. Eye Res. 193, 107988. https://doi.org/10.1016/j.exer.2020.107988

Drerup, C.M., Nechiporuk, A.V., 2016. Chapter 15 - In vivo analysis of axonal transport in zebrafish, in: Pfister, K.K. (Ed.), Methods in Cell Biology, The Neuronal Cytoskeleton, Motor Proteins, and Organelle Trafficking in the Axon. Academic Press, pp. 311–329. https://doi.org/10.1016/bs.mcb.2015.06.007

Du, J., Rountree, A., Cleghorn, W.M., Contreras, L., Lindsay, K.J., Sadilek, M., Gu, H., Djukovic, D., Raftery, D., Satrústegui, J., Kanow, M., Chan, L., Tsang, S.H., Sweet, I.R., Hurley, J.B., 2016. Phototransduction Influences Metabolic Flux and Nucleotide Metabolism in Mouse Retina *. J. Biol. Chem. 291, 4698–4710. https://doi.org/10.1074/jbc.M115.698985

Ellett, F., Pase, L., Hayman, J.W., Andrianopoulos, A., Lieschke, G.J., 2011. mpeg1 promoter transgenes direct macrophage-lineage expression in zebrafish. Blood 117, e49–e56. https://doi.org/10.1182/blood-2010-10-314120

Farber, D.B., Lolley, R.N., 1974. Cyclic Guanosine Monophosphate: Elevation in Degenerating Photoreceptor Cells of the C3H Mouse Retina. Science 186, 449–451. https://doi.org/10.1126/science.186.4162.449

Fernández-Justel, D., Núñez, R., Martín-Benito, J., Jimeno, D., González-López, A., Soriano, E.M., Revuelta, J.L., Buey, R.M., 2019a. A Nucleotide-Dependent Conformational Switch Controls the Polymerization of Human IMP Dehydrogenases to Modulate their Catalytic Activity. J. Mol. Biol. 431, 956–969. https://doi.org/10.1016/j.jmb.2019.01.020

Fernández-Justel, D., Peláez, R., Revuelta, J.L., Buey, R.M., 2019b. The Bateman domain of IMP dehydrogenase is a binding target for dinucleoside polyphosphates. J. Biol. Chem. 294, 14768–14775. https://doi.org/10.1074/jbc.AC119.010055

Fivenson, E.M., Lautrup, S., Sun, N., Scheibye-Knudsen, M., Stevnsner, T., Nilsen, H., Bohr, V.A., Fang, E.F., 2017. Mitophagy in neurodegeneration and aging. Neurochem. Int., Mitochondria in the Nervous System: From Health to Disease 109, 202–209. https://doi.org/10.1016/j.neuint.2017.02.007

Fowler, D.K., Stewart, S., Seredick, S., Eisen, J.S., Stankunas, K., Washbourne, P., 2016. A MultiSite Gateway Toolkit for Rapid Cloning of Vertebrate Expression Constructs with Diverse Research Applications. PLOS ONE 11, e0159277. https://doi.org/10.1371/journal.pone.0159277

Friedman, J.R., Lackner, L.L., West, M., DiBenedetto, J.R., Nunnari, J., Voeltz, G.K., 2011. ER Tubules Mark Sites of Mitochondrial Division. Science 334, 358–362. https://doi.org/10.1126/science.1207385

Gasko, O., Danon, D., 1972. Deterioration and disappearance of mitochondria during reticulocyte maturation. Exp. Cell Res. 75, 159–169. https://doi.org/10.1016/0014-4827(72)90532-0

Géminard, C., De Gassart, A., Vidal, M., 2002. Review : Reticulocyte maturation: mitoptosis and exosome release. Biocell 26, 205–215.

George, A.A., Hayden, S., Holzhausen, L.C., Ma, E.Y., Suzuki, S.C., Brockerhoff, S.E., 2014. Synaptojanin 1 Is Required for Endolysosomal Trafficking of Synaptic Proteins in Cone Photoreceptor Inner Segments. PLOS ONE 9, e84394. https://doi.org/10.1371/journal.pone.0084394

George, A.A., Hayden, S., Stanton, G.R., Brockerhoff, S.E., 2016. Arf6 and the 5'phosphatase of synaptojanin 1 regulate autophagy in cone photoreceptors. BioEssays 38, S119–S135. https://doi.org/10.1002/bies.201670913

Gerdes, H.-H., Carvalho, R.N., 2008. Intercellular transfer mediated by tunneling nanotubes. Curr. Opin. Cell Biol. 20, 470–475. https://doi.org/10.1016/j.ceb.2008.03.005

Giarmarco, M., Seto, J., Brock, D., Brockerhoff, S., 2024. Spatial detection of mitochondrial DNA and RNA in tissues. Front. Cell Dev. Biol. 12. https://doi.org/10.3389/fcell.2024.1346778

Giarmarco, M.M., Brock, D.C., Robbings, B.M., Cleghorn, W.M., Tsantilas, K.A., Kuch, K.C., Ge, W., Rutter, K.M., Parker, E.D., Hurley, J.B., Brockerhoff, S.E., 2020. Daily mitochondrial dynamics in cone photoreceptors. Proc. Natl. Acad. Sci. 117, 28816–28827. https://doi.org/10.1073/pnas.2007827117

Giarmarco, M.M., Cleghorn, W.M., Hurley, J.B., Brockerhoff, S.E., 2018. Preparing Fresh Retinal Slices from Adult Zebrafish for Ex Vivo Imaging Experiments. J. Vis. Exp. JoVE 56977. https://doi.org/10.3791/56977

Giarmarco, M.M., Cleghorn, W.M., Sloat, S.R., Hurley, J.B., Brockerhoff, S.E., 2017. Mitochondria Maintain Distinct Ca2+ Pools in Cone Photoreceptors. J. Neurosci. 37, 2061–2072. https://doi.org/10.1523/JNEUROSCI.2689-16.2017

Goede, P. de, Wefers, J., Brombacher, E.C., Schrauwen, P., Kalsbeek, A., 2018. Circadian rhythms in mitochondrial respiration. https://doi.org/10.1530/JME-17-0196

Gu, F., Chen, L., Ni, B., Zhang, X., 2002. A comparative study on the electron microscopic enzymo-cytochemistry of *Paramecium bursaria* from light and dark cultures. Eur. J. Protistol. 38, 267–278. https://doi.org/10.1078/0932-4739-00875

Guo, R., Gu, J., Zong, S., Wu, M., Yang, M., 2018. Structure and mechanism of mitochondrial electron transport chain. Biomed. J. 41, 9–20. https://doi.org/10.1016/j.bj.2017.12.001

Hamasaki, M., Furuta, N., Matsuda, A., Nezu, A., Yamamoto, A., Fujita, N., Oomori, H., Noda, T., Haraguchi, T., Hiraoka, Y., Amano, A., Yoshimori, T., 2013. Autophagosomes form at ER–mitochondria contact sites. Nature 495, 389–393. https://doi.org/10.1038/nature11910

Hayakawa, K., Esposito, E., Wang, X., Terasaki, Y., Liu, Y., Xing, C., Ji, X., Lo, E.H., 2016. Transfer of mitochondria from astrocytes to neurons after stroke. Nature 535, 551–555. https://doi.org/10.1038/nature18928

Hoang, Q.V., Linsenmeier, R.A., Chung, C.K., Curcio, C.A., 2002. Photoreceptor inner segments in monkey and human retina: Mitochondrial density, optics, and regional variation. Vis. Neurosci. 19, 395–407. https://doi.org/10.1017/S0952523802194028

Hodel, C., Neuhauss, S.C.F., Biehlmaier, O., 2006. Time course and development of light adaptation processes in the outer zebrafish retina. Anat. Rec. A. Discov. Mol. Cell. Evol. Biol. 288A, 653–662. https://doi.org/10.1002/ar.a.20329

Hollyfield, J.G., 1999. Hyaluronan and the Functional Organization of the Interphotoreceptor Matrix. Invest. Ophthalmol. Vis. Sci. 40, 2767–2769.

Hollyfield, J.G., Rayborn, M.E., 1987. Endocytosis in the inner segment of rod photoreceptors: Analysis of *Xenopus laevis* retinas using horseradish peroxidase. Exp. Eye Res. 45, 703–719. https://doi.org/10.1016/S0014-4835(87)80119-7

Hollyfield, J.G., Varner, H.H., Rayborn, M.E., Liou, G.I., Bridges, C.D., 1985. Endocytosis and degradation of interstitial retinol-binding protein: differential capabilities of cells that border the interphotoreceptor matrix. J. Cell Biol. 100, 1676–1681. https://doi.org/10.1083/jcb.100.5.1676

Huang, C.-H., Yang, C.-M., Yang, C.-H., Hou, Y.-C., Chen, T.-C., 2021. Leber's Congenital Amaurosis: Current Concepts of Genotype-Phenotype Correlations. Genes 12, 1261. https://doi.org/10.3390/genes12081261

Huang, Y., Yang, P., Chen, H., Bai, X., Wang, X., Vistro, W.A., Haseeb, A., Shi, Y., Chen, Q., 2018. A "Lamellar structure" contributes to autophagosome biogenesis and mitophagy in zebrafish hepatocytes. Fish Shellfish Immunol. 81, 83–91. https://doi.org/10.1016/j.fsi.2018.06.044

Hurley, J.B., 2021. Retina Metabolism and Metabolism in the Pigmented Epithelium: A Busy Intersection. Annu. Rev. Vis. Sci. 7, 665–692. https://doi.org/10.1146/annurev-vision-100419-115156

Hutto, R.A., Bisbach, C.M., Abbas, F., Brock, D.C., Cleghorn, W.M., Parker, E.D., Bauer, B.H., Ge, W., Vinberg, F., Hurley, J.B., Brockerhoff, S.E., 2020. Increasing Ca2+ in photoreceptor mitochondria alters metabolites, accelerates photoresponse recovery, and reveals adaptations to mitochondrial stress. Cell Death Differ. 27, 1067–1085. https://doi.org/10.1038/s41418-019-0398-2

Indira, D., Varadarajan, S.N., Subhasingh Lupitha, S., Lekshmi, A., Mathew, K.A., Chandrasekharan, A., Rajappan Pillai, P., Pulikkal Kadamberi, I., Ramachandran, I., Sekar, H., Kochucherukkan Gopalakrishnan, A., Tr, S., 2018. Strategies for imaging mitophagy in high-resolution and high-throughput. Eur. J. Cell Biol. 97, 1–14. https://doi.org/10.1016/j.ejcb.2017.10.003

Ingram, N.T., Fain, G.L., Sampath, A.P., 2020. Elevated energy requirement of cone photoreceptors. Proc. Natl. Acad. Sci. 117, 19599–19603. https://doi.org/10.1073/pnas.2001776117

Iribarne, M., Masai, I., 2018. Do cGMP Levels Drive the Speed of Photoreceptor Degeneration?, in: Ash, J.D., Anderson, R.E., LaVail, M.M., Bowes Rickman, C., Hollyfield, J.G., Grimm, C. (Eds.), Retinal Degenerative Diseases. Springer International Publishing, Cham, pp. 327–333. https://doi.org/10.1007/978-3-319-75402-4_40

Ishikawa, M., Sawada, Y., Yoshitomi, T., 2015. Structure and function of the interphotoreceptor matrix surrounding retinal photoreceptor cells. Exp. Eye Res., Ocular extracellular matrix: Role in development, homeostasis and disease 133, 3–18. https://doi.org/10.1016/j.exer.2015.02.017

ISHIKAWA, T., YAMADA, E., 1969. Atypical Mitochondria in the Ellipsoid of the Photoreceptor Cells of Vertebrate Retinas. Invest. Ophthalmol. Vis. Sci. 8, 302–316.

Jackson, R.C., Weber, G., Morris, H.P., 1975. IMP dehydrogenase, an enzyme linked with proliferation and malignancy. Nature 256, 331–333. https://doi.org/10.1038/256331a0

Januschka, M.M., Burkhardt, D.A., Erlandsen, S.L., Purple, R.L., 1987. The ultrastructure of cones in the walleye retina. Vision Res. 27, 327–341. https://doi.org/10.1016/0042-6989(87)90082-4

Johnson, L.V., Hageman, G.S., Blanks, J.C., 1986. Interphotoreceptor matrix domains ensheath vertebrate cone photoreceptor cells. Invest. Ophthalmol. Vis. Sci. 27, 129–135.

Johnson, M.C., Kollman, J.M., 2020. Cryo-EM structures demonstrate human IMPDH2 filament assembly tunes allosteric regulation. eLife 9, e53243. https://doi.org/10.7554/eLife.53243

Kam, J.H., Weinrich, T.W., Sangha, H., Powner, M.B., Fosbury, R., Jeffery, G., 2019. Mitochondrial absorption of short wavelength light drives primate blue retinal cones into glycolysis which may increase their pace of aging. Vis. Neurosci. 36, E007. https://doi.org/10.1017/S0952523819000063

Kanow, M.A., Giarmarco, M.M., Jankowski, C.S., Tsantilas, K., Engel, A.L., Du, J., Linton, J.D., Farnsworth, C.C., Sloat, S.R., Rountree, A., Sweet, I.R., Lindsay, K.J., Parker, E.D.,

Brockerhoff, S.E., Sadilek, M., Chao, J.R., Hurley, J.B., 2017. Biochemical adaptations of the retina and retinal pigment epithelium support a metabolic ecosystem in the vertebrate eye. eLife 6, e28899. https://doi.org/10.7554/eLife.28899

Karlsson, M., Zhang, C., Méar, L., Zhong, W., Digre, A., Katona, B., Sjöstedt, E., Butler, L., Odeberg, J., Dusart, P., Edfors, F., Oksvold, P., von Feilitzen, K., Zwahlen, M., Arif, M., Altay, O., Li, X., Ozcan, M., Mardinoglu, A., Fagerberg, L., Mulder, J., Luo, Y., Ponten, F., Uhlén, M., Lindskog, C., 2021. A single–cell type transcriptomics map of human tissues. Sci. Adv. 7, eabh2169. https://doi.org/10.1126/sciadv.abh2169

Katayama, H., Hama, H., Nagasawa, K., Kurokawa, H., Sugiyama, M., Ando, R., Funata, M., Yoshida, N., Homma, M., Nishimura, T., Takahashi, M., Ishida, Y., Hioki, H., Tsujihata, Y., Miyawaki, A., 2020. Visualizing and Modulating Mitophagy for Therapeutic Studies of Neurodegeneration. Cell 181, 1176-1187.e16. https://doi.org/10.1016/j.cell.2020.04.025

Kawajiri, S., Saiki, S., Sato, S., Sato, F., Hatano, T., Eguchi, H., Hattori, N., 2010. PINK1 is recruited to mitochondria with parkin and associates with LC3 in mitophagy. FEBS Lett. 584, 1073–1079. https://doi.org/10.1016/j.febslet.2010.02.016

Kennedy, B.N., Alvarez, Y., Brockerhoff, S.E., Stearns, G.W., Sapetto-Rebow, B., Taylor, M.R., Hurley, J.B., 2007. Identification of a Zebrafish Cone Photoreceptor–Specific Promoter and Genetic Rescue of Achromatopsia in the nof Mutant. Invest. Ophthalmol. Vis. Sci. 48, 522–529. https://doi.org/10.1167/iovs.06-0975

Kim, J., Lee, E., Chang, B.S., Oh, C.S., Mun, G.-H., Chung, Y.H., Shin, D.H., 2005. The Presence of Megamitochondria in the Ellipsoid of Photoreceptor Inner Segment of the Zebrafish Retina. Anat. Histol. Embryol. 34, 339–342. https://doi.org/10.1111/j.1439-0264.2005.00612.x

Knabe, W., Kuhn, H.-J., 1996. Morphogenesis of megamitochondria in the retinal cone inner segments of Tupaia belangeri (Scandentia). Cell Tissue Res. 285, 1–9. https://doi.org/10.1007/s004410050614

Knabe, W., Skatchkov, S., Kuhn, H.-J., 1997. “Lens Mitochondria” in the Retinal Cones of the Tree-shrew Tupaia belangeri. Vision Res. 37, 267–271. https://doi.org/10.1016/S0042-6989(96)00199-X

Korobova, F., Ramabhadran, V., Higgs, H.N., 2013. An Actin-Dependent Step in Mitochondrial Fission Mediated by the ER-Associated Formin INF2. Science 339, 464–467. https://doi.org/10.1126/science.1228360

Korzh, V., Teh, C., Kondrychyn, I., Chudakov, D.M., Lukyanov, S., 2011. Visualizing Compound Transgenic Zebrafish in Development: A Tale of Green Fluorescent Protein and KillerRed. Zebrafish 8, 23–29. https://doi.org/10.1089/zeb.2011.0689

Kozhevnikova, E.N., van der Knaap, J.A., Pindyurin, A.V., Ozgur, Z., van Ijcken, W.F.J., Moshkin, Y.M., Verrijzer, C.P., 2012. Metabolic Enzyme IMPDH Is Also a Transcription Factor Regulated by Cellular State. Mol. Cell 47, 133–139. https://doi.org/10.1016/j.molcel.2012.04.030

Laar, V.S.V., Arnold, B., Howlett, E.H., Calderon, M.J., Croix, C.M.S., Greenamyre, J.T., Sanders, L.H., Berman, S.B., 2018. Evidence for Compartmentalized Axonal Mitochondrial Biogenesis: Mitochondrial DNA Replication Increases in Distal Axons As an Early Response to Parkinson’s Disease-Relevant Stress. J. Neurosci. 38, 7505–7515. https://doi.org/10.1523/JNEUROSCI.0541-18.2018

Lampinen, R., Belaya, I., Saveleva, L., Liddell, J.R., Rait, D., Huuskonen, M.T., Giniatullina, R., Sorvari, A., Soppela, L., Mikhailov, N., Boccuni, I., Giniatullin, R., Cruz-Haces, M., Konovalova, J., Koskuvi, M., Domanskyi, A., Hämäläinen, R.H., Goldsteins, G., Koistinaho, J., Malm, T., Chew, S., Rilla, K., White, A.R., Marsh-Armstrong, N., Kanninen, K.M., 2022.

Neuron-astrocyte transmitophagy is altered in Alzheimer's disease. Neurobiol. Dis. 170, 105753. https://doi.org/10.1016/j.nbd.2022.105753

Larison, K.D., Bremiller, R., 1990. Early onset of phenotype and cell patterning in the embryonic zebrafish retina. Development 109, 567–576. https://doi.org/10.1242/dev.109.3.567

LaVail, M.M., 1976. Rod Outer Segment Disk Shedding in Rat Retina: Relationship to Cyclic Lighting. Science 194, 1071–1074. https://doi.org/10.1126/science.982063

LaVail, M.M., Gorrin, G.M., Repaci, M.A., Thomas, L.A., Ginsberg, H.M., 1987. Genetic regulation of light damage to photoreceptors. Invest. Ophthalmol. Vis. Sci. 28, 1043–1048.

Lefevere, E., Toft-Kehler, A.K., Vohra, R., Kolko, M., Moons, L., Van Hove, I., 2017. Mitochondrial dysfunction underlying outer retinal diseases. Mitochondrion, Mitochondria and the eye diseases 36, 66–76. https://doi.org/10.1016/j.mito.2017.03.006

Lem, J., Krasnoperova, N.V., Calvert, P.D., Kosaras, B., Cameron, D.A., Nicolò, M., Makino, C.L., Sidman, R.L., 1999. Morphological, physiological, and biochemical changes in rhodopsin knockout mice. Proc. Natl. Acad. Sci. 96, 736–741. https://doi.org/10.1073/pnas.96.2.736

Li, L., Dowling, J.E., 1998. Zebrafish visual sensitivity is regulated by a circadian clock. Vis. Neurosci. 15, 851–857. https://doi.org/10.1017/S0952523898155050

Li, P., Chaurasia, S.S., Gao, Y., Carr, A.L., Iuvone, P.M., Li, L., 2008. CLOCK Is Required for Maintaining the Circadian Rhythms of Opsin mRNA Expression in Photoreceptor Cells *. J. Biol. Chem. 283, 31673–31678. https://doi.org/10.1074/jbc.M803875200

Lin, J.B., Kubota, S., Ban, N., Yoshida, M., Santeford, A., Sene, A., Nakamura, R., Zapata, N., Kubota, M., Tsubota, K., Yoshino, J., Imai, S., Apte, R.S., 2016. NAMPT-Mediated NAD+ Biosynthesis Is Essential for Vision In Mice. Cell Rep. 17, 69–85. https://doi.org/10.1016/j.celrep.2016.08.073

Litts, K.M., Messinger, J.D., Freund, K.B., Zhang, Y., Curcio, C.A., 2015. Inner Segment Remodeling and Mitochondrial Translocation in Cone Photoreceptors in Age-Related Macular Degeneration With Outer Retinal Tubulation. Invest. Ophthalmol. Vis. Sci. 56, 2243–2253. https://doi.org/10.1167/iovs.14-15838

Liu, D., Gao, Y., Liu, J., Huang, Y., Yin, J., Feng, Y., Shi, L., Meloni, B.P., Zhang, C., Zheng, M., Gao, J., 2021. Intercellular mitochondrial transfer as a means of tissue revitalization. Signal Transduct. Target. Ther. 6, 1–18. https://doi.org/10.1038/s41392-020-00440-z

Liu, F., Lössl, P., Rabbitts, B.M., Balaban, R.S., Heck, A.J.R., 2018. The interactome of intact mitochondria by cross-linking mass spectrometry provides evidence for coexisting respiratory supercomplexes*. Mol. Cell. Proteomics 17, 216–232. https://doi.org/10.1074/mcp.RA117.000470

Lluch, S., López-Fuster, M.J., Ventura, J., 2003. Giant mitochondria in the retina cone inner segments of shrews of genus Sorex (Insectivora, Soricidae). Anat. Rec. A. Discov. Mol. Cell. Evol. Biol. 272A, 484–490. https://doi.org/10.1002/ar.a.10066

Lu, J., Zheng, X., Li, F., Yu, Y., Chen, Z., Liu, Z., Wang, Z., Xu, H., Yang, W., 2017. Tunneling nanotubes promote intercellular mitochondria transfer followed by increased invasiveness in bladder cancer cells. Oncotarget 8, 15539–15552. https://doi.org/10.18632/oncotarget.14695

Lyamzaev, K.G., Nepryakhina, O.K., Saprunova, V.B., Bakeeva, L.E., Pletjushkina, O.Yu., Chernyak, B.V., Skulachev, V.P., 2008. Novel mechanism of elimination of malfunctioning mitochondria (mitoptosis): Formation of mitoptotic bodies and extrusion of mitochondrial material from the cell. Biochim. Biophys. Acta BBA - Bioenerg., 15th European Bioenergetics Conference 2008 1777, 817–825. https://doi.org/10.1016/j.bbabio.2008.03.027

MacNichol, E.F., Kunz, Y.W., Levine, J.S., Hárosi, F.I., Collins, B.A., 1978. Ellipsosomes: Organelles Containing a Cytochrome-Like Pigment in the Retinal Cones of Certain Fishes. Science 200, 549–552. https://doi.org/10.1126/science.644317

Maryanovich, M., Zaltsman, Y., Ruggiero, A., Goldman, A., Shachnai, L., Zaidman, S.L., Porat, Z., Golan, K., Lapidot, T., Gross, A., 2015. An MTCH2 pathway repressing mitochondria metabolism regulates haematopoietic stem cell fate. Nat. Commun. 6, 7901. https://doi.org/10.1038/ncomms8901

Masuda, T., Wada, Y., Kawamura, S., 2016. ES1 is a mitochondrial enlarging factor contributing to form mega-mitochondria in zebrafish cones. Sci. Rep. 6, 22360. https://doi.org/10.1038/srep22360

Melentijevic, I., Toth, M.L., Arnold, M.L., Guasp, R.J., Harinath, G., Nguyen, K.C., Taub, D., Parker, J.A., Neri, C., Gabel, C.V., Hall, D.H., Driscoll, M., 2017. C. elegans neurons jettison protein aggregates and mitochondria under neurotoxic stress. Nature 542, 367–371. https://doi.org/10.1038/nature21362

Menger, G.J., Koke, J.R., Cahill, G.M., 2005. Diurnal and circadian retinomotor movements in zebrafish. Vis. Neurosci. 22, 203–209. https://doi.org/10.1017/S0952523805222083

Mercurio, A.M., Holtzman, E., 1982. Smooth endoplasmic reticulum and other agranular reticulum in frog retinal photoreceptors. J. Neurocytol. 11, 263–293. https://doi.org/10.1007/BF01258247

Millard, P., Letisse, F., Sokol, S., Portais, J.-C., 2012. IsoCor: correcting MS data in isotope labeling experiments. Bioinformatics 28, 1294–1296. https://doi.org/10.1093/bioinformatics/bts127

Moore, C.L., Gruberg, E.R., 1974. The distribution of succinic semialdehyde dehydrogenase in the brain and retina of the tiger salamander (*Ambystoma tigrinum*). Brain Res. 67, 467–478. https://doi.org/10.1016/0006-8993(74)90495-8

Morales, I., Sanchez, A., Puertas-Avendaño, R., Rodriguez-Sabate, C., Perez-Barreto, A., Rodriguez, M., 2020. Neuroglial transmitophagy and Parkinson's disease. Glia 68, 2277–2299. https://doi.org/10.1002/glia.23839

Mortimer, S.E., Hedstrom, L., 2005. Autosomal dominant retinitis pigmentosa mutations in inosine 5'-monophosphate dehydrogenase type I disrupt nucleic acid binding. Biochem. J. 390, 41–47. https://doi.org/10.1042/BJ20042051

Mortimer, S.E., Xu, D., McGrew, D., Hamaguchi, N., Lim, H.C., Bowne, S.J., Daiger, S.P., Hedstrom, L., 2008. IMP Dehydrogenase Type 1 Associates with Polyribosomes Translating Rhodopsin mRNA *. J. Biol. Chem. 283, 36354–36360. https://doi.org/10.1074/jbc.M806143200

Mrosovsky, N., Foster, R.G., Salmon, P.A., 1999. Thresholds for masking responses to light in three strains of retinally degenerate mice. J. Comp. Physiol. A 184, 423–428. https://doi.org/10.1007/s003590050341

Nag, T.C., Bhattacharjee, J., 1995. Retinal ellipsosomes: morphology, development, identification, and comparison with oil droplets. Cell Tissue Res. 279, 633–637. https://doi.org/10.1007/BF00318176

Nag, T.C., Wadhwa, S., 2016. Immunolocalisation pattern of complex I–V in ageing human retina: Correlation with mitochondrial ultrastructure. Mitochondrion 31, 20–32. https://doi.org/10.1016/j.mito.2016.08.016

Nath, A.K., Ryu, J.H., Jin, Y.N., Roberts, L.D., Dejam, A., Gerszten, R.E., Peterson, R.T., 2015. PTPMT1 Inhibition Lowers Glucose through Succinate Dehydrogenase Phosphorylation. Cell Rep. 10, 694–701. https://doi.org/10.1016/j.celrep.2015.01.010

Nork, T.M., McCormick, S.A., Chao, G.M., Odom, J.V., 1990. Distribution of carbonic anhydrase among human photoreceptors. Invest. Ophthalmol. Vis. Sci. 31, 1451–1458.

Okawa, H., Sampath, A.P., Laughlin, S.B., Fain, G.L., 2008. ATP Consumption by Mammalian Rod Photoreceptors in Darkness and in Light. Curr. Biol. 18, 1917–1921. https://doi.org/10.1016/j.cub.2008.10.029

Ortin-Martinez, A., Tsai, E.L.S., Nickerson, P.E., Bergeret, M., Lu, Y., Smiley, S., Comanita, L., Wallace, V.A., 2017. A Reinterpretation of Cell Transplantation: GFP Transfer From Donor to Host Photoreceptors. Stem Cells 35, 932–939. https://doi.org/10.1002/stem.2552

OSF | Giarmarco_PNAS_2020_rawdata.zip [WWW Document], n.d. URL https://osf.io/qaed8 (accessed 3.28.25).

Palczewski, K., Kiser, P.D., 2020. Shedding new light on the generation of the visual chromophore. Proc. Natl. Acad. Sci. 117, 19629–19638. https://doi.org/10.1073/pnas.2008211117

Park, J., Chen, Y., Tishkoff, D.X., Peng, C., Tan, M., Dai, L., Xie, Z., Zhang, Y., Zwaans, B.M.M., Skinner, M.E., Lombard, D.B., Zhao, Y., 2013. SIRT5-Mediated Lysine Desuccinylation Impacts Diverse Metabolic Pathways. Mol. Cell 50, 919–930. https://doi.org/10.1016/j.molcel.2013.06.001

Pedley, A.M., Benkovic, S.J., 2017. A New View into the Regulation of Purine Metabolism: The Purinosome. Trends Biochem. Sci. 42, 141–154. https://doi.org/10.1016/j.tibs.2016.09.009

Perkins, G.A., Ellisman, M.H., Fox, D.A., 2003. Three-dimensional analysis of mouse rod and cone mitochondrial cristae architecture: Bioenergetic and functional implications. Mol. Vis.

Peshenko, I.V., Olshevskaya, E.V., Savchenko, A.B., Karan, S., Palczewski, K., Baehr, W., Dizhoor, A.M., 2011. Enzymatic Properties and Regulation of the Native Isozymes of Retinal Membrane Guanylyl Cyclase (RetGC) from Mouse Photoreceptors. Biochemistry 50, 5590–5600. https://doi.org/10.1021/bi200491b

Plana-Bonamaisó, A., López-Begines, S., Fernández-Justel, D., Junza, A., Soler-Tapia, A., Andilla, J., Loza-Alvarez, P., Rosa, J.L., Miralles, E., Casals, I., Yanes, O., de la Villa, P., Buey, R.M.,

Méndez, A., 2020. Post-translational regulation of retinal IMPDH1 in vivo to adjust GTP synthesis to illumination conditions. eLife 9, e56418. https://doi.org/10.7554/eLife.56418

Ploumi, C., Daskalaki, I., Tavernarakis, N., 2017. Mitochondrial biogenesis and clearance: a balancing act. FEBS J. 284, 183–195. https://doi.org/10.1111/febs.13820

Popov, V.N., Eprintsev, A.T., Fedorin, D.N., Igamberdiev, A.U., 2010. Succinate dehydrogenase in *Arabidopsis thaliana* is regulated by light via phytochrome A. FEBS Lett. 584, 199–202. https://doi.org/10.1016/j.febslet.2009.11.057

Potter, V.R., DuBois, K.P., 1943. STUDIES ON THE MECHANISM OF HYDROGEN TRANSPORT IN ANIMAL TISSUES. J. Gen. Physiol. 26, 391–404.

Power, M., Das, S., Schütze, K., Marigo, V., Ekström, P., Paquet-Durand, F., 2020. Cellular mechanisms of hereditary photoreceptor degeneration – Focus on cGMP. Prog. Retin. Eye Res. 74, 100772. https://doi.org/10.1016/j.preteyeres.2019.07.005

Raymond, P.A., Barthel, L.K., Curran, G.A., 1995. Developmental patterning of rod and cone photoreceptors in embryonic zebrafish. J. Comp. Neurol. 359, 537–550. https://doi.org/10.1002/cne.903590403

Raymond, P.A., Colvin, S.M., Jabeen, Z., Nagashima, M., Barthel, L.K., Hadidjojo, J., Popova, L., Pejaver, V.R., Lubensky, D.K., 2014. Patterning the Cone Mosaic Array in Zebrafish Retina Requires Specification of Ultraviolet-Sensitive Cones. PLOS ONE 9, e85325. https://doi.org/10.1371/journal.pone.0085325

Rea, R., Li, J., Dharia, A., Levitan, E.S., Sterling, P., Kramer, R.H., 2004. Streamlined Synaptic Vesicle Cycle in Cone Photoreceptor Terminals. Neuron 41, 755–766. https://doi.org/10.1016/S0896-6273(04)00088-1

Reddy, A.B., Karp, N.A., Maywood, E.S., Sage, E.A., Deery, M., O'Neill, J.S., Wong, G.K.Y., Chesham, J., Odell, M., Lilley, K.S., Kyriacou, C.P., Hastings, M.H., 2006. Circadian Orchestration of the Hepatic Proteome. Curr. Biol. 16, 1107–1115. https://doi.org/10.1016/j.cub.2006.04.026

Reichenbach, A., Robinson, S.R., 1995. The involvement of Müller cells in the outer retina, in: Djamgoz, M.B.A., Archer, S.N., Vallerga, S. (Eds.), Neurobiology and Clinical Aspects of the Outer Retina. Springer Netherlands, Dordrecht, pp. 395–416. https://doi.org/10.1007/978-94-011-0533-0_16

RetNet - Retinal Information Network [WWW Document], n.d. URL https://retnet.org/ (accessed 3.28.25).

Rodríguez-Muela, N., Hernández-Pinto, A.M., Serrano-Puebla, A., García-Ledo, L., Latorre, S.H., de la Rosa, E.J., Boya, P., 2015. Lysosomal membrane permeabilization and autophagy blockade contribute to photoreceptor cell death in a mouse model of retinitis pigmentosa. Cell Death Differ. 22, 476–487. https://doi.org/10.1038/cdd.2014.203

Rosina, M., Ceci, V., Turchi, R., Li, C., Borcherding, N., Sciarretta, F., Sánchez-Díaz, M., Tortolici, F., Karlinsey, K., Chiurchiù, V., Fuoco, C., Giwa, R., Field, R.L., Audano, M., Arena, S., Palma, A., Riccio, F., Shamsi, F., Renzone, G., Verri, M., Crescenzi, A., Rizza, S., Faienza, F., Filomeni, G., Kooijman, S., Rufini, S., Vries, A.A.F. de, Scaloni, A., Mitro, N., Tseng, Y.-H., Hidalgo, A., Zhou, B., Brestoff, J.R., Aquilano, K., Lettieri-Barbato, D., 2022. Ejection of damaged mitochondria and their removal by macrophages ensure efficient thermogenesis in brown adipose tissue. Cell Metab. 34, 533-548.e12. https://doi.org/10.1016/j.cmet.2022.02.016

Saalfeld, S., Cardona, A., Hartenstein, V., Tomančák, P., 2010. As-rigid-as-possible mosaicking and serial section registration of large ssTEM datasets. Bioinformatics 26, i57–i63. https://doi.org/10.1093/bioinformatics/btq219

Saalfeld, S., Fetter, R., Cardona, A., Tomancak, P., 2012. Elastic volume reconstruction from series of ultra-thin microscopy sections. Nat. Methods 9, 717–720. https://doi.org/10.1038/nmeth.2072

Sajdak, B.S., Salmon, A.E., Litts, K.M., Wells, C., Allen, K.P., Dubra, A., Merriman, D.K., Carroll, J., 2019. Evaluating seasonal changes of cone photoreceptor structure in the 13-lined ground squirrel. Vision Res. 158, 90–99. https://doi.org/10.1016/j.visres.2019.02.009

Sakti, D.H., Cornish, E.E., Nash, B.M., Jamieson, R.V., Grigg, J.R., 2023. IMPDH1-associated autosomal dominant retinitis pigmentosa: natural history of novel variant Lys314Gln and a comprehensive literature search. Ophthalmic Genet. 44, 437–455. https://doi.org/10.1080/13816810.2023.2215310

Samuvel, D.J., Li ,Li, Krishnasamy ,Yasodha, Gooz ,Monika, Takemoto ,Kenji, Woster ,Patrick M., Lemasters ,John J., and Zhong, Z., 2022. Mitochondrial depolarization after acute ethanol treatment drives mitophagy in living mice. Autophagy 18, 2671–2685. https://doi.org/10.1080/15548627.2022.2046457

Saravanan, M., Xu, R., Roby, O., Wang, Y., Zhu, S., Lu, A., Du, J., 2023. Tissue-Specific Sex Difference in Mouse Eye and Brain Metabolome Under Fed and Fasted States. Invest. Ophthalmol. Vis. Sci. 64, 18. https://doi.org/10.1167/iovs.64.3.18

Sartori-Rupp, A., Cordero Cervantes, D., Pepe, A., Gousset, K., Delage, E., Corroyer-Dulmont, S., Schmitt, C., Krijnse-Locker, J., Zurzolo, C., 2019. Correlative cryo-electron microscopy reveals the structure of TNTs in neuronal cells. Nat. Commun. 10, 342. https://doi.org/10.1038/s41467-018-08178-7

Scarpulla, R.C., Vega, R.B., Kelly, D.P., 2012. Transcriptional integration of mitochondrial biogenesis. Trends Endocrinol. Metab. 23, 459–466. https://doi.org/10.1016/j.tem.2012.06.006

Schindelin, J., Arganda-Carreras, I., Frise, E., Kaynig, V., Longair, M., Pietzsch, T., Preibisch, S., Rueden, C., Saalfeld, S., Schmid, B., Tinevez, J.-Y., White, D.J., Hartenstein, V., Eliceiri, K., Tomancak, P., Cardona, A., 2012. Fiji: an open-source platform for biological-image analysis. Nat. Methods 9, 676–682. https://doi.org/10.1038/nmeth.2019

Senda, M., Natsumeda, Y., 1994. Tissue-differential expression of two distinct genes for human IMP dehydrogenase (E.C.1.1.1.205). Life Sci. 54, 1917–1926. https://doi.org/10.1016/0024-3205(94)90150-3

Shichino, Y., Iwasaki, S., 2022. Compounds for selective translational inhibition. Curr. Opin. Chem. Biol. 69, 102158. https://doi.org/10.1016/j.cbpa.2022.102158

Shin, J., Chen, J., Solnica-Krezel, L., 2014. Efficient homologous recombination-mediated genome engineering in zebrafish using TALE nucleases. Development 141, 3807–3818. https://doi.org/10.1242/dev.108019

Simpson, C.F., Kling, J.M., 1968. THE MECHANISM OF MITOCHONDRIAL EXTRUSION FROM PHENYLHYDRAZINE-INDUCED RETICULOCYTES IN THE CIRCULATING BLOOD. J. Cell Biol. 36, 103–109. https://doi.org/10.1083/jcb.36.1.103

Skiba, N.P., Lewis, T.R., Spencer, W.J., Castillo, C.M., Shevchenko, A., Arshavsky, V.Y., 2023. Absolute Quantification of Photoreceptor Outer Segment Proteins. J. Proteome Res. 22, 2703–2713. https://doi.org/10.1021/acs.jproteome.3c00267

Slautterback, D.B., 1965. MITOCHONDRIA IN CARDIAC MUSCLE CELLS OF THE CANARY AND SOME OTHER BIRDS. J. Cell Biol. 24, 1–22. https://doi.org/10.1083/jcb.24.1.1

Sloan, J.L., Achilly, N.P., Arnold, M.L., Catlett, J.L., Blake, T., Bishop, K., Jones, M., Harper, U., English, M.A., Anderson, S., Trivedi, N.S., Elkahloun, A., Hoffmann, V., Brooks, B.P., Sood, R., Venditti, C.P., 2020. The vitamin B12 processing enzyme, mmachc, is essential for

zebrafish survival, growth and retinal morphology. Hum. Mol. Genet. 29, 2109–2123. https://doi.org/10.1093/hmg/ddaa044

Sloat, S., Jankowski, C., Hutto, R., Giarmarco, M., Cleghorn, W.M., Tran, V., Shandar, G., Brockerhoff, S.E., Hurley, J., 2016. Quantification of Mitochondrial Structure in Photoreceptors. Invest. Ophthalmol. Vis. Sci. 57, 566.

Soubannier, V., McLelland, G.-L., Zunino, R., Braschi, E., Rippstein, P., Fon, E.A., McBride, H.M., 2012. A Vesicular Transport Pathway Shuttles Cargo from Mitochondria to Lysosomes. Curr. Biol. 22, 135–141. https://doi.org/10.1016/j.cub.2011.11.057

Stearns, G., Evangelista, M., Fadool, J.M., Brockerhoff, S.E., 2007. A Mutation in the Cone-Specific pde6 Gene Causes Rapid Cone Photoreceptor Degeneration in Zebrafish. J. Neurosci. 27, 13866–13874. https://doi.org/10.1523/JNEUROSCI.3136-07.2007

Stone, J., van Driel, D., Valter, K., Rees, S., Provis, J., 2008. The locations of mitochondria in mammalian photoreceptors: Relation to retinal vasculature. Brain Res. 1189, 58–69. https://doi.org/10.1016/j.brainres.2007.10.083

Strappazzon, F., Nazio, F., Corrado, M., Cianfanelli, V., Romagnoli, A., Fimia, G.M., Campello, S., Nardacci, R., Piacentini, M., Campanella, M., Cecconi, F., 2015. AMBRA1 is able to induce mitophagy via LC3 binding, regardless of PARKIN and p62/SQSTM1. Cell Death Differ. 22, 419–432. https://doi.org/10.1038/cdd.2014.139

Sugiura, A., Mattie, S., Prudent, J., McBride, H.M., 2017. Newly born peroxisomes are a hybrid of mitochondrial and ER-derived pre-peroxisomes. Nature 542, 251–254. https://doi.org/10.1038/nature21375

Sugiura, A., McLelland, G., Fon, E.A., McBride, H.M., 2014. A new pathway for mitochondrial quality control: mitochondrial-derived vesicles. EMBO J. 33, 2142–2156. https://doi.org/10.15252/embj.201488104

Takechi, M., Kawamura, S., 2005. Temporal and spatial changes in the expression pattern of multiple red and green subtype opsin genes during zebrafish development. J. Exp. Biol. 208, 1337–1345. https://doi.org/10.1242/jeb.01532

Tarboush, R., Flamarique, I.N., Chapman, G.B., Connaughton, V.P., 2014. Variability in mitochondria of zebrafish photoreceptor ellipsoids. Vis. Neurosci. 31, 11–23. https://doi.org/10.1017/S095252381300059X

Tarlow, D.M., Watkins, P.A., Reed, R.E., Miller, R.S., Zwergel, E.E., Lane, M.D., 1977. Lipogenesis and the synthesis and secretion of very low density lipoprotein by avian liver cells in nonproliferating monolayer culture. Hormonal effects. J. Cell Biol. 73, 332–353. https://doi.org/10.1083/jcb.73.2.332

Teh, C., Chudakov, D.M., Poon, K.-L., Mamedov, I.Z., Sek, J.-Y., Shidlovsky, K., Lukyanov, S., Korzh, V., 2010. Optogenetic in vivocell manipulation in KillerRed-expressing zebrafish transgenics. BMC Dev. Biol. 10, 110. https://doi.org/10.1186/1471-213X-10-110

Thoreson, W.B., 2021. Transmission at rod and cone ribbon synapses in the retina. Pflüg. Arch. - Eur. J. Physiol. 473, 1469–1491. https://doi.org/10.1007/s00424-021-02548-9

Tseng, Y.-C., Chen, R.-D., Lucassen, M., Schmidt, M.M., Dringen, R., Abele, D., Hwang, P.-P., 2011. Exploring Uncoupling Proteins and Antioxidant Mechanisms under Acute Cold Exposure in Brains of Fish. PLOS ONE 6, e18180. https://doi.org/10.1371/journal.pone.0018180

Tsukamoto, Y., Morigiwa, K., Ueda, M., Sterling, P., 2001. Microcircuits for Night Vision in Mouse Retina. J. Neurosci. 21, 8616–8623. https://doi.org/10.1523/JNEUROSCI.21-21-08616.2001

Tyrrell, L.P., Teixeira, L.B.C., Dubielzig, R.R., Pita, D., Baumhardt, P., Moore, B.A., Fernández-Juricic, E., 2019. A novel cellular structure in the retina of insectivorous birds. Sci. Rep. 9, 15230. https://doi.org/10.1038/s41598-019-51774-w

Umapathy, A., Torten, G., Paniagua, A.E., Chung, J., Tomlinson, M., Lim, C., Williams, D.S., 2023. Spatiotemporal Live-Cell Analysis of Photoreceptor Outer Segment Membrane Ingestion by the Retinal Pigment Epithelium Reveals Actin-Regulated Scission. J. Neurosci. 43, 2653–2664. https://doi.org/10.1523/JNEUROSCI.1726-22.2023

Unuma, K., Aki, T., Funakoshi, T., Hashimoto, K., Uemura, K., 2015. Extrusion of mitochondrial contents from lipopolysaccharide-stimulated cells: Involvement of autophagy. Autophagy.

Urschel, M.R., O'Brien, K.M., 2008. High mitochondrial densities in the hearts of Antarctic icefishes are maintained by an increase in mitochondrial size rather than mitochondrial biogenesis. J. Exp. Biol. 211, 2638–2646. https://doi.org/10.1242/jeb.018598

Utsumi, S., Sakamoto, K., Yamashita, T., Tomita, H., Sugano, E., Ishida, K., Ishiyama, E., Ozaki, T., 2020. Presence of ES1 homolog in the mitochondrial intermembrane space of porcine retinal cells. Biochem. Biophys. Res. Commun. 524, 542–548. https://doi.org/10.1016/j.bbrc.2020.01.127

van Ham, T.J., Mapes, J., Kokel, D., Peterson, R.T., 2010. Live imaging of apoptotic cells in zebrafish. FASEB J. 24, 4336–4342. https://doi.org/10.1096/fj.10-161018

Vatine, G., Vallone, D., Gothilf, Y., Foulkes, N.S., 2011. It's time to swim! Zebrafish and the circadian clock. FEBS Lett., Circadian Rhythms 585, 1485–1494. https://doi.org/10.1016/j.febslet.2011.04.007

Vihtelic, T.S., Doro, C.J., Hyde, D.R., 1999. Cloning and characterization of six zebrafish photoreceptor opsin cDNAs and immunolocalization of their corresponding proteins. Vis. Neurosci. 16, 571–585. https://doi.org/10.1017/S0952523899163168

Vincent, A.E., White, K., Davey, T., Philips, J., Ogden, R.T., Lawless, C., Warren, C., Hall, M.G., Ng, Y.S., Falkous, G., Holden, T., Deehan, D., Taylor, R.W., Turnbull, D.M., Picard, M., 2019.

Quantitative 3D Mapping of the Human Skeletal Muscle Mitochondrial Network. Cell Rep. 26, 996-1009.e4. https://doi.org/10.1016/j.celrep.2019.01.010

Vlist, M. van der, Raoof, R., Willemen, H.L.D.M., Prado, J., Versteeg, S., Gil, C.M., Vos, M., Lokhorst, R.E., Pasterkamp, R.J., Kojima, T., Karasuyama, H., Khoury-Hanold, W., Meyaard, L., Eijkelkamp, N., 2022. Macrophages transfer mitochondria to sensory neurons to resolve inflammatory pain. Neuron 110, 613-626.e9. https://doi.org/10.1016/j.neuron.2021.11.020

Wada, Y., Sandberg, M.A., McGee, T.L., Stillberger, M.A., Berson, E.L., Dryja, T.P., 2005. Screen of the IMPDH1 Gene among Patients with Dominant Retinitis Pigmentosa and Clinical Features Associated with the Most Common Mutation, Asp226Asn. Invest. Ophthalmol. Vis. Sci. 46, 1735–1741. https://doi.org/10.1167/iovs.04-1197

Wan, J., Goldman, D., 2016. Retina regeneration in zebrafish. Curr. Opin. Genet. Dev., Cell reprogramming, regeneration and repair 40, 41–47. https://doi.org/10.1016/j.gde.2016.05.009

Wang, M., Zhong, Z., Zhong, Y., Zhang, W., Wang, H., 2015. The Zebrafish Period2 Protein Positively Regulates the Circadian Clock through Mediation of Retinoic Acid Receptor (RAR)-related Orphan Receptor α (Rorα) *. J. Biol. Chem. 290, 4367–4382. https://doi.org/10.1074/jbc.M114.605022

Wang, X., Gerdes, H.-H., 2015. Transfer of mitochondria via tunneling nanotubes rescues apoptotic PC12 cells. Cell Death Differ. 22, 1181–1191. https://doi.org/10.1038/cdd.2014.211

Wen, X., Saltzgaber, G.W., Thoreson, W.B., 2017. Kiss-and-Run Is a Significant Contributor to Synaptic Exocytosis and Endocytosis in Photoreceptors. Front. Cell. Neurosci. 11. https://doi.org/10.3389/fncel.2017.00286

Wendel, B.J., Pandiyan, V.P., Liu, T., Jiang, X., Lassoued, A., Slezak, E., Schleufer, S., Bharadwaj, P., Tuten, W.S., Mustafi, D., Chao, J.R., Sabesan, R., 2024. Multimodal High-Resolution Imaging

in Retinitis Pigmentosa: A Comparison Between Optoretinography, Cone Density, and Visual Sensitivity. Invest. Ophthalmol. Vis. Sci. 65, 45. https://doi.org/10.1167/iovs.65.10.45

Wensel, T.G., Potter, V.L., Moye, A., Zhang, Z., Robichaux, M.A., 2021. Structure and dynamics of photoreceptor sensory cilia. Pflüg. Arch. - Eur. J. Physiol. 473, 1517–1537. https://doi.org/10.1007/s00424-021-02564-9

Williams, P.R., Suzuki, S.C., Yoshimatsu, T., Lawrence, O.T., Waldron, S.J., Parsons, M.J., Nonet, M.L., Wong, R.O.L., 2010. In vivo development of outer retinal synapses in the absence of glial contact. J. Neurosci. Off. J. Soc. Neurosci. 30, 11951–11961. https://doi.org/10.1523/JNEUROSCI.3391-10.2010

Williamson, D.H., Lund, P., Krebs, H.A., 1967. The redox state of free nicotinamide-adenine dinucleotide in the cytoplasm and mitochondria of rat liver. Biochem. J. 103, 514–527.

Wimberg, H., Janssen-Bienhold, U., Koch, K.-W., 2018. Control of the Nucleotide Cycle in Photoreceptor Cell Extracts by Retinal Degeneration Protein 3. Front. Mol. Neurosci. 11. https://doi.org/10.3389/fnmol.2018.00052

Winkler, B.S., 1981. Glycolytic and oxidative metabolism in relation to retinal function. J. Gen. Physiol. 77, 667–692. https://doi.org/10.1085/jgp.77.6.667

Wong, Y.C., Peng, W., Krainc, D., 2019. Lysosomal Regulation of Inter-mitochondrial Contact Fate and Motility in Charcot-Marie-Tooth Type 2. Dev. Cell 50, 339-354.e4. https://doi.org/10.1016/j.devcel.2019.05.033

Yang, P., Lockard, R., Titus, H., Hiblar, J., Weller, K., Wafai, D., Weleber, R.G., Duvoisin, R.M., Morgans, C.W., Pennesi, M.E., 2020. Suppression of cGMP-Dependent Photoreceptor Cytotoxicity With Mycophenolate Is Neuroprotective in Murine Models of Retinitis Pigmentosa. Invest. Ophthalmol. Vis. Sci. 61, 25. https://doi.org/10.1167/iovs.61.10.25

Yano, S., Tazawa, H., Kishimoto, H., Kagawa, S., Fujiwara, T., Hoffman, R.M., 2021. Real-Time Fluorescence Image-Guided Oncolytic Virotherapy for Precise Cancer Treatment. Int. J. Mol. Sci. 22, 879. https://doi.org/10.3390/ijms22020879

Youle, R.J., Narendra, D.P., 2011. Mechanisms of mitophagy. Nat. Rev. Mol. Cell Biol. 12, 9–14. https://doi.org/10.1038/nrm3028

Young, R.W., 1967. THE RENEWAL OF PHOTORECEPTOR CELL OUTER SEGMENTS. J. Cell Biol. 33, 61–72. https://doi.org/10.1083/jcb.33.1.61

Zhao, H., Chiaro, C.R., Zhang, L., Smith, P.B., Chan, C.Y., Pedley, A.M., Pugh, R.J., French, J.B., Patterson, A.D., Benkovic, S.J., 2015. Quantitative Analysis of Purine Nucleotides Indicates That Purinosomes Increase de Novo Purine Biosynthesis *♦. J. Biol. Chem. 290, 6705–6713. https://doi.org/10.1074/jbc.M114.628701